



UNIVERSITÀ DEGLI STUDI DI PAVIA

PHD PROGRAM IN MATHEMATICS AND STATISTICS

Dipartimento di Matematica “Felice Casorati”

**Beam Models:
Variational Derivation,
Analytical and Numerical
Solutions**

October 21, 2013

Supervisor: Professor

CARLO LOVADINA

Co - supervisor: Professor

FERDINANDO AURICCHIO

Author:

GIUSEPPE BALDUZZI

396814

Abstract

This thesis illustrates an application of the so-called *dimensional reduction* modelling approach, used to obtain some, linear, elastic beam-models starting from the 3D linear elastic problem. The approximated solutions of the beam-models are obtained through a finite element discretisation procedure. The goal of the whole procedure is to obtain a beam model and the corresponding finite element that satisfy efficiently the increasing engineering requests, in particular an accurate description of stresses.

The dimensional reduction results as the outcome of the following procedure: (i) weak formulation of the linear elastic problem, (ii) introduction of a cross-section approximation, (iii) application of the Fubini-Tonelli theorem, (iv) integration within the cross section of the weak-formulation terms. On the other hand, the mixed finite element results as the outcome of the following procedure: (i) modification of the beam-model formulation in order to satisfy the axial compatibility (and without violating equilibrium within the cross section), (ii) introduction of an axis piecewise-polynomial approximation, (iii) integration along the beam axis.

The thesis considers different weak formulations as starting point of the dimension reduction, pointing out the advantages of the Hellinger-Reissner functional. In particular, the use of the $H(\text{div}, \Omega)$ space results extremely useful in order to achieve an accurate stress description. Unfortunately, its finite element approximation could be extremely complicated from the computational point of view. On the other hand, step (i) of the finite element derivation allows to obtain a displacement-based finite element and attempts to mitigate the $H(\text{div}, \Omega)$ computational complexity.

The beam modelling and the finite-element discretisation procedures are applied to three significant situations: (i) non-homogeneous 2D beam body, (ii) non-homogeneous 3D beam body, (iii) 2D beam body with non-constant cross-section.

In all the considered cases, the resulting mixed beam models do not need correction factors, as the most of beam models used in practice. Moreover, they take correctly into account also equation couplings that occur, as an example, considering non-constant cross-section beams without symmetry. Finally, the beam model can predict the local effects of both boundary displacement constraints and non homogeneous or concentrated boundary load distributions, usually not accurately described by most of the standard beam models.

The beam finite elements inherit the capability to describe local effects of constraints and an accurate description stress distribution inside the cross section. Several numerical tests show that: (i) the finite element-solution converge to the analytical solution providing accurate description of both displacement and stresses, (ii) the computational efforts produce significant benefits in solution accuracy leading the proposed method to be convenient with respect to the standard ones usually adopted in practice, (iii) the beam model shows the expected asymptotic behaviour, and (iv) the beam model, and the corresponding finite element are able to model complex bodies, at least in conditions of practical interest.

Contents

Abstract (English)	I
Contents	V
List of Acronyms	VII
Nomenclature	X
List of Tables	XI
List of Figures	XIV
1 Introduction	1
1.1 General literature review	1
1.2 Goals	3
1.3 Outline	4
2 Problem Formulation and Applied Procedures	7
2.1 Explicit PDE	7
2.2 Hilbert spaces definition	9
2.3 TPE approach	9
2.4 HR approach	10
2.4.1 HR grad-grad stationarity	11
2.4.2 HR div-div stationarity	11
2.5 HW approach	12
2.5.1 HW grad-grad stationarity	13
2.5.2 HW div-div stationarity	13
2.6 Other, Less Used Principles	13
2.7 Conclusion on problem formulations	13
2.8 Applied procedures	14
2.8.1 Dimensional reduction	14
2.8.1.1 Literature review	15
2.8.1.2 Cross-section approximation	15
2.8.2 FE derivation procedure	15
2.8.2.1 Axial approximation	15
2.8.3 Conclusion on applied procedure	16

3	2D Beam-model	17
3.1	Profile approximation and notations	17
3.2	Problem formulation	18
3.3	TPE based beam model	19
3.3.1	Model formulation	19
3.3.2	Beam-model examples	20
3.3.2.1	Firts order, single layer beam	21
3.3.2.2	High order, single layer beam	21
3.3.2.3	Multilayer beam	22
3.3.3	FE derivation	24
3.3.3.1	FE formulation	24
3.3.3.2	Axial shape functions definition	24
3.4	HR-based beam models	24
3.4.1	Model formulation	25
3.4.1.1	grad-grad approach	25
3.4.1.2	div-div approach	26
3.4.1.3	Conclusions on the derived beam models	27
3.4.2	Cross-section shape function definition	28
3.4.3	Beam-model examples	28
3.4.3.1	Single layer beam	29
3.4.3.2	Multilayer beam	30
3.4.4	FE derivation	30
3.4.4.1	Weak problem formulation	31
3.4.4.2	FE formulation	31
3.4.4.3	Axis shape function definition	31
3.4.5	Numerical Examples	32
3.4.5.1	Multilayer homogeneous beam	32
3.4.5.1.1	Convergence	32
3.4.5.1.2	Boundary effects	35
3.4.5.2	Multilayer non-homogeneous symmetric section	37
3.4.5.3	Multilayer non-homogeneous non-symmetric section	38
3.5	Comparison of computational time	41
4	3D Beam-model	43
4.1	Literature review: existing 3D solutions	43
4.1.1	Saint-Venant solution	43
4.1.2	Saint-Venant solution enhancements	44
4.2	Model derivation	44
4.2.1	Cross-section approximation and notations	44
4.2.2	Model formulation	45
4.2.3	Cross-section shape functions definition	47
4.2.4	Beam-model examples	48
4.2.4.1	One-fiber cross-section	50
4.2.4.2	Two-fiber cross-section	51
4.2.4.3	Conclusions on beam models	51
4.3	FE derivation	52
4.3.1	Weak problem formulation	52
4.3.2	FE formulation	52
4.3.3	Axial shape functions definition	53

4.4	Numerical examples	54
4.4.1	Homogeneous square cross-section beam	54
4.4.1.1	Displacement error	55
4.4.1.2	Stress error	56
4.4.1.3	Asymptotic analysis	58
4.4.1.4	Computational costs	58
4.4.1.5	Conclusions on the beam model and the corresponding FE scheme	60
4.4.2	Rectangular slim cross-section	60
4.4.3	Non homogeneous cross-section beam (soft core beam)	62
4.4.4	L-shape cross-section beam	64
5	Non-constant Cross-section Beam-model	67
5.1	Engineering motivations	67
5.2	Problem formulation	69
5.3	Model derivation	69
5.3.1	Cross-section approximation and notations	70
5.3.2	Model formulation	71
5.3.3	Beam-model examples	72
5.3.3.1	Simplified kinematic and stress	72
5.3.3.2	Enhanced kinematic	73
5.4	FE derivation	74
5.5	Numerical examples	75
5.5.1	Symmetric tapered beam	75
5.5.2	Stiffness-matrix condition-number	80
5.5.3	Arch shaped beam	83
6	Final Remarks	87
	Bibliography	89

List of Acronyms

FE	Finite Element
FEM	Finite Element Method
3D	three dimension
2D	two dimension
1D	one dimension
ODE	Ordinary Differential Equation
PDE	Partial Differential Equation
SV	Saint Venant
EB	Euler Bernoulli
KL	Kichhoff Love
RM	Reissner Mindlin
HR	Hellingher Reissner
HW	Hu Washizu
TPE	Total Potential Energy
BVP	Boundary Value Problem
DOF	Degree Of Freedom
ECCOMAS	European Conference in Computational Methods in Applied Sciences and Engineering

Nomenclature

\mathbf{n}	outward unit vector	9
γ	generic field	15
$\hat{\gamma}$	axial coefficient function vector	15
λ	solution of the generalized eigenvalue problems	23
$(\cdot)^T$	transposition operation	15
$\nabla \cdot$	divergence operator	9
∇^s	symmetric gradient	9
ν	Poisson's coefficient	18
Ω	region occupied by the body	7
\bar{A}	radius of the smallest ball that contains the cross-section	7
\bar{l}	beam axis length	7
$\partial\Omega$	beam boundary	8
$\partial\Omega_s$	displacement constrained boundary	8
$\partial\Omega_t$	externally loaded boundary	8
∂A	cross-section boundary	8
$\bar{\mathbf{s}}$	assigned boundary displacement	8
σ	stress tensor	9
ε	strain tensor	9
D	forth order linear elastic tensor	8
E, ν	vectors defining the mechanical properties of the layers for 2D beams	23
$E_{1,2,3}$	boolean matices	18
F	beam model internal load	20
f	body load	8
G	matrix governing the HR based beam models	25

\mathbf{H}	matrix governing the HR based beam models	25
\mathbf{h}	vector defining the layer geometries for 2D beams	23
\mathbf{K}	finite element stiffness matrix	24
\mathbf{N}_γ	vector of axis shape functions	16
\mathbf{r}_γ	cross-section shape function vector	15
\mathbf{s}	displacement	9
\mathbf{T}	beam model boundary load	20
\mathbf{t}	external load	8
\mathbf{y}	cross-section coordinate	7
$\tilde{\gamma}$	finite element numerical coefficients	16
A	cross section	7
$A_{0,l}$	initial and final cross sections	8
d	number of the cross-section shape functions	15
E	Young's modulus	18
L	lateral surface of the beam	8
l	beam longitudinal axis	7
O	Cartesian coordinate origin	8
t	number of axis shape functions	16
x, y, z	Cartesian coordinate	8

List of Tables

2.1	Obtained functional critical point classified in terms of functionals from which are derived and equation formats.	14
3.1	Tensorial and Engineering equivalent notations.	18
3.2	Polynomial degrees of the profiles vectors, continuity properties and number of DOFs for a multi-layer beam.	23
3.3	Degree and continuity of cross-section profile functions and axis shape functions for the Total Potential Energy (TPE)- based Finite Element (FE).	24
3.4	Polynomial degrees of the profiles vectors, continuity properties and number of DOFs for a multi-layer beam.	28
3.5	Degree and continuity properties of shape functions with respect to y and x directions.	32
3.6	Transverse displacements and relative errors of the free-edge of a cantilever ($\bar{l} = 10$ and $h = 1$) obtained by different beam theories.	33
3.7	Transverse displacements and relative errors of the free-edge of a cantilever ($\bar{l} = 30$ and $h = 1$) obtained by different beam theories.	33
4.1	Degree and continuity of cross-section profile functions (C^{-1} means discontinuous function). . .	50
4.2	Degree and continuity of cross-section profile functions and axis shape functions (C^{-1} means discontinuous function)	53
4.3	Mean value of final cross-section displacement $\bar{v}(10)$ and the corresponding relative error for a cantilever ($\bar{l} = 10\text{mm}$, $b = h = 1\text{mm}$) evaluated using different beam models.	55
4.4	Final cross-section displacement relative error, number of DOFs used in the analysis ($\#$ DOFs), number of global stiffness-matrix entries different from zero ($\#$ entries $\neq 0$), band width of the global stiffness matrix (band-width), and estimation of the number of flops necessary to factorize the global stiffness matrix ($\#$ flops) for a cantilever ($\bar{l} = 10\text{mm}$, $b = h = 1\text{mm}$) evaluated using different beam models.	59
4.5	Minimum and maximum value of stress components distributions evaluated on the cross-section $x = 10\text{mm}$ for the non-homogeneous case, evaluated with different methods.	64
4.6	Minimum and maximum value of stress components distributions evaluated on the cross-section $x = 10\text{mm}$ for the L-shape case, evaluated with different methods.	66
5.1	Tensor and engineering equivalent notations.	71
5.2	Highest polynomial degree with respect to y of the cross-section shape functions used in beam modelling.	74
5.3	Non-symmetric tapered beams, parameter definitions for the considered examples	80
5.4	Non-constant cross-section beams, parameter definitions for the considered examples	81

List of Figures

2.1	3D beam geometry, Cartesian coordinate system, dimensions, and adopted notations.	8
2.2	Cross-section geometry, Cartesian coordinate system, dimensions, and adopted notations.	8
3.1	2D beam geometry, Cartesian coordinate system, dimensions, and adopted notations.	17
3.2	Relative errors on free-edge, transverse displacement for different mesh sizes δ and different number of layers.	34
3.3	Axial and transverse displacement coefficient functions of a three-layer, homogeneous cantilever, clamped in $x = 0$, loaded at $x = 2.5$ by a quadratic shear distribution and modelled by means of 64 elements.	35
3.4	Axial stress coefficient functions $s_{xi}(x)$ of a three layer, homogeneous cantilever, clamped in $x = 0$, loaded at $x = 2.5$ by a quadratic shear distribution and modelled with 64 elements.	35
3.5	Transversal stress coefficient functions and shear coefficient functions of a three layer, homogeneous cantilever, clamped in $x = 0$, loaded at $x = 2.5$ by a quadratic shear distribution and modelled by means of 64 elements.	36
3.6	Relative axial and transverse displacements (i.e. compatibility errors) evaluated on interlayer surfaces $S_1 : y = -1/5$ and $S_2 : y = 1/6$	36
3.7	Cross-section stress-distributions evaluated at $x = 2.5$, far from the clamped boundary. 1D and 2D solutions for the symmetric section.	37
3.8	Cross-section stress-distributions evaluated at $x = 0.5$, close to the clamped boundary. 1D and 2D solutions for the symmetric section.	38
3.9	Cross-section stress-distributions evaluated at $x = 0.125$, very close to the clamped boundary. 1D and 2D solutions for the symmetric section.	39
3.10	Cross-section stress-distributions evaluated at $x = 2.5$, 1D and 2D solutions for the un-symmetric section.	40
3.11	Displacement and shear errors versus the computational time, results evaluated for a 5 layer homogeneous beam.	42
4.1	3D beam geometry, Cartesian coordinate system, dimensions, and adopted notations.	43
4.2	Non-elementary cross-section geometry definition, dimensions, and adopted notations.	49
4.3	Homogeneous, square cross-section: dimensions and adopted discretization ($h = b = 1\text{mm}$, $E = 10^5\text{MPa}$, and $\nu = 0.25$).	49
4.4	Homogeneous cross section: geometry and mesh definition (in the considered example $h = b = 1\text{mm}$, δ variable, $E = 10^5\text{MPa}$, and $\nu = 0.25$).	54
4.5	Relative error $e_{v\text{rel}}$ plotted as function of the element size $1/\delta$	56
4.6	Shear axial coefficient functions $\hat{\tau}_{xy}(x)$ and $\hat{\tau}_{xz}(x)$ for the case of homogeneous and square cross section.	57
4.7	Shear cross-section distributions (4.7(a) and 4.7(b)) and cross-section error distributions (4.7(c) and 4.7(d)) for the case of homogeneous and square cross section.	57
4.8	Relative asymptotic error.	58

4.9	Relative error e_{vrel} plotted as function of the number of elements for different ratios h/\bar{l}	59
4.10	Slim cross section: geometry and mesh definition.	60
4.11	Transversal cross-section displacements (amplification factor 10) evaluated at $x = 10\text{mm}$	61
4.12	Shear components evaluated at $x = 10\text{mm}$ for the case of homogeneous, slim cross-section: cross-section distributions 4.12(a) and 4.12(c), cross-section relative error distributions 4.12(b) and 4.12(d) (results plotted for $y, z > 0$).	61
4.13	Non-homogeneous cross section: geometry and mesh definition (in the considered example $h = b = 1\text{mm}$, $a = 0.2\text{mm}$, $E_1 = 10^5\text{MPa}$, $E_2 = 10^3\text{MPa}$, and $\nu = 0.25$).	62
4.14	Stress distributions evaluated at $x = 10\text{mm}$ for the non homogeneous case.	63
4.15	L-shape cross section: geometry and mesh definition (in the considered example $b = 1\text{mm}$, $h = 0.5\text{mm}$, $a = c = 0.125\text{mm}$, $E = 10^5\text{MPa}$, and $\nu = 0.25$).	64
4.16	Stress distributions evaluated at $x = 10\text{mm}$ for the L-shape cross section.	65
5.1	2D beam geometry, coordinate system, dimensions and adopted notations.	67
5.2	Symmetric tapered beam: $\bar{l} = 10\text{mm}$, $\bar{A}(0) = 1\text{mm}$, $\bar{A}(\bar{l}) = 0.5\text{mm}$, $q = 1\text{N}$, $E = 100000\text{MPa}$, and $\nu = 0.25$	76
5.3	Displacement axial coefficient functions, evaluated for a symmetric tapered beam under shear-bending load.	76
5.4	Stress axial coefficient functions (Subfigure 5.4(a), 5.4(b), and 5.4(e)) and resulting internal actions (Subfigure 5.4(c), and 5.4(d)), evaluated for a symmetric tapered beam under shear-bending load.	78
5.5	Axial (Figure 5.5(a)) and transversal (Figure 5.5(a)) stress cross-section distributions, evaluated in the cross section $A(5)$	79
5.6	Cross-section shear distributions (Figures 5.6(a), 5.6(b), and 5.6(c)) and related absolute errors (Figure 5.6(d)).	79
5.7	Non-symmetric tapered beam: $\bar{l} = 10\text{mm}$, $\bar{A}(0) = \bar{A}(\bar{l}) + \Delta$, $E = 100000\text{MPa}$, and $\nu = 0.25$	80
5.8	Non-constant cross-section beam: $\bar{l} = 10\text{mm}$, $\bar{A}(0) = 1\text{mm}$, $\Delta = 0.46875\text{mm}$, $E = 100000\text{MPa}$, and $\nu = 0.25$	81
5.9	Stiffness matrix condition number.	82
5.10	Arch shaped beam: $\bar{l} = 10\text{mm}$, $\Delta = 0.5\text{mm}$, $\bar{A}(\bar{l}) = \bar{A}(0) = 0.6\text{mm}$, $q = 1\text{N/mm}$, $E = 100000\text{MPa}$, and $\nu = 0.25$	83
5.11	Displacement axial coefficient functions, evaluated for an arch shaped beam under axial load.	83
5.12	Stress axial coefficient functions, evaluated for an arch shaped beam under axial load.	84
5.13	Resulting actions distributions, evaluated for an arch shaped beam under axial load.	85

Chapter 1

Introduction

This chapter delineates the context and the practical reasons that motivate the investigations illustrated in this document. In particular, Section 1.1 introduces a brief discussion of the historical evolution and the state of art of beam modelling, Section 1.2 define the goals of the job described in the present document, and Section 1.3 provides a brief overview of the document.

1.1 General literature review

The continuum mechanic is one of the oldest research topic. In particular, as discussed in (Stein, 2012), scientists, mathematicians, and engineers contribute to the definition of principles, laws, and models since the origin of the modern science.

In particular, as illustrated in (Allen, 2013), the mathematical modelling of **beam-** and **plate-bodies** (i.e. prismatic bodies with one and two dimension predominant with respect to the others, respectively) develops concurrently with the continuum mechanic. More rigorously, Allen (2013) notices significant experience-based knowledges on beams and plates that led to build significant structures since the centuries before Christ.

In the following, we briefly introduce some models and solutions that could be considered milestones in beam modelling. Standard literature (e.g. see Timoshenko (1955) and Hjelmstad (2005)) provides their careful descriptions.

- The Euler Bernoulli (EB) beam model, proposed in eighteenth century, assumes that the cross-section dimensions are negligible with respect to the beam length. As a consequence, the cross section is assumed to remain rigid and orthogonal to the beam axis, also in deformed configuration. It follows that 4 cross-section rigid motion (i.e. (i) the axial displacement; (ii-iii) the translations orthogonal to the beam axis; (iv) the rotation around the beam axis) are necessary to describe the beam kinematic and 4 independent Ordinary Differential Equation (ODE) impose the equilibrium between the internal resulting stresses (i.e. axial compression, shears, bending moments, and torque) and the applied loads.
- The Saint Venant (SV) solution, proposed in nineteenth century, is an analytical solution of the three dimension (3D) Partial Differential Equation (PDE) governing the continuum mechanics, obtained using suitable conditions deeply discussed in Section 4.1.
- The Timoshenko beam model, proposed in the early twentieth century, generalizes the EB beam model, assuming that the cross section could rotate with respect to the beam axis. In particular, the model improves the description of the shear bending behaviour.

Consistently, we cite also some models that could be considered milestones in plate modelling.

- The Kirchhoff Love (KL) plate model, proposed in the late nineteenth century, generalize the EB assumptions to plate models.
- The Reissner Mindlin (RM) plate model, proposed in twentieth century, generalize the Timoshenko assumptions to plate models.

All the so far mentioned milestones assume the material to be elastic, homogeneous and isotropic. As a consequence, as highlighted also in EB beam model description, it is possible to distinguish and model independently the different behaviours of the beam. In fact, in standard model formulation, axial (membrane for plates), shear bending, and torque behaviours are governed by independent ODEs. Moreover, restricting our attention to the models, we notice that all of them assume simplified kinematic and, as a consequence, need correction factors, also for the simplest cases. Despite the limiting hypothesis on which are based, the milestone models are widely used also today in engineering practice, due to their first design capabilities.

Since the beginning twentieth century new materials, as reinforced concrete, laminated structures, and fibre reinforced composites became more and more diffused in engineering practice. Moreover, in the second half of the twentieth century, new design philosophies (as the limit-states and the performance-based design) become more and more popular and, nowadays, they are adopted as standard design-criterion by many countries (e.g. European Committee for Standardisation, EC0). Finally, new applications, as windmill blades and structures with complex geometry, need effective models of slender, but non-prismatic bodies. All the so far introduced trends lead the engineers to require more and more accurate analysis, leading the milestone models to be inadequate with respect to the increasing engineering requests.

Hence, researchers have developed new approaches that can generally be classified as:

- **high-order, displacement-based models**, which introduce more sophisticated cross-section kinematics,
- **mixed or hybrid models**, which introduce also stresses – and sometimes even strains – as independent variables.

Just to give a few examples, an often cited model falling in the first category is the one proposed by Reddy (1984) that introduces section warping in addition to Timoshenko displacements. As discussed by Sheinman (2001), this model shows an inconsistency, since transverse displacement generates a constant cross-section shear distribution, whereas axial displacements give a quadratic one. A more complete kinematics is adopted in the model proposed by Lo et al. (1977a) where, considering both section warping and striction, authors eliminate such an inconsistency. For a general treatment of high-order, planar, kinematic beam models and discussion of their analytical solutions the readers may refer to the work of Sheinman (2001). With respect to mixed models, a very interesting approach is the one proposed by Alessandrini et al. (1999), where, starting from 3D elasticity, the authors illustrate a clear derivation of some plate models, studying also the convergence of the models under consideration.

In addition, for the case of multilayer beams and plates, many further choice could be done in modelling (e.g., see Carrera (2000) and Wanji and Zhen (2008)). As an example, *layer-wise* models adopt piecewise layer-defined functions while *global* models use globally defined functions to describe the field distribution on cross-section. For both items, intermediate choices are possible, e.g. only some stress components could be selected as independent variables, or some fields are described layer-wise, while the remaining ones are assumed as global functions.

As explained in (Hjelmstad and Taciroglu, 2003), the new design philosophies challenge the classical beam-modelling approach, based on displacements, since they do not provide a sufficiently accurate stress description, in particular in the case of inelastic materials. To insert non-linear

behaviour into beam models and frame structures, as explained in (Saritas and Filippou, 2009), practitioners usually follow two possible strategies listed in the following.

- **Concentrated plasticity** that uses non-dimensional non linear elements, such as rotational springs, which position is fixed a-priori. The main limitation of this method consists in the incapability of model, as an example, the compression-bending interaction.
- **Distributed plasticity** (e.g. Spacone et al., 1996) that uses a so called fibre model, i.e. a model that assume the EB kinematic and a simplified non linear constitutive law applied to portions of cross section called fibres. This strategy overcomes some limitations of concentrated plasticity but the simplified kinematic and constitutive laws often lead to non accurate solutions.

In the attempt to treat more rigorously non-linear constitutive laws, researchers consider also other approaches, like the force-based method in which primary variables are the stress resultants (e.g. Hjelmstad and Taciroglu, 2002) and the already mentioned mixed methods (e.g. Hjelmstad and Taciroglu, 2005). Hjelmstad and Taciroglu (2003) notice that some of the strategies proposed in literature have not a consistent variational structure and, moreover, there is not a method that is clearly superior to the other.

In the second half of the twentieth century, moreover, the availability of computational instruments leads to the diffusion of many numerical techniques useful to find an approximated solution for the models so far introduced. The most successful method is clearly the Finite Element Method (FEM) that was widely investigated from theoretical point of view and applied in engineering practice. A literature review shows that the number of proposed beam and plate FE implementations is nearly uncountable. This depends on the fact that many different choices are possible and span from the functional formulation with the corresponding independent variables to the order of field approximation. Moreover, we notice that beam and plate FE could suffer from locking phenomena that consists in a spurious increase of the stiffness occurring with mesh refinement.

As a general remark, we notice that the most of the proposed models in engineering practice are effective for specific problems, whereas no general procedure are proposed in order to model complex and general situations.

1.2 Goals

The goal of this thesis is to investigate a beam modelling approach and the correspondent FE such that the obtained models could satisfy the following requirements.

- They could be used with a general 3D constitutive relation.
- They could consider non-homogeneous materials within the cross-section.
- They could consider non-constant cross-section.
- They do not need correction factors.
- They do not show static or kinematic inconsistency.

Moreover, we require that the beam FE satisfies the following requirements.

- It does not suffer any locking phenomena.
- It uses the same Degree Of Freedom (DOF) of standard FE, i.e. we have the possibility to integrate the proposed FE in existing displacement based codes.

The reasons that motivate the present research are purely engineering, nevertheless, the achievement of the so far introduced goals requires an adequate mathematical support.

As a consequence, an additional fundamental goal is to apply the mathematical knowledges during derivation and validation such that the goodness of the model could be rigorously discussed.

1.3 Outline

The contents and the main results of each chapter are illustrated in the following.

Problem Formulation and Applied Procedures

Chapter 2 formulates rigorously the Boundary Value Problem (BVP) we are going to tackle. In particular, we write the explicit PDE assuming a generic n -dimensional domain. We write some weak problem formulations, discussing their applications in beam and plate modelling and highlighting advantages and critical steps in their use.

Finally, Chapter 2 introduces the mathematical procedures and the associated notations we use in order to derive the beam models. In particular, we introduce the dimensional reduction method, providing also a short literature review, and the FEM. We highlight some similarities between the two method and discuss the main advantages of the whole procedure.

2D Beam-model

Chapter 3 derives some 2D beam models and the corresponding FEs. In particular we derive 3 different beam models:

- a displacement based beam model,
- a displacement-accurate mixed beam model, developed starting from a functional formulation that privileges the displacement description,
- a stress-accurate mixed beam model, developed starting from a functional formulation that privileges the stress description; this functional is not diffused in engineering practice, despite the advantages indicated by mathematicians.

We illustrate that the displacement based beam model is not capable to recover correctly the simplest milestone beam models whereas the stress-accurate beam model has this capability. Moreover, we show that all the models, in case of multilayer beams, have the capability to describe effectively boundary effects.

In derivation of the stress-accurate mixed beam model FE formulation we opportunely integrate by parts some terms of the beam model weak formulation. As a consequence, the FE enforces the displacement compatibility along the axis, whereas it continues to privilege the stress description within the cross section. This choice allows to achieve the FE goals listed in Section 1.2. **Moreover, in the computational framework, the shape functions for the dimension reduction and for the FE are easier to manipulate than the ones used for a standard 3D full discretisation, at least under the simplifications considered in models development.**

The numerical results highlight the accuracy of the proposed mixed model solution and its convergence. In particular the chapter illustrate the capability of the beam model to take into account multilayer, non homogeneous cross-sections. Finally, the chapter provides some information about the computational effectiveness of the proposed method, highlighting that the mixed beam models could be competitive with respect to the high-order displacement based models.

Most of the results illustrated in this chapter was already published in Auricchio et al. (2010) and presented by the author during the European Conference in Computational Methods in Applied Sciences and Engineering (ECCOMAS) 2010 ab1 (2010).

3D Beam-model

Chapter 4 derives the 3D beam model and the corresponding FE. Due to the results discussed in Chapter 3, this chapter focuses the attention on the stress-accurate mixed beam-model and the corresponding FE. Also the 3D beam model has the capability to describe the boundary effects, that increases refining the cross-section discretisation.

Numerical results illustrate the capabilities of the model to describe accurately also complex situations as the anti-clastic bending. Moreover, we provide some informations about convergence and numerical errors, highlighting the good behaviour of the solution with respect to the mesh refinement.

Finally, we discuss some tests on the asymptotic behaviour, i.e. the behaviour of the solution when the beam slenderness goes to infinity. The so far mentioned slenderness is defined as the ratio between axis length and cross-section size, Numerical results show that the solution converge to the EB beam solution, as expected and proved in literature. Unfortunately, the numerical tests highlight also the worsening of the stiffness-matrix condition number for extremely slender beams.

The results illustrated in this chapter was already published in Auricchio et al. (2013) and presented by the author during the ECCOMAS 2012 abl (2012).

Non-constant Cross-section Beam-model

Chapter 5 derives a 2D beam model with non-constant and homogeneous cross-section and the corresponding FE. The domain definition does not fail in the general framework provided in Chapter 2, as a consequence we need to introduce a specific problem formulation.

In order to develop the non-constant beam model and the corresponding FE, we modify opportunely the stress-accurate mixed beam model illustrated in Chapter 3. The literature review indicates that the enforcement of boundary equilibrium is the critical aspect in non-constant beam modelling. Fortunately, the considered beam modelling approach allows to tackle this aspect without particular difficulties.

Numerical results show that the obtained beam model provide satisfactory description of the body behaviour in a large class of examples. Moreover, numerical results show that the beam FE results to be robust with respect to the domain geometry worsening, at least in the condition of practical interest.

Chapter 2

Problem Formulation and Applied Procedures

In this chapter we provide the mathematical formulation of the continuum mechanics problem we are going to consider. In order to be as general as possible, we consider a generic n -dimensional domain. Obviously, for the practitioners, the cases of interest are $n = 2$ and $n = 3$ that lead to 2D and 3D problems, respectively. Chapters 3 and 5 consider the 2D problem as starting point, whereas Chapter 4 treats the 3D problem.

Section 2.1 defines the PDE governing the linear elastic problem we are going to investigate in the following. Section 2.2 introduces the definition of some Hilbert spaces that we use in next sections. Sections 2.3, 2.4, 2.5, and 2.6 introduce different weak problem formulations, with some emphasis on the Hellinger Reissner (HR) functional. Section 2.7 contains some observation on the different problem formulations. Finally, Section 2.8 introduces the mathematical procedures that will be used in next chapters.

2.1 Problem Strong Formulation

The object of our study is a n -dimensional **beam body** Ω , that behaves under the assumption of linear elastic constitutive relation and small displacements. We highlight that the so far introduced assumptions allow to consider a *linear problem*. Moreover, we do not introduce assumptions about homogeneity and isotropy of the material that constitute the body. The latter assumption results to be useful in order to solve some specific engineering problems that will be mentioned in the following chapters.

We assume that the problem domain $\Omega \subset \mathbb{R}^n$ can be expressed as follows:

$$\Omega := l \times A \tag{2.1}$$

where the **beam longitudinal axis** l and the **cross-section** A are orthogonal, closed, and bounded sets defined as follows:

$$l := \{x \in \mathbb{R} \mid x \in [0, \bar{l}]\} \quad A := \{\mathbf{y} \in \mathbb{R}^{n-1}\}$$

We denote the **length of the longitudinal axis** as \bar{l} , and the **radius of the smallest ball that contains the cross-section** as \bar{A} . In engineering practice is usual to assume that $\bar{l} \gg \bar{A}$ for reasons that will be explained in Chapter 4. Nevertheless we highlight that this hypothesis is not necessary in the further development.

Being ∂A the **cross-section boundary**, we define the **lateral surface** as $L := l \times \partial A$. Moreover we define the **initial and final cross-sections** as $\{A_0, A_l\} := \{0, \bar{l}\} \times A$.

In order to give an example, Figure 2.1 represents a 3D domain with the relative Cartesian coordinate system, the initial and the final cross sections A_0 and A_l respectively, and the lateral surface L .

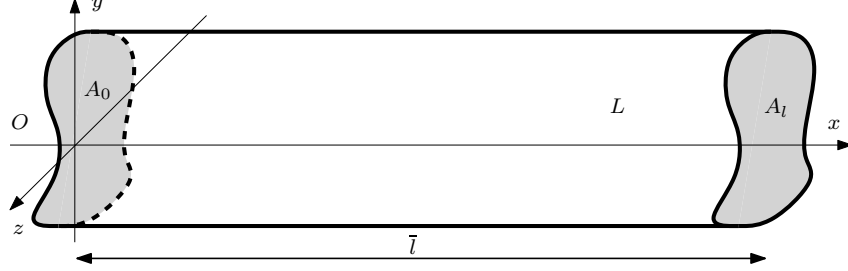


Figure 2.1: 3D beam geometry, Cartesian coordinate system, dimensions, and adopted notations.

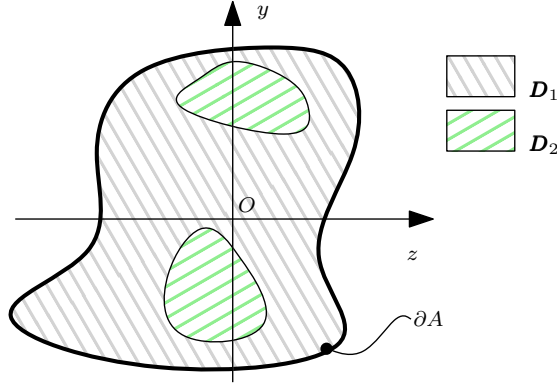


Figure 2.2: Cross-section geometry, Cartesian coordinate system, dimensions, and adopted notations.

We denote the **domain boundary** as $\partial\Omega$, so that $\partial\Omega := A_0 \cup A_l \cup L$. For $\partial\Omega$, we consider the partition $\{\partial\Omega_t; \partial\Omega_s\}$, where $\partial\Omega_t$ and $\partial\Omega_s$ are the **externally loaded** and the **displacement constrained boundaries**, respectively.

The **external load** is defined as a *sufficiently smooth* surface force density $\mathbf{t} : \partial\Omega_t \rightarrow \mathbb{R}^n$ while the **body load** is defined as a volume force density $\mathbf{f} : \Omega \rightarrow \mathbb{R}^n$. Moreover, we specify a *sufficiently smooth boundary displacement* function $\mathbf{\bar{s}} : \partial\Omega_s \rightarrow \mathbb{R}^n$. The regularities of external load and boundary displacement function will be specified in the following sections, consistently with the specific variational problem formulation. We highlight also that the required regularity may change with respect to the specific variational formulation we are considering.

As illustrated in Figure 2.2, referring to 3D beam body, we assume that the body could be not homogeneous in the cross section. As a consequence, the fourth order **linear elastic tensor** \mathbf{D} depends on the cross-section coordinates, i.e. $\mathbf{D} : A \rightarrow \mathbb{R}^{n \times n \times n \times n}$. In particular, Figure 2.2 represents a cross-section in which the linear elastic tensor is constant piecewise defined. Nevertheless, we can consider more general definitions, like a linear dependence on the cross-section coordinate that allow to model complex materials, like those called **graded materials**.

Being $\mathbb{R}_s^{n \times n}$ the space of symmetric, second-order tensors, we introduce the **stress** field $\boldsymbol{\sigma} : \Omega \rightarrow \mathbb{R}_s^{n \times n}$, the **strain** field $\boldsymbol{\epsilon} : \Omega \rightarrow \mathbb{R}_s^{n \times n}$, and the **displacement** vector field $\mathbf{s} : \Omega \rightarrow \mathbb{R}^n$.

Thereby the strong formulation of the elastic problem corresponds to the following BVP:

$$\boldsymbol{\varepsilon} = \nabla^s \mathbf{s} \quad \text{in } \Omega \quad (2.2a)$$

$$\boldsymbol{\sigma} = \mathbf{D} : \boldsymbol{\varepsilon} \quad \text{in } \Omega \quad (2.2b)$$

$$\nabla \cdot \boldsymbol{\sigma} + \mathbf{f} = \mathbf{0} \quad \text{in } \Omega \quad (2.2c)$$

$$\boldsymbol{\sigma} \cdot \mathbf{n} = \mathbf{t} \quad \text{on } \partial\Omega_t \quad (2.2d)$$

$$\mathbf{s} = \bar{\mathbf{s}} \quad \text{on } \partial\Omega_s \quad (2.2e)$$

where ∇^s is an operator that provides the symmetric part of the gradient, $\nabla \cdot$ represents the divergence operator, and $:$ represents the double dot product. Equation (2.2a) is the **compatibility** relation, Equation (2.2b) is the **material constitutive relation** and Equation (2.2c) represents the **equilibrium** condition. Equations (2.2d) and (2.2e) are respectively the **boundary equilibrium** and the **boundary compatibility** condition, where \mathbf{n} is the outward unit vector, defined on the boundary.

2.2 Hilbert spaces definition

In this section we define the Hilbert spaces that we use in problem weak formulations. Moreover, for each space we discuss existing FE approximations.

For the generic variable $\boldsymbol{\gamma} : \Omega \rightarrow \mathbb{R}^{(\cdot)}$ we define the following space:

$$L^2(\Omega) := \left\{ \boldsymbol{\gamma} : \Omega \rightarrow \mathbb{R}^{(\cdot)} : \int_{\Omega} \boldsymbol{\gamma} \cdot \boldsymbol{\gamma} d\Omega < \infty \right\} \quad (2.3)$$

where the operator \cdot indicates a suitable scalar product.

For the displacement field we define the following space:

$$H^1(\Omega) := \left\{ \mathbf{s} : \Omega \rightarrow \mathbb{R}^n : \mathbf{s} \text{ and } (\nabla^s \mathbf{s}) \in L^2(\Omega) \right\} \quad (2.4)$$

The FE discretization of this space are extremely numerous. The most of FE described in standard engineering literature on the topic (e.g. Zienkiewicz and Taylor, 2000a) approximate this field.

For the stress field we define the following space:

$$H(\text{div}, \Omega) := \left\{ \boldsymbol{\sigma} : \Omega \rightarrow \mathbb{R}_s^{n \times n} : \boldsymbol{\sigma} \text{ and } (\nabla \cdot \boldsymbol{\sigma}) \in L^2(\Omega) \right\} \quad (2.5)$$

The FE discretization of this space is indicated as a critical step in the literature. In fact, the first two dimension (2D) stable FE $H(\text{div}, \Omega)$ discretisation that uses polynomial globally defined on the elements was proposed in 2002 by Adams and Cockburn (2005). In the lowest order case, the proposed FE uses 24 DOFs that are defined on vertices, edges, and inside each triangle. Before these result the strategies adopted for the FE discretisation consist in weakly imposition of stress tensor symmetry (e.g. Amara and Thomas, 1979; Arnold and Falk, 1988) or in the use of composite elements (e.g. Johnson and Mercier, 1978).

A first 3D stable non-composite FE discretisation was proposed in 2005 by Adams and Cockburn (2005). A complete family of 3D FE was proposed and investigated in (Arnold et al., 2008) where the authors notice that, in the lowest order case, a single FE has 162 DOF. In consequence of the FE complexity, the authors notice the low practical interest of the proposed element.

2.3 Total Potential Energy approach

TPE is the functional most frequently used in continuum mechanics and in standard literature (e.g. Hjelmstad, 2005). Several authors use it as a starting point to derive both first-order beam models as well as the most popular corresponding FE formulations.

The TPE functional can be expressed as follows:

$$J_{TPE}(\mathbf{s}) = \frac{1}{2} \int_{\Omega} \nabla^s \mathbf{s} : \mathbf{D} : \nabla^s \mathbf{s} d\Omega - \int_{\Omega} \mathbf{s} \cdot \mathbf{f} d\Omega - \int_{\partial\Omega_t} \mathbf{s} \cdot \mathbf{t} dS \quad (2.6)$$

Boundary conditions will be suitably imposed in what follows. The critical point of the functional above corresponds to find the energy minimizer, which is unique and stable in the usual framework of admissible displacement space.

Requiring stationarity of TPE (2.6), we obtain the following weak problem:

Find $\mathbf{s} \in W_{\overline{\mathbf{s}}}^s$ such that $\forall \delta \mathbf{s} \in W^s$:

$$\delta J_{TPE}^s = \int_{\Omega} \nabla^s (\delta \mathbf{s}) : \mathbf{D} : \nabla^s \mathbf{s} d\Omega - \int_{\Omega} \delta \mathbf{s} \cdot \mathbf{f} d\Omega - \int_{\partial\Omega_t} \delta \mathbf{s} \cdot \mathbf{t} dS = 0 \quad (2.7)$$

where

$$W_{\overline{\mathbf{s}}}^s := \{ \mathbf{s} \in H^1(\Omega) : \mathbf{s}|_{\partial\Omega_s} = \overline{\mathbf{s}} \} \quad (2.8)$$

$$W^s := \{ \delta \mathbf{s} \in H^1(\Omega) : \delta \mathbf{s}|_{\partial\Omega_s} = \mathbf{0} \} \quad (2.9)$$

We define Equation (2.7) as the **TPE symmetric stationarity** that is often used as a basis for FE development, leading obviously to a symmetric stiffness matrix. We notice that the boundary condition (2.2e) is imposed as essential condition in W^s , whereas the boundary equilibrium (2.2d) is a natural condition, weakly imposed through the TPE symmetric stationarity (2.7).

Wanji and Zhen (2008) give a review on multilayered, elastic, displacement-based (i.e., TPE derived) plate FE. Increasing orders of field approximation are considered, from the simplest model in which displacements are globally defined along the cross-section, to the most sophisticated ones in which displacements are defined layer-wise. Wanji and Zhen also notice that almost all the presented FE perform only for some specific problems (thick laminated plates, soft-core sandwich, etc.), but they are not able to accurately describe the shear distribution along the thickness in the general case.

An accurate evaluation of shear distribution is one of the aims of the work by Vinayak et al. (1996a,b), in which the authors develop a multilayered planar beam FE starting from Equation (2.7), using the field approximation proposed by Lo et al. (1977a,b) and appropriately treating the thickness heterogeneity. They propose two ways to evaluate the axial and transverse stresses: the first one uses the compatibility and the constitutive relations (Equations (2.2a) and (2.2b)), while the second one refines the shear and the out-of-plane stress distributions using the equilibrium relation (2.2c). The resulting numerical schemes are generally satisfactory, but the computed solutions might exhibit instabilities near the boundary, and the stress distributions are not always sufficiently accurate.

As a general remark (see Rohwer and Rolfes (1998) and Rohwer et al. (2005)), in TPE-based models the critical step is the post processing stress evaluation that could compromise the effectiveness of the method.

2.4 Hellinger-Reissner approach

The HR functional can be expressed as:

$$J_{HR}(\boldsymbol{\sigma}, \mathbf{s}) = \int_{\Omega} \boldsymbol{\sigma} : \nabla^s \mathbf{s} d\Omega - \frac{1}{2} \int_{\Omega} \boldsymbol{\sigma} : \mathbf{D}^{-1} : \boldsymbol{\sigma} d\Omega - \int_{\Omega} \mathbf{s} \cdot \mathbf{f} d\Omega \quad (2.10)$$

How boundary conditions will be enforced depends on the specific variational formulation employed to express the stationarity of the functional (cf. Subsections 2.4.1 and 2.4.2). We also wish to remark that stationarity of this functional corresponds to a saddle point problem. Therefore, the model derivation based on HR functional requires a particular care on the displacement and stress field assumptions, otherwise the model risks to lead to a problem lacking well-posedness.

2.4.1 HR grad-grad stationarity

Requiring stationarity of HR functional (2.10), we obtain the following weak problem:

$$\boxed{\begin{aligned} &\text{Find } \mathbf{s} \in W_{\bar{\mathbf{s}}}^{gg} \text{ and } \boldsymbol{\sigma} \in S^{gg} \text{ such that } \forall \delta \mathbf{s} \in W^{gg} \text{ and } \forall \delta \boldsymbol{\sigma} \in S^{gg}: \\ &\delta J_{HR}^{gg} = \int_{\Omega} \nabla^s \delta \mathbf{s} : \boldsymbol{\sigma} d\Omega + \int_{\Omega} \delta \boldsymbol{\sigma} : \nabla^s \mathbf{s} d\Omega - \int_{\Omega} \delta \boldsymbol{\sigma} : \mathbf{D}^{-1} : \boldsymbol{\sigma} d\Omega \\ &- \int_{\Omega} \delta \mathbf{s} \cdot \mathbf{f} d\Omega - \int_{\partial\Omega_t} \delta \mathbf{s} \cdot \mathbf{t} dS = 0 \end{aligned}} \quad (2.11)$$

where

$$\begin{aligned} W_{\bar{\mathbf{s}}}^{gg} &:= \{ \mathbf{s} \in H^1(\Omega) : \mathbf{s}|_{\partial\Omega_s} = \bar{\mathbf{s}} \} \\ W^{gg} &:= \{ \delta \mathbf{s} \in H^1(\Omega) : \delta \mathbf{s}|_{\partial\Omega_s} = \mathbf{0} \} \\ S^{gg} &:= \{ \boldsymbol{\sigma} \in L^2(\Omega) \} \end{aligned}$$

We call Equation (2.11) **HR grad-grad stationarity** because two gradient operators appear in the formulation. We remark that the kinematic boundary condition $\mathbf{s}|_{\partial\Omega_s} = \bar{\mathbf{s}}$ is directly enforced in the trial space $W_{\bar{\mathbf{s}}}^{gg}$ (*essential* boundary condition), while $\boldsymbol{\sigma} \cdot \mathbf{n}|_{\partial\Omega_t} = \mathbf{t}$ turns out to be a *natural* boundary condition.

Alessandrini et al. (1999) derived some homogeneous plate models starting from HR grad-grad stationarity (2.11). They noticed that in many situations, models derived by HR grad-grad stationarity (2.11) lead to model displacement fields which minimize the potential energy in the class of the same kinematic assumptions. Therefore, in those cases HR grad-grad models are equivalent to the corresponding models obtained by the TPE symmetric stationarity (2.7).

Many researchers have derived multilayered plate and beam FE using HR grad-grad stationarity (2.11). The works by Spilker (1982), Feng and Hoa (1998), Icardi and Atzori (2004) and Huang et al. (2002) are among the most significant examples, since the computed solutions are generally satisfactory. The main drawback of these schemes, especially for the case of layer-wise beams and plates, is the high number of degrees of freedom (DOFs) that leads to an heavy FE formulation. Spilker (1982) alleviates this problem by assuming stress variables to be discontinuous along the plate extension so that they can be condensed at the element level reducing the mixed local stiffness matrix to a displacement-like one.

2.4.2 HR div-div stationarity

Integrating by parts, the first and the second terms of Equation (2.11) become:

$$\begin{aligned} \int_{\Omega} \nabla^s \delta \mathbf{s} : \boldsymbol{\sigma} d\Omega &= \int_{\partial\Omega} \delta \mathbf{s} \cdot \boldsymbol{\sigma} \cdot \mathbf{n} dS - \int_{\Omega} \delta \mathbf{s} \cdot \nabla \cdot \boldsymbol{\sigma} d\Omega \\ \int_{\Omega} \delta \boldsymbol{\sigma} : \nabla^s \mathbf{s} d\Omega &= \int_{\partial\Omega} \delta \boldsymbol{\sigma} \cdot \mathbf{n} \cdot \mathbf{s} dS - \int_{\Omega} \nabla \cdot \delta \boldsymbol{\sigma} \cdot \mathbf{s} d\Omega \end{aligned} \quad (2.12)$$

Hence, substituting Expression (2.12) in (2.11), the weak formulation becomes:

$$\boxed{\begin{aligned} &\text{Find } \mathbf{s} \in W^{dd} \text{ and } \boldsymbol{\sigma} \in S_t^{dd} \text{ such that } \forall \delta \mathbf{s} \in W^{dd} \text{ and } \forall \delta \boldsymbol{\sigma} \in S^{dd} \\ &\delta J_{HR}^{dd} = - \int_{\Omega} \delta \mathbf{s} \cdot \nabla \cdot \boldsymbol{\sigma} \, d\Omega - \int_{\Omega} \nabla \cdot \delta \boldsymbol{\sigma} \cdot \mathbf{s} \, d\Omega - \int_{\Omega} \delta \boldsymbol{\sigma} : \mathbf{D}^{-1} : \boldsymbol{\sigma} \, d\Omega \\ &- \int_{\Omega} \delta \mathbf{s} \cdot \mathbf{f} \, d\Omega + \int_{\partial\Omega_s} \delta \boldsymbol{\sigma} \cdot \mathbf{n} \cdot \bar{\mathbf{s}} \, dS = 0 \end{aligned}} \quad (2.13)$$

where

$$W^{dd} := \{\mathbf{s} \in L^2(\Omega)\} \quad (2.14)$$

$$S_t^{dd} := \{\boldsymbol{\sigma} \in H(\text{div}, \Omega) : \boldsymbol{\sigma} \cdot \mathbf{n}|_{\partial\Omega_t} = \mathbf{t}\} \quad (2.15)$$

$$S^{dd} := \{\delta \boldsymbol{\sigma} \in H(\text{div}, \Omega) : \delta \boldsymbol{\sigma} \cdot \mathbf{n}|_{\partial\Omega_t} = \mathbf{0}\} \quad (2.16)$$

We define Equation (2.13) as **HR div-div stationarity** because two divergence operators appear in it. We remark that $\mathbf{s}|_{\partial\Omega_s} = \bar{\mathbf{s}}$ is now a *natural* boundary condition, while $\boldsymbol{\sigma} \cdot \mathbf{n}|_{\partial\Omega_t} = \mathbf{t}$ becomes an *essential* boundary condition, as it is directly incorporated in the space S_t^{dd} .

Considering the HR div-div stationarity approach (2.13), Alessandrini et al. have derived some homogeneous plate models, more interesting than the ones stemming from the HR grad-grad stationarity (2.11). However, the same techniques developed in Alessandrini et al. cannot be directly applied to general heterogeneous plates, because the resulting models may be divergent (cf. Auricchio et al. (2004)).

We highlight that the boundary equilibrium $\boldsymbol{\sigma} \cdot \mathbf{n}|_{\partial\Omega_t} = \mathbf{t}$ is an *essential* condition (i.e. it is strongly imposed into the space definition and it must be exactly satisfied everywhere on the loaded boundary $\partial\Omega_t$) whereas the boundary compatibility is a *natural* condition (i.e. it is naturally satisfied by the functional stationarity and it is weakly imposed on the displacement constrained boundary $\partial\Omega_s$).

The HR functional (2.10) is deeply investigated in mathematical literature, a classical reference is Brezzi and Fortin (1991) in which authors enunciate necessary conditions to ensure that Problem (2.10) is *well posed*, moreover, for the same problem, they develop the FE approximation providing error estimation and proving the convergence of both variables \mathbf{s} and $\boldsymbol{\sigma}$.

The basic idea of well-posed condition is that, since in functional stationarity (2.10) we use virtual displacements $\delta \mathbf{s}$ to test stresses $\boldsymbol{\sigma}$ and vice-versa, the richness of both fields must be equilibrate such that there is not uncontrolled variables.

As discussed in Auricchio et al. (2010), despite the interest of mathematicians, the applications of the functional stationarity (2.10) are not so diffused: Auricchio et al. (2004), Batra et al. (2002), and Batra and Vidoli (2002) are the few papers we found in engineering literature in which authors use the HR functional (2.10) or some others, similar to (2.10) for the use of the divergence operator. A possible cause could be the need to satisfy some non-trivial conditions on regularity and dimension of both spaces W and S to ensure the problem is *well-posed*. Moreover, the approximation of $H(\text{div}, \Omega)$ using FE technique is quite complex to manage from the numerical point of view.

2.5 Hu–Washizu approach

The Hu Washizu (HW) functional may be expressed as follows:

$$J_{HW}(\boldsymbol{\sigma}, \boldsymbol{\varepsilon}, \mathbf{s}) = \int_{\Omega} \boldsymbol{\sigma} : (\nabla^s \mathbf{s} - \boldsymbol{\varepsilon}) \, d\Omega + \frac{1}{2} \int_{\Omega} \boldsymbol{\varepsilon} : \mathbf{D} : \boldsymbol{\varepsilon} \, d\Omega - \int_{\Omega} \mathbf{s} \cdot \mathbf{f} \, d\Omega \quad (2.17)$$

Again, how boundary conditions will be enforced depends on the specific variational formulation employed to express the stationarity of the functional. We also remark that, here, also the strain field is a primal variable. In the following variational formulations, we will not specify the functional frameworks for the involved fields, since they are similar to the ones of the HR-based corresponding variational formulations.

2.5.1 HW grad-grad stationarity

The critical point of Equation (2.17) can be expressed as:

$$\begin{aligned} \delta J_{HW}^{gg} = & \int_{\Omega} \nabla^s \delta \mathbf{s} : \boldsymbol{\sigma} d\Omega - \int_{\Omega} \delta \boldsymbol{\varepsilon} : \boldsymbol{\sigma} d\Omega + \int_{\Omega} \delta \boldsymbol{\sigma} : (\nabla^s \mathbf{s} - \boldsymbol{\varepsilon}) d\Omega \\ & + \int_{\Omega} \delta \boldsymbol{\varepsilon} : \mathbf{D} : \boldsymbol{\varepsilon} d\Omega - \int_{\Omega} \delta \mathbf{s} \cdot \mathbf{f} d\Omega - \int_{\partial\Omega_t} \delta \mathbf{s} \cdot \mathbf{t} dS = 0 \end{aligned} \quad (2.18)$$

where \mathbf{s} satisfies $\mathbf{s}|_{\partial\Omega_s} = \bar{\mathbf{s}}$, while $\boldsymbol{\sigma} \cdot \mathbf{n}|_{\partial\Omega_t} = \mathbf{t}$ is a natural boundary condition. As in the discussion of HR stationarities we call Equation (2.18) **HW grad-grad stationarity** because two gradient operators appear in the formulation. An example of the use of HW grad-grad stationarity (2.18) in multilayered plate modeling is presented by Auricchio and Sacco (1999).

2.5.2 HW div-div stationarity

A second HW stationarity formulation can be found introducing Equations (2.12) in Equation (2.18) obtaining:

$$\begin{aligned} \delta J_{HW}^{dd} = & - \int_{\Omega} \delta \mathbf{s} \cdot \nabla \cdot \boldsymbol{\sigma} d\Omega - \int_{\Omega} \delta \boldsymbol{\varepsilon} : \boldsymbol{\sigma} d\Omega - \int_{\Omega} \nabla \cdot \delta \boldsymbol{\sigma} \cdot \mathbf{s} d\Omega - \int_{\Omega} \delta \boldsymbol{\sigma} : \boldsymbol{\varepsilon} d\Omega \\ & + \int_{\Omega} \delta \boldsymbol{\varepsilon} : \mathbf{D} : \boldsymbol{\varepsilon} d\Omega - \int_{\Omega} \delta \mathbf{s} \cdot \mathbf{f} d\Omega + \int_{\partial\Omega_s} (\delta \boldsymbol{\sigma} \cdot \mathbf{n}) \cdot \bar{\mathbf{s}} dS = 0 \end{aligned} \quad (2.19)$$

where $\boldsymbol{\sigma}$ satisfies $\boldsymbol{\sigma} \cdot \mathbf{n} = \mathbf{t}$ on $\partial\Omega_t$, while $\mathbf{s}|_{\partial\Omega_s} = \bar{\mathbf{s}}$ is a natural boundary condition. We call Equation (2.19) **HW div-div stationarity** because two divergence operators appear in the formulation.

2.6 Other, Less Used Principles

An alternative problem formulation is to consider some stress components as dependent variables, expressing them *a-priori* in terms of the displacements. Reissner Mixed Variational Theorem approach, introduced by Reissner (1986), follows this approach: the out of plane stresses τ_{xy} and σ_{yy} are considered as independent variables while the axial stress σ_{xx} is expressed as a function of displacements; Carrera (2000, 2001), Carrera and Demasi (2002) and Demasi (2009a,b,c,d,e) derived different plate FE applying this viewpoint, with different choice of basis function and obtaining a reasonable accuracy in stress description.

Other alternatives exist, as an example (Pechstein and Schoberl, 2012) propose a functional that consider displacements and stresses as independent variables but uses different spaces with respect to the so far introduced HR formulations.

2.7 Conclusion on problem formulations

From the previous discussion (briefly summarized in Table 2.1 in terms of principles and equation formats) it is possible to draw some concluding remarks, listed in the following.

- All the considered weak problem formulations are symmetric.
- Every mixed weak formulation can be expressed in different formats: the grad-grad formulations (2.11) and (2.18) , and the div-div formulations (2.13) and (2.19). The former ones require to consider *a-priori* smooth displacement fields and less regular stress fields ($\mathbf{s} \in H^1(\Omega)$ and $\boldsymbol{\sigma} \in L^2(\Omega)$), while the latter ones demand *a-priori* less regular displacement fields and smooth stress fields ($\mathbf{s} \in L^2(\Omega)$ and $\boldsymbol{\sigma} \in H(\text{div}, \Omega)$).
- The grad-grad weak problem formulations ((2.11) and (2.18)) look up the displacement solution in the same spaces of TPE (2.7). As a consequence, under suitable hypothesis, the solution of the three so far introduced problem weak problem formulation are equivalent.
- When selecting the approximation fields for the mixed FE design, the combination of the regularity requirements and the well-posedness of the corresponding saddle point problems, typically leads to:
 - congruent models for the grad-grad formulations,
 - self-equilibrated models for the div-div formulations.

Since we think that one of the major limitations of the elementary available beam models is connected to the fact that equilibrium equations are not sufficiently enforced within the cross-section, in the following we focus on HR formulations but with some emphasis on the div-div form (2.13).

	Principle	
displacement-based	TPE	eq (2.7)
mixed	HR	grad-grad eq (2.11) div-div eq (2.13)
	HW	grad-grad eq (2.18) div-div eq (2.19)

Table 2.1: Obtained functional critical point classified in terms of functionals from which are derived and equation formats.

2.8 Applied procedures

In this section we introduce and discuss the mathematical procedures that will be applied in the following chapters in order to obtain the beam model and the corresponding FE.

2.8.1 Dimensional reduction

The **dimensional reduction** could be summarized in the following 3 step procedure.

- **First step.** A variational principle is selected for the elasticity problem (2.2). In particular, the functional spaces for the involved fields has to be appropriately chosen.
- **Second step.** For each involved field, a set of cross-section shape functions is selected. Typically, to develop a beam model, one chooses polynomial or piecewise polynomial shapes within the cross-section, while no profile restrictions are imposed along the axial direction. However, the approximation fields should fit the functional framework of the **First step** above, at least if a *conforming* model is considered.
- **Third step.** Integration within the cross-section is performed. This way, the n -dimensional variational problem is reduced to a 1D variational problem, which corresponds to a system of ODEs equipped with boundary conditions (i.e. the beam model).

2.8.1.1 Literature review

The so-far mentioned dimensional reduction method was proposed by Kantorovich and Krylov (1958) and it is a general mathematical procedure that exploits the geometry of the domain to reduce the problem dimension (in beam modelling from 3D PDEs to ODEs).

The method is widely used in continuum mechanic for the derivation of both plate and beam models. With respect to plate models we would cite, among other examples, Vogelius and Babuska (1981a,b); Alessandrini et al. (1999); Batra et al. (2002), and Batra and Vidoli (2002). Whereas with respect to beam models we would cite Dong et al. (2001); Kosmatka et al. (2001); Lin et al. (2001) who derive and discuss the homogeneous solution of a 3D semi-analytical solution for a beam body.

We notice also that the 3 step procedure summarized at the beginning of this section sometime is called *partial discretization process* (see e.g. Zienkiewicz and Taylor, 2000a) or *semi-analytical FE processes* (see e.g. Zienkiewicz and Taylor, 2000b).

2.8.1.2 Cross-section approximation

From a rigorous mathematical point of view, the second step in the dimensional reduction consists in the approximation of the generic field $\gamma : \Omega \rightarrow \mathbb{R}^{(\cdot)}$ as a linear combination of d **cross-section shape functions**, stored in a vector $\mathbf{r}_\gamma : A \rightarrow \mathbb{R}^{(\cdot) \times d}$, weighted with arbitrary **axial coefficient functions** $\hat{\gamma} : l \rightarrow \mathbb{R}^d$, i.e.

$$\gamma(x, \mathbf{y}) \approx \mathbf{r}_\gamma^T(\mathbf{y})(x, \mathbf{y}) \hat{\gamma}(x) \quad (2.20)$$

where $(\cdot)^T$ indicates the transposition operation.

We emphasize that the cross-section shape functions $\mathbf{r}_\gamma : A \rightarrow \mathbb{R}^{(\cdot) \times d}$ are a set of pre-assigned, linearly-independent functions. As a consequence, the field $\gamma : \Omega \rightarrow \mathbb{R}^{(\cdot)}$ is uniquely determined by the axial coefficient functions $\hat{\gamma} : l \rightarrow \mathbb{R}^d$ that are indeed the *unknowns* of the beam model we are developing.

2.8.2 FE derivation procedure

The FE derivation procedure could be summarized in the following 3 step procedure.

- **First step.** A variational principle is selected for the beam model. In particular, the functional spaces for the involved fields has to be appropriately chosen.
- **Second step.** For each involved field, an axis approximation is selected. Typically, to develop a beam FE, one chooses polynomial or piecewise polynomial shapes along the axis direction. However, the approximation fields should fit the functional framework of the **First step** above, at least if a *conforming* model is considered.
- **Third step.** Integration along the axis is performed. This way, the 1D variational problem is reduced to an algebraic problem, which corresponds to a system of algebraic linear equations.

2.8.2.1 Axial approximation

From a rigorous mathematical point of view, the second step in the FE derivation procedure consists in the approximation of the generic axial coefficient function $\hat{\gamma}$ as a linear combination of t **axis shape functions**, stored in a vector $\mathbf{N}_{\gamma i} : l \rightarrow \mathbb{R}^t$, weighted with arbitrary **numerical coefficients** $\tilde{\gamma}_i \in \mathbb{R}^t$, i.e.

$$\hat{\gamma}(x) \approx \mathbf{N}_\gamma(x) \tilde{\gamma} \quad (2.21)$$

where

$$\mathbf{N}_\gamma = \begin{bmatrix} \mathbf{N}_{\gamma_1}^T(x) & \mathbf{0} & \cdots & \mathbf{0} \\ \mathbf{0} & \mathbf{N}_{\gamma_2}^T(x) & \cdots & \mathbf{0} \\ \vdots & \vdots & \ddots & \vdots \\ \mathbf{0} & \mathbf{0} & \cdots & \mathbf{N}_{\gamma_d}^T(x) \end{bmatrix}; \quad \tilde{\boldsymbol{\gamma}} = \begin{Bmatrix} \tilde{\gamma}_1 \\ \tilde{\gamma}_2 \\ \vdots \\ \tilde{\gamma}_d \end{Bmatrix}$$

In the following, we drop the explicit dependence of \mathbf{N}_γ on x for notational simplicity.

2.8.3 Conclusion on applied procedure

As highlighted in Sections 2.8.1 and 2.8.2, from an abstract point of view, both the mathematical procedures consist of the same three steps.

The whole procedure (dimensional reduction and FE derivation) could be seen as a full-discretization procedure. From this point of view, the result of the steps so far described has some similarities with the tensor product discretisation that exploits the domain structure (for the problem under investigation see Equation (2.1)) and constructs a FE space Σ_Ω as the tensor product of approximations defined in each sub-region $\Sigma_\Omega := \Sigma_l \otimes \Sigma_A$. We notice that the tensor product discretisation is sometime used also in plate modelling, as illustrated in (Pechstein and Schoberl, 2012).

Nevertheless, distinguish the two steps leads the following advantages:

- the possibility to manage independently the cross-section and the axis approximations considering both the weak formulation with the associated spaces and the approximation accuracy,
- the capability to investigate and discuss the model properties.

Moreover, we highlight also that the two separate discretization procedures allow to make careful and optimized choices with respect to the different domain-subsets. As a consequence, we can consider extremely distorted meshes, with element sizes that could have different order of magnitude with respect to the cross-section and the axis directions. This choice could represent a problem looking at the whole discretisation procedure, on the other hand it represents the standard in beam FE discretisation.

Chapter 3

2D Beam–model

In this chapter we are going to consider a 2D elastic problem, i.e. with respect to the notation introduced in Chapter 2 we assume $n = 2$. As a consequence, the cross-section coordinates reduce to the scalar value y . Figure 3.1 represents the domain, the adopted Cartesian coordinate system, the initial and the final cross sections A_0 and A_l respectively, and the lateral surface L for the case we are considering. With respect to the notations introduced in Section 2.8.1.2, we have that $\gamma(x, y)$, $\mathbf{r}_\gamma(y)$ and $\hat{\gamma}(x)$.

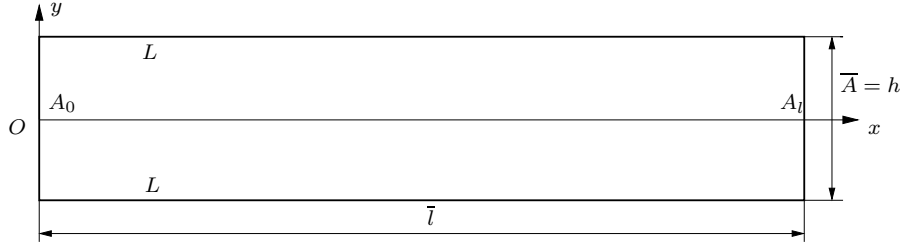


Figure 3.1: 2D beam geometry, Cartesian coordinate system, dimensions, and adopted notations.

Section 3.1 specializes the notations introduced in Chapter 2 to the 2D case. Section 3.2 specifies the boundary conditions of the 2D problem. Sections 3.3 and 3.4 formulate the TPE and the HR based beam models respectively, discuss the analytical solution of some beam model examples, formulate the corresponding FEs, and provide some numerical examples. Finally, Section 3.5 provides some information about the computational time and the numerical efficiency of the proposed methods.

3.1 Profile approximation and notations

Adopting notation introduced in (2.20) and switching now to an engineering notation we set:

$$\mathbf{s}(x, y) = \begin{Bmatrix} s_u(x, y) \\ s_v(x, y) \end{Bmatrix} = \begin{bmatrix} \mathbf{r}_u^T(y) & \mathbf{0} \\ \mathbf{0} & \mathbf{r}_v^T(y) \end{bmatrix} \begin{Bmatrix} \hat{\mathbf{u}}(x) \\ \hat{\mathbf{v}}(x) \end{Bmatrix} = \mathbf{R}_s \hat{\mathbf{s}} \quad (3.1)$$

$$\boldsymbol{\sigma}(x, y) = \begin{Bmatrix} \sigma_{xx}(x, y) \\ \sigma_{yy}(x, y) \\ \tau_{xy}(x, y) \end{Bmatrix} = \begin{bmatrix} \mathbf{r}_{\sigma_x}^T(y) & \mathbf{0} & \mathbf{0} \\ \mathbf{0} & \mathbf{r}_{\sigma_y}^T(y) & \mathbf{0} \\ \mathbf{0} & \mathbf{0} & \mathbf{r}_\tau^T(y) \end{bmatrix} \begin{Bmatrix} \hat{\sigma}_x(x) \\ \hat{\sigma}_y(x) \\ \hat{\tau}(x) \end{Bmatrix} = \mathbf{R}_\sigma \hat{\boldsymbol{\sigma}} \quad (3.2)$$

where, for \mathbf{R}_s and \mathbf{R}_σ ($\hat{\mathbf{s}}$ and $\hat{\boldsymbol{\sigma}}$, respectively), we drop the explicit dependence on y (x , respectively), for notational simplicity. Virtual fields are analogously defined as:

$$\delta \mathbf{s} = \mathbf{R}_s \delta \hat{\mathbf{s}} \quad \delta \boldsymbol{\sigma} = \mathbf{R}_\sigma \delta \hat{\boldsymbol{\sigma}}$$

We remark that, due to assumption (2.20), computation of partial derivatives is straightforward, since it holds:

$$\frac{\partial}{\partial x} \gamma = \frac{\partial}{\partial x} (\mathbf{r}_\gamma^T \hat{\boldsymbol{\gamma}}) = \mathbf{r}_\gamma^T \frac{d}{dx} \hat{\boldsymbol{\gamma}} = \mathbf{r}_\gamma^T \hat{\boldsymbol{\gamma}}' \quad \frac{\partial}{\partial y} \gamma = \frac{\partial}{\partial y} (\mathbf{r}_\gamma^T \hat{\boldsymbol{\gamma}}) = \frac{d}{dy} \mathbf{r}_\gamma^T \hat{\boldsymbol{\gamma}} = \mathbf{r}_\gamma'^T \hat{\boldsymbol{\gamma}}$$

where we use a prime to indicate derivatives both along x and along y , because there is no risk of confusion.

Coherently with the engineering notation just introduced, in Table 3.1 we re-define the differential operators and the outward unit vector product where

$$\mathbf{E}_1 = \begin{bmatrix} 1 & 0 & 0 \\ 0 & 0 & 1 \end{bmatrix} \quad \mathbf{E}_2 = \begin{bmatrix} 0 & 0 & 1 \\ 0 & 1 & 0 \end{bmatrix}$$

The products between partial derivatives and boolean matrices \mathbf{E}_i , $i = 1, 2$ must be intended as scalar-matrix products, whereas differential operators are applied to stress approximations $\mathbf{R}_\sigma \hat{\boldsymbol{\sigma}}$.

In Chapter 2, with \mathbf{D}^{-1} we denoted the fourth order elastic tensor while in this chapter, we use the same notation to indicate the corresponding square matrix obtained following engineering notation. Therefore, we have:

$$\mathbf{D}^{-1} = \frac{1}{E} \begin{bmatrix} 1 & -\nu & 0 \\ -\nu & 1 & 0 \\ 0 & 0 & 2(1+\nu) \end{bmatrix}$$

where E and ν indicate the Young's modulus and the Poisson's coefficient respectively.

Tensorial notation	Engineering notation
$\nabla \cdot \boldsymbol{\sigma}$	$\left(\frac{d}{dx} \mathbf{E}_1 + \frac{d}{dy} \mathbf{E}_2 \right) \mathbf{R}_\sigma \hat{\boldsymbol{\sigma}}$
$\nabla^S \mathbf{s}$	$\left(\frac{d}{dx} \mathbf{E}_1^T + \frac{d}{dy} \mathbf{E}_2^T \right) \mathbf{R}_s \hat{\mathbf{s}}$
$\boldsymbol{\sigma} \cdot \mathbf{n}$	$(n_x \mathbf{E}_1 + n_y \mathbf{E}_2) \mathbf{R}_\sigma \hat{\boldsymbol{\sigma}}$

Table 3.1: Tensorial and Engineering equivalent notations.

3.2 Problem formulation

In the following, we consider the special case of a beam for which it holds:

$$\bar{\mathbf{s}} = \mathbf{0} \quad \text{on } A_0 = \partial\Omega_s, \quad (3.3)$$

$$\mathbf{t} \neq \mathbf{0} \quad \text{on } A_l \quad (3.4)$$

$$\mathbf{t} = \mathbf{0} \quad \text{on } S_0 \cup S_n \quad (3.5)$$

Hence, $\partial\Omega_t = A_l \cup S_0 \cup S_n$; moreover, the beam is clamped on the left-hand side A_0 , and it is subjected to a non-vanishing traction field on the right-hand side A_l .

Furthermore, we suppose that the external load $\mathbf{t}|_{A_l}$ can be exactly represented using the chosen profiles for $\boldsymbol{\sigma} \cdot \mathbf{n}$. Recalling (3.2), and noting that $\mathbf{n}|_{A_l} = (1, 0)^T$, this means that there exist suitable vectors $\hat{\mathbf{t}}_x$ and $\hat{\mathbf{t}}_y$ such that

$$\mathbf{t} = \begin{Bmatrix} \mathbf{R}_{\sigma_x}^T \hat{\mathbf{t}}_x \\ \mathbf{R}_{\tau}^T \hat{\mathbf{t}}_y \end{Bmatrix} \quad (3.6)$$

Therefore, the boundary condition $\boldsymbol{\sigma} \cdot \mathbf{n}|_{A_l} = \mathbf{t}$ may be written as (cf. (3.2))

$$\begin{Bmatrix} \hat{\boldsymbol{\sigma}}_x(\bar{l}) \\ \hat{\boldsymbol{\tau}}(\bar{l}) \end{Bmatrix} = \begin{Bmatrix} \hat{\mathbf{t}}_x \\ \hat{\mathbf{t}}_y \end{Bmatrix} \quad (3.7)$$

We also remark that all these assumptions can be modified to cover more general cases; nonetheless, this simple model is already adequate to illustrate the method capabilities. Moreover, we notice that the assumption on external load (3.6) is necessary only for the development of mixed beam model illustrated in Section 3.4.1.2.

3.3 Total Potential Energy based beam model

In this section, starting from the 2D problem weak formulation (2.7), we perform the dimensional reduction which is based on the introduction of field cross-section approximations and on a cross-section integration. For simplicity, in the model derivation, we switch to an engineering-oriented notation.

3.3.1 Model formulation

In the following we assume that $\partial\Omega_t = A_l \cup L$, and the lateral surface is unloaded, i.e.: $\mathbf{t}|_L = \mathbf{0}$. The unloaded lateral surface is an usual assumption in beam modelling. However, we notice that the model derivation can be performed taking into account arbitrary load conditions as well.

Introducing the engineering notation and the approximations defined in Section 2.8.1.2, variational problem (2.7) becomes:

$$\begin{aligned} \delta J_{TPE} = & \int_{\Omega} \left[\delta \hat{\mathbf{s}}^T \mathbf{R}_s^T \left(\frac{d}{dx} \mathbf{E}_1 + \frac{\partial}{\partial y} \mathbf{E}_2 \right) \right] \mathbf{D} \left[\left(\frac{d}{dx} \mathbf{E}_1^T + \frac{\partial}{\partial y} \mathbf{E}_2^T \right) \mathbf{R}_s \hat{\mathbf{s}} \right] d\Omega \\ & - \int_{\Omega} \delta \hat{\mathbf{s}}^T \mathbf{R}_s^T \mathbf{f} d\Omega - \int_{\partial\Omega_t} \delta \hat{\mathbf{s}}^T \mathbf{R}_s^T \mathbf{t} dA = 0 \end{aligned} \quad (3.8)$$

Expanding products, introducing the derivative notation introduced in Table 3.1, and recalling that $\partial\Omega_s = A_0$, Equation (3.8) becomes:

$$\begin{aligned} \delta J_{TPE} = & \int_{\Omega} \left(\delta \hat{\mathbf{s}}'^T \mathbf{R}_s^T \mathbf{E}_1 \mathbf{D} \mathbf{E}_1 \mathbf{R}_s \hat{\mathbf{s}}' + \delta \hat{\mathbf{s}}'^T \mathbf{R}_s^T \mathbf{E}_1 \mathbf{D} \mathbf{E}_2 \mathbf{R}_s' \hat{\mathbf{s}} + \right. \\ & \left. \delta \hat{\mathbf{s}}^T \mathbf{R}_s'^T \mathbf{E}_2 \mathbf{D} \mathbf{E}_1 \mathbf{R}_s \hat{\mathbf{s}}' + \delta \hat{\mathbf{s}}^T \mathbf{R}_s'^T \mathbf{E}_2 \mathbf{D} \mathbf{E}_2 \mathbf{R}_s' \hat{\mathbf{s}} - \delta \hat{\mathbf{s}}^T \mathbf{R}_s^T \mathbf{f} \right) d\Omega + \\ & \int_{A_l} \delta \hat{\mathbf{s}}^T \mathbf{R}_s^T \mathbf{t} dA = 0 \end{aligned} \quad (3.9)$$

Splitting the integral on the domain Ω into an integral along the axis l and an integral on the cross section A , Equation (3.9) becomes:

$$\delta J_{TPE} = \int_l \left(\delta \hat{\mathbf{s}}'^T \mathbf{A}^{TPE} \hat{\mathbf{s}}' + \delta \hat{\mathbf{s}}'^T \mathbf{B}_{s's}^{TPE} \hat{\mathbf{s}} + \delta \hat{\mathbf{s}}^T \mathbf{B}_{ss'}^{TPE} \hat{\mathbf{s}}' + \delta \hat{\mathbf{s}}^T \mathbf{C}^{TPE} \hat{\mathbf{s}} - \delta \hat{\mathbf{s}}^T \mathbf{F} \right) dx + \delta \hat{\mathbf{s}}^T \Big|_{\bar{l}} \mathbf{T} = 0 \quad (3.10)$$

where

$$\begin{aligned}
\mathbf{A}^{TPE} &:= \int_A \mathbf{R}_s^T \mathbf{E}_1 \mathbf{D} \mathbf{E}_1 \mathbf{R}_s dA \\
\mathbf{B}_{s's'}^{TPE} &= (\mathbf{B}_{ss'}^{TPE})^T := \int_A \mathbf{R}_s^T \mathbf{E}_1 \mathbf{D} \mathbf{E}_2 \mathbf{R}'_s dA \\
\mathbf{C}^{TPE} &:= \int_A \mathbf{R}_s'^T \mathbf{E}_2 \mathbf{D} \mathbf{E}_2 \mathbf{R}'_s dA \\
\mathbf{F} &:= \int_A \mathbf{R}_s^T \mathbf{f} dA; \quad \mathbf{T} := \int_{A_l} \mathbf{R}_s^T \mathbf{t} dA;
\end{aligned} \tag{3.11}$$

Equation (3.10) represents the weak formulation of the beam model: the integrals are defined only along the beam axis, whereas the cross-section integrals become coefficient matrices.

To obtain the corresponding strong formulation, i.e. the associated ODE system, we need to integrate by parts the third term of Equation (3.10):

$$\begin{aligned}
\int_l \delta \hat{\mathbf{s}}'^T \mathbf{A}^{TPE} \hat{\mathbf{s}}' dx &= \delta \hat{\mathbf{s}}^T \mathbf{A}^{TPE} \hat{\mathbf{s}}' \Big|_{x=0}^{x=\bar{l}} - \int_l \delta \hat{\mathbf{s}}^T \mathbf{A}^{TPE} \hat{\mathbf{s}}'' dx \\
\int_l \delta \hat{\mathbf{s}}'^T \mathbf{B}_{s's'}^{TPE} \hat{\mathbf{s}} dx &= \delta \hat{\mathbf{s}}^T \mathbf{B}_{s's'}^{TPE} \hat{\mathbf{s}} \Big|_{x=0}^{x=\bar{l}} - \int_l \delta \hat{\mathbf{s}}'^T \mathbf{B}_{s's'}^{TPE} \hat{\mathbf{s}}' dx
\end{aligned} \tag{3.12}$$

Substituting Equation (3.12) in Equation (3.10) and recalling that $\delta \hat{\mathbf{s}}(0) = \mathbf{0}$, we obtain:

$$\begin{aligned}
&\int_l \delta \hat{\mathbf{s}}^T (-\mathbf{A}^{TPE} \hat{\mathbf{s}}'' + \mathbf{B}^{TPE} \hat{\mathbf{s}}' + \mathbf{C}^{TPE} \hat{\mathbf{s}} - \mathbf{F}) dx \\
&- \delta \hat{\mathbf{s}}^T (\mathbf{T} + \mathbf{A}^{TPE} \hat{\mathbf{s}}'|_{\bar{l}} + \mathbf{B}_{s's'}^{TPE} \hat{\mathbf{s}}|_{\bar{l}}) = 0
\end{aligned} \tag{3.13}$$

where $\mathbf{B}^{TPE} = -\mathbf{B}_{s's'}^{TPE} + \mathbf{B}_{ss'}^{TPE}$.

Since Equation (3.13) needs to be satisfied for all the possible virtual fields, we obtain the following ODE, equipped with the essential boundary condition (3.3).

$$\begin{cases} -\mathbf{A}^{TPE} \hat{\mathbf{s}}'' + \mathbf{B}^{TPE} \hat{\mathbf{s}}' + \mathbf{C}^{TPE} \hat{\mathbf{s}} = \mathbf{F} & \text{in } l \\ +\mathbf{A}^{TPE} \hat{\mathbf{s}}' + \mathbf{B}_{s's'}^{TPE} \hat{\mathbf{s}} = -\mathbf{T} & \text{at } x = \bar{l} \\ \hat{\mathbf{s}} = \mathbf{0} & \text{at } x = 0 \end{cases} \tag{3.14}$$

3.3.2 Beam-model examples

In this section we give three examples of beam models. More precisely, considering a beam of thickness $\bar{A} = h$ and starting from the TPE approach (Equation (3.14)), we derive:

1. a single layer beam model in which we use a first order displacement field; by means of this example we will show that the approach under discussion is not able to reproduce the classical models;
2. a single layer beam model in which we use an high order displacement field; by means of this example we will show that, in order to reproduce the classical models, we need refined displacement fields;
3. a multilayer beam model, in which we consider also higher order kinematic and stress fields; by means of this example we will illustrate how the approach could produce a refined model with a reasonable solution.

3.3.2.1 First order, single layer beam

Considering a homogeneous beam, we assume a first-order kinematic (as in Timoshenko model) . In other words we make the following hypotheses:

$$\begin{aligned} u &= u_0(x) + y u_1(x) & \text{i.e.} & \quad \mathbf{r}_u = \begin{Bmatrix} 1 \\ y \end{Bmatrix} & \quad \hat{\mathbf{u}} = \begin{Bmatrix} u_0 \\ u_1 \end{Bmatrix} \\ v &= v(x) & \text{i.e.} & \quad \mathbf{r}_v = \{1\} & \quad \hat{\mathbf{v}} = \{v\} \end{aligned}$$

The matrices \mathbf{A}^{TPE} , \mathbf{B}^{TPE} , and \mathbf{C}^{TPE} defined in Equations (3.11) and entering into the beam model (3.14), are explicitly given by:

$$\begin{aligned} \mathbf{A}^{TPE} &= \begin{bmatrix} h \frac{E}{1-\nu^2} & 0 & 0 \\ 0 & \frac{h^3 E}{12(1-\nu^2)} & 0 \\ 0 & 0 & h \frac{E}{2(1+\nu)} h \end{bmatrix} \\ \mathbf{B}^{TPE} &= \begin{bmatrix} 0 & 0 & 0 \\ 0 & 0 & -h \frac{E}{2(1+\nu)} \\ 0 & h \frac{E}{2(1+\nu)} & 0 \end{bmatrix} \\ \mathbf{C}^{TPE} &= \begin{bmatrix} 0 & 0 & 0 \\ 0 & -h \frac{E}{2(1+\nu)} & 0 \\ 0 & 0 & 0 \end{bmatrix} \end{aligned} \tag{3.15}$$

The matrices defined in (3.15) lead the following ODE system:

$$\begin{cases} h \frac{E}{1-\nu^2} u_0'' = 0 \\ \frac{h^3 E}{12(1-\nu^2)} u_1'' - \frac{Eh}{2(1+\nu)} (v' + u_1) = 0 \\ \frac{Eh}{2(1+\nu)} (v'' + u_1') = 0 \\ + \text{suitable boundary conditions} \end{cases} \tag{3.16}$$

Therefore, not surprisingly, we recover the classical Timoshenko equations, where, unfortunately, the shear correction factor (5/6) does not appear.

3.3.2.2 High order, single layer beam

Considering a homogeneous beam, we assume an high-order kinematic (as the one considered in (Lo et al., 1977a)). In other words we make the following hypotheses:

$$\begin{aligned} u &= u_0(x) + y u_1(x) + y^2 u_2(x) + y^3 u_3(x) & \text{i.e.} & \quad \mathbf{r}_u = \begin{Bmatrix} 1 \\ y \\ y^2 \\ y^3 \end{Bmatrix} & \quad \hat{\mathbf{u}} = \begin{Bmatrix} u_0 \\ u_1 \\ u_2 \\ u_3 \end{Bmatrix} \\ v &= v_0(x) + y v_1(x) + y^2 v_2(x) & \text{i.e.} & \quad \mathbf{r}_v = \begin{Bmatrix} 1 \\ y \\ y^2 \end{Bmatrix} & \quad \hat{\mathbf{v}} = \begin{Bmatrix} v_0 \\ v_1 \\ v_2 \end{Bmatrix} \end{aligned}$$

The matrices \mathbf{A}^{TPE} , \mathbf{B}^{TPE} , and \mathbf{C}^{TPE} defined in Equations (3.11) and entering into the beam model (3.14), are explicitly given by:

$$\begin{aligned}
 \mathbf{A}^{TPE} &= \frac{E}{1+\nu} \begin{bmatrix} \frac{h}{1-\nu} & 0 & \frac{h^3}{12(1-\nu)} & 0 & 0 & 0 & 0 \\ 0 & \frac{h^3}{12(1-\nu)} & 0 & \frac{h^5}{80(1-\nu)} & 0 & 0 & 0 \\ \frac{h^3}{12(1-\nu)} & 0 & \frac{h^5}{80(1-\nu)} & 0 & 0 & 0 & 0 \\ 0 & \frac{h^5}{80(1-\nu)} & 0 & \frac{h^7}{448(1-\nu)} & 0 & 0 & 0 \\ 0 & 0 & 0 & 0 & \frac{h}{2} & 0 & \frac{h^3}{24} \\ 0 & 0 & 0 & 0 & 0 & \frac{h^3}{24} & 0 \\ 0 & 0 & 0 & 0 & \frac{h^3}{24} & 0 & \frac{h^5}{160} \end{bmatrix} \\
 \mathbf{B}^{TPE} &= \frac{E}{1+\nu} \begin{bmatrix} 0 & 0 & 0 & 0 & 0 & \frac{h\nu}{1-\nu} & 0 \\ 0 & 0 & 0 & 0 & -\frac{h}{2} & 0 & -\frac{h^3(1-5\nu)}{24(1-\nu)} \\ 0 & 0 & 0 & 0 & 0 & -\frac{h^3(1-2\nu)}{12(1-\nu)} & 0 \\ 0 & 0 & 0 & 0 & -\frac{h^3}{8} & 0 & -\frac{h^5(3-7\nu)}{320(1-\nu)} \\ 0 & \frac{h}{2} & 0 & \frac{h^3}{8} & 0 & 0 & 0 \\ \frac{h\nu}{1-\nu} & 0 & \frac{h^3(1-2\nu)}{12(1-\nu)} & 0 & 0 & 0 & 0 \\ 0 & \frac{h^3(1-5\nu)}{24(1-\nu)} & 0 & \frac{h^5(3-7\nu)}{160(1-\nu)} & 0 & 0 & 0 \end{bmatrix} \quad (3.17) \\
 \mathbf{C}^{TPE} &= \frac{E}{1+\nu} \begin{bmatrix} 0 & 0 & 0 & 0 & 0 & 0 & 0 \\ 0 & -\frac{h}{2} & 0 & \frac{h^3}{8} & 0 & 0 & 0 \\ 0 & 0 & \frac{h^3}{6} & 0 & 0 & 0 & 0 \\ 0 & \frac{h^3}{8} & 0 & \frac{9h^5}{160} & 0 & 0 & 0 \\ 0 & 0 & 0 & 0 & 0 & 0 & 0 \\ 0 & 0 & 0 & 0 & 0 & \frac{h}{(1-\nu)} & 0 \\ 0 & 0 & 0 & 0 & 0 & 0 & \frac{h^3}{3(1-\nu)} \end{bmatrix}
 \end{aligned}$$

3.3.2.3 Multilayer beam

We now consider a beam composed by n layers. The geometric and material parameters for the generic i -th layer are defined by the thickness h_i , the Young's modulus E_i and the Poisson ratio ν_i , collected in the n -dimensional vectors \mathbf{h} , \mathbf{E} and $\boldsymbol{\nu}$, respectively.

To design a multilayer beam model, we follow the two-step procedure described below.

1. In each layer, we choose suitable profiles for every field involved in the modeling. Of course, given a generic field, the simplest choice, which is the one we use in this paper, is to use the same profiles for every layer.
2. Across each interlayer, we impose the necessary continuity to ensure that the displacements belong to $H^1(\Omega)$.

As a consequence, given a generic field γ , it is possible to define its profile vector \mathbf{r}_γ , which is characterized by:

- The highest polynomial degree, with respect to y , used in a generic layer. This number is denoted by $\deg(\mathbf{r}_\gamma)$ in what follows.
- The regularity across each interlayer: in the following, C^{-1} stands for no continuity requirement, C^0 for standard continuity requirement.

We thus select the involved fields according to Table 3.2, where we also show the number of layer and global DOFs.

	$\deg(\mathbf{r}_\gamma)$	inter-layer continuity	layer DOF	global DOF
\mathbf{r}_u	3	C^0	4	$3n+1$
\mathbf{r}_v	2	C^0	3	$2n+1$

Table 3.2: Polynomial degrees of the profiles vectors, continuity properties and number of DOFs for a multilayer beam.

We now present an easy case to illustrate the model capabilities. More precisely, we consider a *homogeneous* beam, but we treat it as if it were formed by three layers. Thus, the geometric and material properties are described by:

$$\mathbf{h} = \begin{Bmatrix} 0.300 \\ 0.367 \\ 0.333 \end{Bmatrix} [\text{mm}] \quad \mathbf{E} = \begin{Bmatrix} 10^5 \\ 10^5 \\ 10^5 \end{Bmatrix} [\text{MPa}] \quad \boldsymbol{\nu} = \begin{Bmatrix} 0.25 \\ 0.25 \\ 0.25 \end{Bmatrix} [-]$$

The term h_i of the vector \mathbf{h} defines the thickness of the i -th layer constituting the beam, numbered from the bottom to the top; analogously the terms of vectors \mathbf{E} and $\boldsymbol{\nu}$ define the mechanical properties of the layers. We now give the solution of the generalized eigenvalue problem $\det(\lambda^2 \mathbf{A}^{TPE} + \lambda \mathbf{B}^{TPE} + \mathbf{C}^{TPE}) = 0$, which enters in the construction of the homogeneous solution of (3.14).

$$\lambda = \begin{Bmatrix} \sim 0 \\ \pm 10.116 \\ \pm 12.064 \\ \pm 23.614 \\ \pm 27.443 \\ \pm 19.155 \pm 2.959i \\ \pm 13.602 \pm 2.581i \\ \pm 24.439 \pm 5.185i \\ \pm 7.536 \pm 2.748i \end{Bmatrix} \begin{matrix} [6] \\ [2] \\ [2] \\ [2] \\ [2] \\ [4] \\ [4] \\ [4] \\ [4] \end{matrix}$$

where in square brackets we show the eigenvalue multiplicities, and we used the symbol ~ 0 to denote eigenvalues which vanish up to the machine precision.

It is possible to evaluate also the homogeneous solution but, given the problem complexity, it is huge and we will not report it. Nevertheless it is possible to discuss its structure and made some important remarks.

- The zero eigenvalues lead to polynomial terms analogous to the Timoshenko homogeneous solution described in Section 3.4.3.1.
- The complex conjugate eigenvalues ($a \pm ib$) lead to functions like $C_i e^{ax} \sin(bx + C_j)$, which describe local effects near the boundaries, as it happens in several other beam models (see Ladeveze and Simmonds, 1998; Allix and Dupleix-Couderc, 2010; Dauge et al., 2002).

3.3.3 Finite Element derivation

The goal of this section is to obtain a displacement-based beam FE formulation. Accordingly, we introduce an approximation along the x direction, and perform an integration along the axis. The procedure reduces the algebraic-differential equation system (3.10) to a pure algebraic equation system.

3.3.3.1 FE formulation

In the following, we assume that the beam is clamped in A_0 , i.e. $\bar{\mathbf{s}} = \mathbf{0}$.

The FE discretization of the model follows from the introduction of the axial shape function approximation (2.21) into the beam-model weak formulation (3.10):

$$\begin{aligned} \delta J_{TPE} = \int_l \left(\delta \tilde{\mathbf{s}}^T \mathbf{N}_s'^T \mathbf{A}^{TPE} \mathbf{N}_s' \tilde{\mathbf{s}} + \delta \tilde{\mathbf{s}}^T \mathbf{N}_s'^T \mathbf{B}_{s's'}^{TPE} \mathbf{N}_s \tilde{\mathbf{s}} + \delta \tilde{\mathbf{s}}^T \mathbf{N}_s^T \mathbf{B}_{ss'}^{TPE} \mathbf{N}_s' \tilde{\mathbf{s}} + \right. \\ \left. \delta \tilde{\mathbf{s}}^T \mathbf{N}_s^T \mathbf{C}^{TPE} \mathbf{N}_s' \tilde{\mathbf{s}} - \delta \tilde{\mathbf{s}}^T \mathbf{N}_s^T \mathbf{F} \right) dx + \delta \tilde{\mathbf{s}}^T \mathbf{N}_s^T|_{\bar{l}} \mathbf{T} = 0 \end{aligned} \quad (3.18)$$

Collecting unknown coefficients in a vector and requiring (3.18) to be satisfied for all possible virtual fields, we obtain the following algebraic equation system:

$$\mathbf{K}^{TPE} \tilde{\mathbf{s}} = \tilde{\mathbf{F}} \quad (3.19)$$

where

$$\begin{aligned} \mathbf{K}^{TPE} &:= \int_l (\mathbf{N}_s'^T \mathbf{A}^{TPE} \mathbf{N}_s' + \mathbf{N}_s'^T \mathbf{B}_{s's'}^{TPE} \mathbf{N}_s + \mathbf{N}_s^T \mathbf{B}_{ss'}^{TPE} \mathbf{N}_s' + \mathbf{N}_s^T \mathbf{C}^{TPE} \mathbf{N}_s') dx \\ \tilde{\mathbf{F}} &:= \int_l \mathbf{N}_s^T \mathbf{F} dx + \mathbf{N}_s^T|_{x=\bar{l}} \mathbf{T} \end{aligned} \quad (3.20)$$

We highlight that the weak formulation (3.18) is symmetric.

3.3.3.2 Axial shape functions definition

In Table 3.3 we introduce the shape-function properties that we use in numerical examples, together with the cross-section shape-function properties. We notice that choices illustrated in

Variable	deg (\mathbf{r}_γ)	y cont.	deg (\mathbf{N}_γ)	x cont.
u	1	C^0	2	C^0
v	2	C^0	3	C^0

Table 3.3: Degree and continuity of cross-section profile functions and axis shape functions for the TPE- based FE.

Table 3.3 are arbitrary.

3.4 HR-based beam models

In this section we develop some mixed beam models. Referring to the procedure described in Chapter 2.8, we will start from the HR variational formulations of Section 2.4 (cf. **First step**), we will define the approximated fields (cf. **Second step**), and perform the integration along the thickness (cf. **Third step**). Moreover, to simplify the further discussions, we will switch to an engineering notation.

3.4.1 Model formulation

3.4.1.1 grad-grad approach

Using the notations introduced in Subsection 3.1 the HR grad-grad stationarity (2.11) becomes:

$$\begin{aligned} \delta J_{HR}^{gg} = & \int_{\Omega} \left[\left(\frac{d}{dx} \mathbf{E}_1^T + \frac{d}{dy} \mathbf{E}_2^T \right) \mathbf{R}_s \delta \hat{\mathbf{s}} \right]^T \mathbf{R}_{\sigma} \hat{\boldsymbol{\sigma}} d\Omega + \int_{\Omega} \delta \hat{\boldsymbol{\sigma}}^T \mathbf{R}_{\sigma}^T \left[\left(\frac{d}{dx} \mathbf{E}_1^T + \frac{d}{dy} \mathbf{E}_2^T \right) \mathbf{R}_s \hat{\mathbf{s}} \right] d\Omega \\ & - \int_{\Omega} \delta \hat{\boldsymbol{\sigma}}^T \mathbf{R}_{\sigma}^T \mathbf{D}^{-1} \mathbf{R}_{\sigma} \hat{\boldsymbol{\sigma}} d\Omega - \int_{\Omega} \delta \hat{\mathbf{s}}^T \mathbf{R}_s^T \mathbf{f} d\Omega - \int_{\partial\Omega_t} \delta \hat{\mathbf{s}}^T \mathbf{R}_s^T \mathbf{t} dy = 0 \end{aligned} \quad (3.21)$$

Expanding Equation (3.21) we obtain:

$$\begin{aligned} \delta J_{HR}^{gg} = & \int_{\Omega} \left(\delta \hat{\mathbf{s}}'^T \mathbf{R}_s^T \mathbf{E}_1 \mathbf{R}_{\sigma} \hat{\boldsymbol{\sigma}} + \delta \hat{\mathbf{s}}^T \mathbf{R}_s'^T \mathbf{E}_2 \mathbf{R}_{\sigma} \hat{\boldsymbol{\sigma}} \right) d\Omega + \int_{\Omega} \left(\delta \hat{\boldsymbol{\sigma}}^T \mathbf{R}_{\sigma}^T \mathbf{E}_1^T \mathbf{R}_s \hat{\mathbf{s}}' + \delta \hat{\boldsymbol{\sigma}}^T \mathbf{R}_{\sigma}^T \mathbf{E}_2^T \mathbf{R}_s' \hat{\mathbf{s}} \right) d\Omega \\ & - \int_{\Omega} \left(\delta \hat{\boldsymbol{\sigma}}^T \mathbf{R}_{\sigma}^T \mathbf{D}^{-1} \mathbf{R}_{\sigma} \hat{\boldsymbol{\sigma}} + \delta \hat{\mathbf{s}}^T \mathbf{R}_s^T \mathbf{f} \right) d\Omega - \int_{A_t} \delta \hat{\mathbf{s}}^T \mathbf{R}_s^T \mathbf{t} dy = 0 \end{aligned} \quad (3.22)$$

By using Fubini-Tonelli theorem, Equation (3.22) can be written as:

$$\delta J_{HR}^{gg} = \int_l \left(\delta \hat{\mathbf{s}}'^T \mathbf{G}_{s\sigma} \hat{\boldsymbol{\sigma}} + \delta \hat{\mathbf{s}}^T \mathbf{H}_{s'\sigma} \hat{\boldsymbol{\sigma}} + \delta \hat{\boldsymbol{\sigma}}^T \mathbf{G}_{\sigma s} \hat{\mathbf{s}}' + \delta \hat{\boldsymbol{\sigma}}^T \mathbf{H}_{\sigma s'} \hat{\mathbf{s}} - \delta \hat{\boldsymbol{\sigma}}^T \mathbf{H}_{\sigma\sigma} \hat{\boldsymbol{\sigma}} - \delta \hat{\mathbf{s}}^T \mathbf{F} \right) dx - \delta \hat{\mathbf{s}}^T \mathbf{T} \Big|_{x=\bar{l}} = 0 \quad (3.23)$$

where, in addition to the definitions provided in (3.11), we set:

$$\begin{aligned} \mathbf{G}_{s\sigma} = \mathbf{G}_{\sigma s}^T &= \int_A \mathbf{R}_s^T \mathbf{E}_1 \mathbf{R}_{\sigma} dy & \mathbf{H}_{s'\sigma} = \mathbf{H}_{\sigma s'}^T &= \int_A \mathbf{R}_s'^T \mathbf{E}_2 \mathbf{R}_{\sigma} dy \\ \mathbf{H}_{\sigma\sigma} &= \int_A \mathbf{R}_{\sigma}^T \mathbf{D}^{-1} \mathbf{R}_{\sigma} dy \end{aligned} \quad (3.24)$$

Equation (3.23) represents the weak form of the 1D beam model. To obtain the corresponding boundary value problem, we integrate by parts the first term of (3.23):

$$\int_l \delta \hat{\mathbf{s}}'^T \mathbf{G}_{s\sigma} \hat{\boldsymbol{\sigma}} dx = \delta \hat{\mathbf{s}}^T \mathbf{G}_{s\sigma} \hat{\boldsymbol{\sigma}} \Big|_{x=0}^{x=\bar{l}} - \int_l \delta \hat{\mathbf{s}}^T \mathbf{G}_{s\sigma} \hat{\boldsymbol{\sigma}}' dx \quad (3.25)$$

Substituting Equation (3.25) in (3.23), recalling that $\delta \hat{\mathbf{s}} = \mathbf{0}$ on A_0 and collecting variables in a vector we obtain:

$$\int_l [\delta \hat{\mathbf{s}}; \delta \hat{\boldsymbol{\sigma}}]^T \left(\mathbf{G} \begin{Bmatrix} \hat{\mathbf{s}}' \\ \hat{\boldsymbol{\sigma}}' \end{Bmatrix} + \mathbf{H}^{gg} \begin{Bmatrix} \hat{\mathbf{s}} \\ \hat{\boldsymbol{\sigma}} \end{Bmatrix} - \begin{Bmatrix} \mathbf{F} \\ \mathbf{0} \end{Bmatrix} \right) dx + \delta \hat{\mathbf{s}}^T (\mathbf{G}_{s\sigma} \hat{\boldsymbol{\sigma}} - \mathbf{T}) \Big|_{x=\bar{l}} = 0 \quad (3.26)$$

in which

$$\mathbf{G} = \begin{bmatrix} \mathbf{0} & -\mathbf{G}_{s\sigma} \\ \mathbf{G}_{\sigma s} & \mathbf{0} \end{bmatrix} \quad \mathbf{H}^{gg} = \begin{bmatrix} \mathbf{0} & \mathbf{H}_{s'\sigma} \\ \mathbf{H}_{\sigma s'} & -\mathbf{H}_{\sigma\sigma} \end{bmatrix} \quad (3.27)$$

Requiring to satisfy Equation (3.26) for all the possible variations, and imposing the *essential* boundary condition $\hat{\mathbf{s}}$ we finally obtain:

$$\begin{cases} \mathbf{G} \begin{Bmatrix} \hat{\mathbf{s}}' \\ \hat{\boldsymbol{\sigma}}' \end{Bmatrix} + \mathbf{H}^{gg} \begin{Bmatrix} \hat{\mathbf{s}} \\ \hat{\boldsymbol{\sigma}} \end{Bmatrix} = \begin{Bmatrix} \mathbf{F} \\ \mathbf{0} \end{Bmatrix} & \text{in } l \\ \mathbf{G}_{s\sigma} \hat{\boldsymbol{\sigma}} = \mathbf{T} & \text{at } x = \bar{l} \\ \hat{\mathbf{s}} = \mathbf{0} & \text{at } x = 0 \end{cases} \quad (3.28)$$

We remark that boundary value problem (3.28) is not necessarily well-posed. This depends on how the profile vectors have been chosen for all the involved fields. However, well-posedness of (3.28) is guaranteed if the approximated fields are selected according with the approximation theory of saddle-point problem (2.11) (see Alessandrini et al. (1999)).

3.4.1.2 div-div approach

Using the notation introduced in Section 3.1 in Equation (2.13), the HR div-div functional stationarity becomes:

$$\begin{aligned} \delta J_{HR}^{dd} = & - \int_{\Omega} \delta \hat{\mathbf{s}}^T \mathbf{R}_s^T \left[\left(\frac{d}{dx} \mathbf{E}_1 + \frac{d}{dy} \mathbf{E}_2 \right) \mathbf{R}_{\sigma} \hat{\boldsymbol{\sigma}} \right] d\Omega - \int_{\Omega} \left[\left(\frac{d}{dx} \mathbf{E}_1 + \frac{d}{dy} \mathbf{E}_2 \right) \mathbf{R}_{\sigma} \delta \hat{\boldsymbol{\sigma}} \right]^T \mathbf{R}_s \hat{\mathbf{s}} d\Omega \\ & - \int_{\Omega} \delta \hat{\boldsymbol{\sigma}}^T \mathbf{R}_{\sigma}^T \mathbf{D}^{-1} \mathbf{R}_{\sigma} \hat{\boldsymbol{\sigma}} d\Omega - \int_{\Omega} \delta \hat{\mathbf{s}}^T \mathbf{R}_s^T \mathbf{f} d\Omega = 0 \end{aligned} \quad (3.29)$$

Expanding Equation (3.29), the weak formulation becomes:

$$\begin{aligned} \delta J_{HR}^{dd} = & - \int_{\Omega} \left(\delta \hat{\mathbf{s}}^T \mathbf{R}_s^T \mathbf{E}_1 \mathbf{R}_{\sigma} \hat{\boldsymbol{\sigma}}' + \delta \hat{\mathbf{s}}^T \mathbf{R}_s^T \mathbf{E}_2 \mathbf{R}_{\sigma} \hat{\boldsymbol{\sigma}} \right) d\Omega - \int_{\Omega} \left(\delta \hat{\boldsymbol{\sigma}}'^T \mathbf{R}_{\sigma}^T \mathbf{E}_1^T \mathbf{R}_s \hat{\mathbf{s}} + \delta \hat{\boldsymbol{\sigma}}'^T \mathbf{R}_{\sigma}^T \mathbf{E}_2^T \mathbf{R}_s \hat{\mathbf{s}} \right) d\Omega \\ & - \int_{\Omega} \left(\delta \hat{\boldsymbol{\sigma}}^T \mathbf{R}_{\sigma}^T \mathbf{D}^{-1} \mathbf{R}_{\sigma} \hat{\boldsymbol{\sigma}} + \delta \hat{\mathbf{s}}^T \mathbf{R}_s^T \mathbf{f} \right) d\Omega = 0 \end{aligned} \quad (3.30)$$

By using Fubini-Tonelli theorem, Equation (3.30) becomes:

$$\delta J_{HR}^{dd} = \int_l \left(-\delta \hat{\mathbf{s}}^T \mathbf{G}_{ss} \hat{\boldsymbol{\sigma}}' - \delta \hat{\mathbf{s}}^T \mathbf{H}_{s\sigma'} \hat{\boldsymbol{\sigma}} - \delta \hat{\boldsymbol{\sigma}}'^T \mathbf{G}_{\sigma s} \hat{\mathbf{s}} - \delta \hat{\boldsymbol{\sigma}}^T \mathbf{H}_{\sigma' s} \hat{\mathbf{s}} - \delta \hat{\boldsymbol{\sigma}}^T \mathbf{H}_{\sigma\sigma} \hat{\boldsymbol{\sigma}} - \delta \hat{\mathbf{s}}^T \mathbf{F} \right) dx = 0 \quad (3.31)$$

where

$$\mathbf{H}_{\sigma' s} = \int_A \mathbf{R}_{\sigma}'^T \mathbf{E}_2 \mathbf{R}_s dy$$

while the other matrices are defined as (3.24).

Equation (3.31) represents the weak form of the 1D beam model. To obtain the corresponding boundary value problem, we integrate by parts the third term of (3.31):

$$- \int_l \delta \hat{\boldsymbol{\sigma}}'^T \mathbf{G}_{\sigma s} \hat{\mathbf{s}} dx = - \delta \hat{\boldsymbol{\sigma}}^T \mathbf{G}_{\sigma s} \hat{\mathbf{s}} \Big|_{x=0}^{x=\bar{l}} + \int_l \delta \hat{\boldsymbol{\sigma}}^T \mathbf{G}_{\sigma s} \hat{\mathbf{s}}' dx \quad (3.32)$$

Substituting Equation (3.32) in Equation (3.31), recalling that $\mathbf{G}_{s\sigma} \delta \hat{\boldsymbol{\sigma}} = \mathbf{0}$ at $x = \bar{l}$, and collecting the unknowns in a vector we obtain:

$$\int_l [\delta \hat{\mathbf{s}}; \delta \hat{\boldsymbol{\sigma}}]^T \left(\mathbf{G} \begin{Bmatrix} \hat{\mathbf{s}}' \\ \hat{\boldsymbol{\sigma}}' \end{Bmatrix} + \mathbf{H}^{dd} \begin{Bmatrix} \hat{\mathbf{s}} \\ \hat{\boldsymbol{\sigma}} \end{Bmatrix} - \begin{Bmatrix} \mathbf{F} \\ \mathbf{0} \end{Bmatrix} \right) dx + \delta \hat{\boldsymbol{\sigma}}^T \mathbf{G}_{\sigma s} \hat{\mathbf{s}} \Big|_{x=0} = 0 \quad (3.33)$$

where \mathbf{G} is defined as in (3.27) and \mathbf{H}^{dd} is defined as:

$$\mathbf{H}^{dd} = \begin{bmatrix} \mathbf{0} & -\mathbf{H}_{s\sigma'} \\ -\mathbf{H}_{\sigma' s} & -\mathbf{H}_{\sigma\sigma} \end{bmatrix} \quad (3.34)$$

Requiring to satisfy Equation (3.33) for all the possible variations, and imposing the *essential* boundary condition (3.7), we finally obtain:

$$\begin{cases} \mathbf{G} \begin{Bmatrix} \hat{\mathbf{s}}' \\ \hat{\boldsymbol{\sigma}}' \end{Bmatrix} + \mathbf{H}^{dd} \begin{Bmatrix} \hat{\mathbf{s}} \\ \hat{\boldsymbol{\sigma}} \end{Bmatrix} = \begin{Bmatrix} \mathbf{F} \\ \mathbf{0} \end{Bmatrix} & \text{in } l \\ \hat{\boldsymbol{\sigma}}_x = \hat{\mathbf{t}}_x & \text{at } x = \bar{l} \\ \hat{\boldsymbol{\tau}} = \hat{\mathbf{t}}_\tau & \text{at } x = \bar{l} \\ \mathbf{G}_{\sigma s} \hat{\mathbf{s}} = \mathbf{0} & \text{at } x = 0 \end{cases} \quad (3.35)$$

We remark that boundary value problem (3.35) is not necessarily well-posed. This depends on how the profile vectors have been chosen for all the involved fields. However, well-posedness of (3.35) is guaranteed if the approximated fields are selected according with the approximation theory of saddle-point problem (2.13) (see Alessandrini et al. (1999)).

3.4.1.3 Conclusions on the derived beam models

From what we have developed in this section, we can make the following remarks.

- Starting from two different versions of the HR stationarity condition (i.e., grad-grad (2.11) and div-div (2.13)) and introducing hypothesis (2.20), we obtain two different classes of one-dimensional beam models. Both classes may be described by a boundary value problem of the following type:

$$\begin{cases} \mathbf{G} \begin{Bmatrix} \hat{\mathbf{s}}' \\ \hat{\boldsymbol{\sigma}}' \end{Bmatrix} + \mathbf{H} \begin{Bmatrix} \hat{\mathbf{s}} \\ \hat{\boldsymbol{\sigma}} \end{Bmatrix} = \begin{Bmatrix} \mathbf{F} \\ \mathbf{0} \end{Bmatrix} \\ + \text{suitable boundary conditions} \end{cases} \quad (3.36)$$

The difference between models based on the HR grad-grad formulation and the HR div-div one stands in the \mathbf{H} matrix. More precisely:

- $\mathbf{H} = \mathbf{H}^{gg}$ for the HR grad-grad formulation. In this case, derivatives are applied to the displacement fields through the symmetric gradient operator and the resulting models privilege the satisfaction of the compatibility relation (2.2a) rather than the equilibrium equation (2.2c).
- $\mathbf{H} = \mathbf{H}^{dd}$ for the HR div-div formulation. In this case, derivatives are applied to the stress fields through the divergence operator and the resulting models privilege the satisfaction of the equilibrium equation rather than the compatibility one.
- Boundary value problem (3.35) can be explicitly written as:

$$\begin{cases} -\mathbf{G}_{s\sigma} \hat{\boldsymbol{\sigma}}' - \mathbf{H}_{s\sigma'} \hat{\boldsymbol{\sigma}} = \mathbf{0} \\ \mathbf{G}_{\sigma s} \hat{\mathbf{s}}' - \mathbf{H}_{\sigma' s} \hat{\mathbf{s}} - \mathbf{H}_{\sigma\sigma} \hat{\boldsymbol{\sigma}} = \mathbf{F} \\ + \text{suitable boundary conditions} \end{cases}$$

We can compute $\hat{\boldsymbol{\sigma}}$ from the second equation and substitute it in the first one, obtaining a displacement-like formulation of the problem:

$$\begin{cases} \mathbf{A} \hat{\mathbf{s}}'' + \mathbf{B} \hat{\mathbf{s}}' + \mathbf{C} \hat{\mathbf{s}} = \mathbf{F} \\ + \text{suitable boundary conditions} \end{cases} \quad (3.37)$$

where

$$\mathbf{A} = -\mathbf{G}_{s\sigma} \mathbf{H}_{\sigma\sigma}^{-1} \mathbf{G}_{\sigma s} \quad \mathbf{B} = -\mathbf{G}_{s\sigma} \mathbf{H}_{\sigma\sigma}^{-1} \mathbf{H}_{\sigma' s} + \mathbf{H}_{s\sigma'} \mathbf{H}_{\sigma\sigma}^{-1} \mathbf{G}_{\sigma s} \quad \mathbf{C} = \mathbf{H}_{s\sigma'} \mathbf{H}_{\sigma\sigma}^{-1} \mathbf{H}_{\sigma' s}$$

Analogous considerations apply to problem (3.28).

3.4.2 Cross-section shape function definition

To design a multilayer beam model, we follow the two-step procedure described below.

1. In each layer, we choose suitable profiles for every field involved in the modeling. Of course, given a generic field, the simplest choice, which is the one we use in this paper, is to use the same profiles for every layer.
2. Across each interlayer, we impose the necessary continuity to ensure that the stresses belong to $H(\text{div}, \Omega)$.

As a consequence, given a generic field γ , it is possible to define its profile vector \mathbf{r}_γ , which is characterized by:

- The highest polynomial degree, with respect to y , used in a generic layer. This number is denoted by $\deg(\mathbf{r}_\gamma)$ in what follows.
- The regularity across each interlayer: in the following, C^{-1} stands for no continuity requirement, C^0 for standard continuity requirement.

Since a main aim of this paper is to develop a model with an accurate stress description, a natural choice is to assume $\deg(\mathbf{r}_\tau) = 2$, as in Jourawsky theory. To ensure well-posedness of the resulting model, we thus select the involved fields according to Table 3.4, where we also show the number of layer and global DOFs. Furthermore, we notice that we have to impose $\sigma_y = \tau = 0$ at the top and bottom of the beam.

	$\deg(\mathbf{r}_\gamma)$	inter-layer continuity	layer DOF	global DOF
\mathbf{r}_u	1	C^{-1}	2	2n
\mathbf{r}_v	2	C^{-1}	3	3n
\mathbf{r}_{σ_x}	1	C^{-1}	2	2n
\mathbf{r}_{σ_y}	3	C^0	4	3n-1
\mathbf{r}_τ	2	C^0	3	2n-1

Table 3.4: Polynomial degrees of the profiles vectors, continuity properties and number of DOFs for a multilayer beam.

Remark 3.4.1. *More generally, to design a well-posed beam model one could choose*

$$\begin{aligned} \deg(\mathbf{r}_{\sigma_x}) &= \deg(\mathbf{r}_u) = \deg(\mathbf{r}_\tau) - 1 \\ \deg(\mathbf{r}_\tau) &= \deg(\mathbf{r}_v) = \deg(\mathbf{r}_{\sigma_y}) - 1 \end{aligned} \tag{3.38}$$

together with the $H(\text{div})$ regularity for the stress field.

3.4.3 Beam-model examples

In this section we give two examples of beam models developed using the strategies of Section 3.4.1.2. More precisely, starting from the HR div-div approach (Equation (3.35)), we derive:

1. a single layer beam model in which we use a first order displacement field; by means of this example we will show that the approach under discussion is able to reproduce the classical models;
2. a multilayer beam model, in which we consider also higher order kinematic and stress fields; by means of this example we will illustrate how the approach could produce a refined model with a reasonable solution.

3.4.3.1 Single layer beam

Considering a homogeneous beam, we assume a first-order kinematic (as in Timoshenko model) and the usual cross-section stress distributions (obtained from the Jourawsky theory). In other words we make the following hypotheses:

$$\begin{array}{llll}
 u = u_0(x) + yu_1(x) & \text{i.e.} & \mathbf{r}_u = \begin{Bmatrix} 1 \\ y \end{Bmatrix} & \hat{\mathbf{u}} = \begin{Bmatrix} u_0 \\ u_1 \end{Bmatrix} \\
 v = v(x) & \text{i.e.} & \mathbf{r}_v = \{1\} & \hat{\mathbf{v}} = \{v\} \\
 \sigma_{xx} = \sigma_{x0}(x) + y\sigma_{x1}(x) & \text{i.e.} & \mathbf{r}_{\sigma_x} = \begin{Bmatrix} 1 \\ y \end{Bmatrix} & \hat{\boldsymbol{\sigma}}_x = \begin{Bmatrix} \sigma_{x0} \\ \sigma_{x1} \end{Bmatrix} \\
 \sigma_{yy} = 0 & \text{i.e.} & \mathbf{r}_{\sigma_y} = \{0\} & \hat{\boldsymbol{\sigma}}_y = \{0\} \\
 \tau = (1 - 4y^2/h^2) \tau(x) & \text{i.e.} & \mathbf{r}_\tau = \{1 - 4y^2/h^2\} & \hat{\boldsymbol{\tau}} = \{\tau\}
 \end{array}$$

The matrices \mathbf{G} and \mathbf{H}^{dd} defined in (3.27) and (3.34), and entering into the beam model (3.35), are explicitly given by:

$$\mathbf{G} = \begin{bmatrix} 0 & 0 & 0 & -h & 0 & 0 \\ 0 & 0 & 0 & 0 & -\frac{h^3}{12} & 0 \\ 0 & 0 & 0 & 0 & 0 & -\frac{2}{3}h \\ h & 0 & 0 & 0 & 0 & 0 \\ 0 & \frac{h^3}{12} & 0 & 0 & 0 & 0 \\ 0 & 0 & \frac{2}{3}h & 0 & 0 & 0 \end{bmatrix}; \quad \mathbf{H}^{dd} = \begin{bmatrix} 0 & 0 & 0 & 0 & 0 & 0 \\ 0 & 0 & 0 & 0 & 0 & \frac{2}{3}h \\ 0 & 0 & 0 & 0 & 0 & 0 \\ 0 & 0 & 0 & -\frac{h}{E} & 0 & 0 \\ 0 & 0 & 0 & 0 & -\frac{h^3}{12E} & 0 \\ 0 & \frac{2}{3}h & 0 & 0 & 0 & -\frac{8}{15}h \frac{2(1+\nu)}{E} \end{bmatrix} \quad (3.39)$$

Since problem (3.35) is governed by an ODE system with constant coefficients, the homogeneous solution can be analytically computed. For example, choosing

$$h = 1 \text{ [mm]} \quad l = 10 \text{ [mm]} \quad E = 10^5 \text{ [MPa]} \quad \nu = 0.25 \text{ [-]}$$

the homogeneous solution is given by

$$\begin{aligned}
 u_0 &= 5.00 \cdot 10^{-6} C_4 x + C_1 \\
 u_1 &= 4.00 \cdot 10^{-6} C_6 x^2 + 5.00 \cdot 10^{-6} C_5 x + C_2 \\
 v &= -(1.33 \cdot 10^{-5} C_6 x^3 + 5.00 \cdot 10^{-6} C_5 x^2 + 5.00 \cdot 10^{-1} C_2 x + C_3) + 10^{-5} C_6 x \\
 \sigma_{x0} &= C_4 \\
 \sigma_{x1} &= 4.00 C_6 x + C_5 \\
 \tau &= C_6
 \end{aligned} \quad (3.40)$$

in which C_i are arbitrary constants. The six constants of (3.40) may be determined by imposing the boundary conditions specified in (3.35). Indeed, for the beam model under consideration, the boundary conditions in (3.35) lead to a set of six linearly independent equations, since the matrix \mathbf{G}_{σ_s} (cf. (3.24) and (3.27)) is invertible.

We remark that the solution (3.40) is compatible with the one obtained by the Timoshenko beam model. However, we underline that the stress distributions along the beam axis are obtained directly from the model solution, and not by means of the displacement derivatives, as happens in classical formulations.

We also notice that, reducing the model to the displacement formulation (cf. (3.37)), we obtain the following ODE system:

$$\begin{cases} hEu_0'' = 0 \\ \frac{h^3}{12}Eu_1'' - \frac{5}{62}\frac{Eh}{(1+\nu)}(v' + u_1) = 0 \\ \frac{5}{62}\frac{Eh}{(1+\nu)}(v'' + u_1') = 0 \\ + \text{suitable boundary conditions} \end{cases} \quad (3.41)$$

Therefore, not surprisingly, we again recover the classical Timoshenko equations, where, however, the exact shear correction factor (5/6) automatically appears. The same result holds true in the framework of variational plate modelling proposed by Alessandrini et al. (1999).

3.4.3.2 Multilayer beam

We now consider the multilayer beam model described in Section 3.3.2.3. Considering the div-div beam model, the total number of cross-section variables is 34. We notice that the boundary value problem (3.35) is uniquely solvable also in this case. However, we now have $\text{rank}(\mathbf{G}) = 22$, which means that problem (3.35) is actually a differential-algebraic boundary value problem. Thus, 22 variables are solutions of a differential problem, while the remaining 12 unknowns are algebraically determined by the former ones. We also remark that the boundary conditions in (3.35) actually lead to 22 independent constraints, since $\text{rank}(\mathbf{G}_{\sigma s}) = 11$.

We now give the solution of the generalized eigenvalue problem $\det(\lambda\mathbf{G} + \mathbf{H}^{dd}) = 0$, which enters in the construction of the homogeneous solution of (3.35).

$$\lambda = \left\{ \begin{array}{c} \sim 0 \\ \pm 11.430 \pm 3.870i \\ \pm 7.481 \pm 2.585i \\ \pm 4.023 \pm 2.520i \\ \pm 15.520 \pm 6.021i \end{array} \right\} \begin{array}{l} [6] \\ [4] \\ [4] \\ [4] \\ [4] \end{array}$$

where in square brackets we show the eigenvalue multiplicities, and we used the symbol ~ 0 to denote eigenvalues which vanish up to the machine precision.

It is possible to evaluate also the homogeneous solution but, given the problem complexity, it is huge and we will not report it. Nevertheless it is possible to discuss its structure and made some important remarks.

- The zero eigenvalues lead to polynomial terms analogous to the Timoshenko homogeneous solution described in Section 3.4.3.1.
- The complex conjugate eigenvalues ($a \pm ib$) lead to functions like $C_i e^{ax} \sin(bx + C_j)$, which describe local effects near the boundaries, as it happens in several other beam models (see Ladeveze and Simmonds, 1998; Allix and Dupleix-Couderc, 2010).

3.4.4 FE derivation

In this section we develop the FE corresponding to the multilayer beam model introduced in Section 3.4.3.2. This is equivalent to introduce a dimension reduction also along the beam axis, leading, therefore, to a purely algebraic system.

3.4.4.1 Weak problem formulation

We now make explicit the weak formulation we will use as a starting point for the FE discretization. To this end, we first recall the beam model variational formulation (3.31). Then, we integrate by parts with respect to the x direction both the first and the third terms of Equation (3.31). We thus obtain:

Find $\hat{\mathbf{s}} \in \widetilde{W}$ and $\hat{\boldsymbol{\sigma}} \in \widetilde{S}$ such that for every $\delta\hat{\mathbf{s}} \in \widetilde{W}$ and for every $\delta\hat{\boldsymbol{\sigma}} \in \widetilde{S}$

$$\delta J_{HR} = \int_l \left(\delta\hat{\mathbf{s}}^T \mathbf{G}_{s\sigma} \hat{\boldsymbol{\sigma}} - \delta\hat{\mathbf{s}}^T \mathbf{H}_{s\sigma'} \hat{\boldsymbol{\sigma}} + \delta\hat{\boldsymbol{\sigma}}^T \mathbf{G}_{\sigma s} \hat{\mathbf{s}}' - \delta\hat{\boldsymbol{\sigma}}^T \mathbf{H}_{\sigma's} \hat{\mathbf{s}} - \delta\hat{\boldsymbol{\sigma}}^T \mathbf{H}_{\sigma\sigma} \hat{\boldsymbol{\sigma}} - \delta\hat{\mathbf{s}}^T \mathbf{F} \right) dx - \delta\hat{\mathbf{s}}^T \mathbf{T} \Big|_{x=\bar{l}} = 0 \quad (3.42)$$

where

$$\widetilde{W} := \{ \hat{\mathbf{s}} \in H^1(l) : \hat{\mathbf{s}}|_{x=0} = \mathbf{0} \}; \quad \widetilde{S} := L^2(l)$$

We may notice that all the derivatives with respect to x are applied to displacement variables, whereas derivatives with respect to y (incorporated into the \mathbf{H} matrices) are applied to cross-section stress vectors. The resulting variational formulation has the following features:

- The obtained weak formulation (3.42) is symmetric.
- y -derivatives applied to stresses and the essential conditions of S_t^{dd} (cf. Definition (2.15)) lead to a formulation which accurately solve the equilibrium equation in the y direction, i.e. in the cross-section.
- x derivatives applied to displacements and the essential condition in \widetilde{W} lead to a formulation which accurately solve the compatibility equation (2.2a) along the beam axis.

3.4.4.2 FE formulation

The FE discretization simply follows from the application of (2.21) into the variational formulation (3.42). We get:

$$\begin{aligned} \delta J_{HR} = & \int_l \left(\delta\tilde{\mathbf{s}}^T \mathbf{N}'^T_s \mathbf{G}_{s\sigma} \mathbf{N}_\sigma \tilde{\boldsymbol{\sigma}} - \delta\tilde{\mathbf{s}}^T \mathbf{N}_s^T \mathbf{H}_{s\sigma'} \mathbf{N}_\sigma \tilde{\boldsymbol{\sigma}} + \delta\tilde{\boldsymbol{\sigma}}^T \mathbf{N}_\sigma^T \mathbf{G}_{\sigma s} \mathbf{N}'_s \tilde{\mathbf{s}}' \right) dx + \\ & - \int_l \left(\delta\tilde{\boldsymbol{\sigma}}^T \mathbf{N}_\sigma^T \mathbf{H}_{\sigma's} \mathbf{N}_s \tilde{\mathbf{s}} + \delta\tilde{\boldsymbol{\sigma}}^T \mathbf{N}_\sigma^T \mathbf{H}_{\sigma\sigma} \mathbf{N}_\sigma \tilde{\boldsymbol{\sigma}} - \delta\tilde{\mathbf{s}}^T \mathbf{N}_s^T \mathbf{F} \right) dx - \delta\tilde{\mathbf{s}}^T \mathbf{N}_s^T \mathbf{T} \Big|_{x=\bar{l}} = 0 \end{aligned} \quad (3.43)$$

Collecting unknown coefficients in a vector and requiring to satisfy Equation (3.43) for all the possible virtual fields we obtain:

$$\begin{bmatrix} \mathbf{0} & \mathbf{K}_{s\sigma} \\ \mathbf{K}_{\sigma s} & \mathbf{K}_{\sigma\sigma} \end{bmatrix} \begin{Bmatrix} \tilde{\mathbf{s}} \\ \tilde{\boldsymbol{\sigma}} \end{Bmatrix} = \begin{Bmatrix} \tilde{\mathbf{F}} \\ \mathbf{0} \end{Bmatrix} \quad (3.44)$$

where the vector $\tilde{\mathbf{F}}$ is defined in Equation (3.20) and

$$\mathbf{K}_{s\sigma} = \mathbf{K}_{\sigma s}^T = \int_l (\mathbf{N}'^T_s \mathbf{G}_{s\sigma} \mathbf{N}_\sigma - \mathbf{N}_s^T \mathbf{H}_{s\sigma'} \mathbf{N}_\sigma) dx \quad \mathbf{K}_{\sigma\sigma} = - \int_l \mathbf{N}_\sigma^T \mathbf{H}_{\sigma\sigma} \mathbf{N}_\sigma dx$$

3.4.4.3 Axis shape function definition

In what follows we will focus, for all the involved variables, on the finite element spaces shown in Table 3.5, where we also recall the profile properties which has led to the multi-layered beam model. For the polynomial degrees and continuity requirements, we here use the same notation as in Section 3.4.3.2. Thus, for example, the field v is approximated by means of piecewise cubic polynomials, continuous along the axial direction.

	$\deg(\mathbf{r}_\gamma)$	y continuity	$\deg(\mathbf{N}_\gamma)$	x continuity
u	1	C^{-1}	2	C^0
v	2	C^{-1}	3	C^0
σ_x	1	C^{-1}	1	C^{-1}
σ_y	3	C^0	3	C^{-1}
τ	2	C^0	2	C^{-1}

Table 3.5: Degree and continuity properties of shape functions with respect to y and x directions.

We remark that this choice of the finite element shape functions assures the stability and convergence of the resulting discrete scheme. We also notice that stresses are discontinuous across elements along the x direction, so that it is possible to statically condensate them out at the element level, reducing the dimension of the global stiffness matrix and improving efficiency.

3.4.5 Numerical Examples

3.4.5.1 Multilayer homogeneous beam

We now consider the same three layer homogeneous beam introduced in Section 3.3.2.3 (total thickness $h = 1\text{mm}$). Together with the clamping condition in A_0 , we assume the beam to be loaded by null body load $\mathbf{f} = \mathbf{0}$ and, along A_l , by the quadratic shear stress distribution $\mathbf{t}|_{A_l} = [0, 3/2(1 - 4y^2)]^T [\text{MPa}]$.

3.4.5.1.1 Convergence In Table 3.6 we report the mean value of the transverse displacement along A_l , as obtained by employing the following different procedures, evaluated for a beam of length $\bar{l} = 10\text{mm}$:

1. the classical Euler-Bernoulli beam model;
2. the classical Timoshenko beam model;
3. the numerical model under investigation, in which the solution is computed using a mesh of 64 elements;
4. a 2D FE scheme of the structural analysis program ABAQUS, using a fine regular grid of 3500×350 elements.

In Table 3.7 we report the mean value of the transverse displacement along A_l , as obtained by employing the procedures so far mentioned and the parameters specified in the following, evaluated for a beam of length $\bar{l} = 30\text{mm}$:

1. for the numerical model under investigation, we use a mesh of 128 elements;
2. for the 2D FE scheme, we use a fine regular grid of 6000×400 elements.

Due to the large number of elements used, we consider the FE solutions as the reference solution, and we denote with v_{ex} their mean value along A_l .

In Tables 3.6 and 3.7 we also report the following relative error quantity:

$$e_{rel}^v := \frac{|v - v_{ex}|}{|v_{ex}|} \quad (3.45)$$

where v is the mean value along A_l computed by the various procedures. We remark that e_{rel}^v gives an indication of the model accuracy, even though it is not the usual error measure in terms of the natural norms.

Beam theory	$v(10)$ [mm · 10 ⁻²]	e_{rel}^v [· 10 ⁻³]
Euler-Bernoulli	4.000 000	6.192
Timoshenko	4.030 000	1.261
Three-layered mixed FE	4.026 460	0.382
2D solution	4.024 924	-

Table 3.6: Transverse displacements and relative errors of the free-edge of a cantilever ($\bar{l} = 10$ and $h = 1$) obtained by different beam theories.

Beam theory	$v(30)$ [mm]	e_{rel}^v [· 10 ⁻⁴]
Euler-Bernoulli	1.080 000	4.257
Timoshenko	1.080 900	4.072
Three-layered mixed FE	1.080 578	1.092
2D solution	1.080 460	-

Table 3.7: Transverse displacements and relative errors of the free-edge of a cantilever ($\bar{l} = 30$ and $h = 1$) obtained by different beam theories.

Table 3.6 shows the superior performance of the three-layered mixed FE with respect to the other considered 1D models. Table 3.7 confirms the results illustrated in Table 3.6, nevertheless we notice that the relative errors decrease of 1 order of magnitude. It can be shown that the 2D beam solution converges to the EB solution (see Ciarlet (1997), for instance) increasing the beam slenderness. The numerical results illustrated in Tables 3.6 and 3.7 agree with the theoretical results and indicate the asymptotic consistency of the proposed beam model.

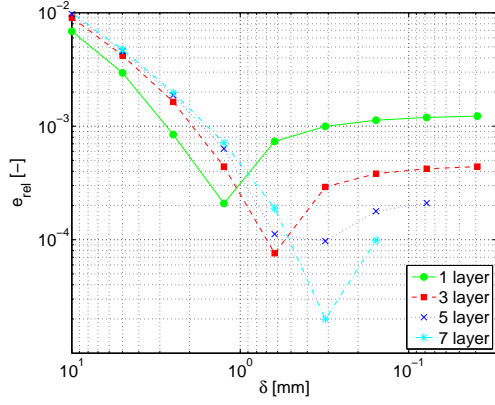
In Figure 3.2 we study the convergence of our numerical model. More precisely, we plot the relative quantity defined in Equation (3.45), evaluated considering i layers of thickness $h_i = 1/i$ ($i = 1, 3, 5, 7$), $\bar{l} = 10$, and different mesh sizes δ in the x direction. Figure 3.2(a) illustrates the convergence of the FE solution with respect to the 2D problem solution. Looking at Figure 3.2(a) we notice that:

- using even a few elements the quantity e_{rel}^v is under 1%;
- the error e_{rel}^v decreases as the number of layers increases;
- using highly-refined mesh, the relative error e_{rel}^v increases, even if it apparently converges to a constant close to 10^{-3} . This behaviour can be explained by recalling that a *modeling error* does necessarily arise. Indeed, the solution of the 2D elastic problem and the one of the multi-layered beam mixed model do differ from each others, for a fixed length and thickness of the beam.

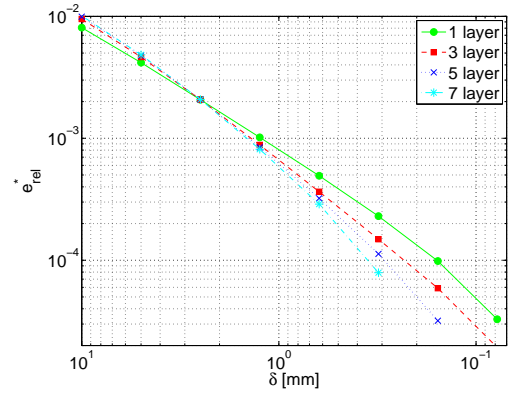
In Figure 3.2(b) we consider another relative quantity, namely e_{rel}^* . Such a quantity is similar that defined in (3.45), but here the reference solution is the one obtained by the FE analysis of the multi-layered model using the most refined mesh. The aim of this investigation is to provide informations about the convergence of the FE solution with respect to the one dimension (1D) model solution. We notice that:

- the sequences of errors e_{rel}^* are monotonically convergent to zero;
- fixing the number of layers, the log-log plots of errors suggest a convergence rate of the order of α , with $\alpha \approx 1$.

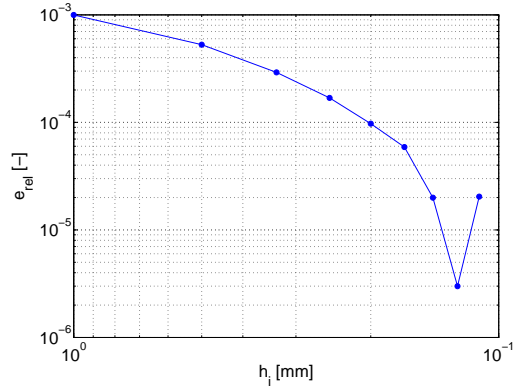
Finally, in Figure 3.2(c) we plot the relative error e_{rel}^v versus the number of layers (results obtained using a mesh of 32 elements). The aim of this investigation is to provide some informations



(a) Relative error e_{rel}^v , evaluated assuming $v_{ex} = 2D$ numerical solution.



(b) Relative error e_{rel}^* , evaluated assuming $v_{ex} = 1D$ numerical solution obtained using the most refined x -direction mesh.



(c) Relative error e_{rel}^v , plotted as a function of the layer thickness h_i , with mesh size $\delta = 0.3125$ mm.

Figure 3.2: Relative errors on free-edge, transverse displacement for different mesh sizes δ and different number of layers.

about the effects of 1D model refinement on FE solution accuracy. It is evident that the relative error decreases incrementing the number of layers even if the succession is not linear.

3.4.5.1.2 Boundary effects As already noticed in Section 3.3.2.3, the model under investigation is capable to capture some local effect near the clamped boundary; we here present some results focused on that issue. Even though this study is far from being exhaustive, it gives an indication of the model potentials. In what follows the computations are performed using a mesh of 64 elements. Preliminary numerical tests highlight that the local effects extinguish in an axis region of length similar to the cross-section thickness. As a consequence, to highlight the boundary effects we consider a beam analogous to the one introduced at the beginning of Section 3.4.5.1 in which we set $\bar{l} = 2.5\text{mm}$. The results are reported in Figures 3.3, 3.4 and 3.5.

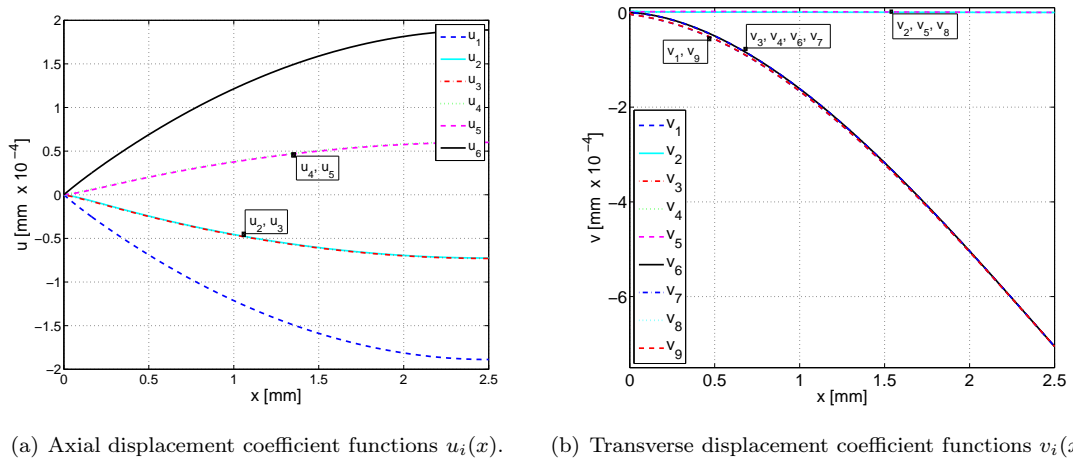


Figure 3.3: Axial and transverse displacement coefficient functions of a three-layer, homogeneous cantilever, clamped in $x = 0$, loaded at $x = 2.5$ by a quadratic shear distribution and modelled by means of 64 elements.

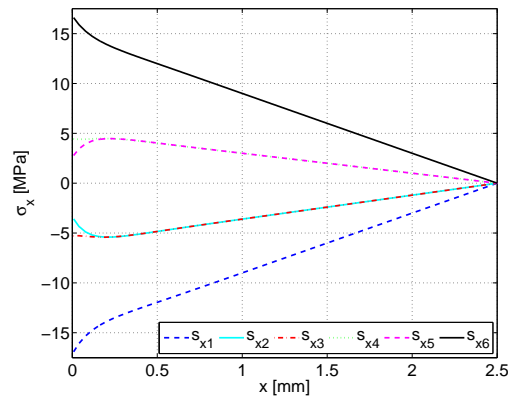


Figure 3.4: Axial stress coefficient functions $s_{xi}(x)$ of a three layer, homogeneous cantilever, clamped in $x = 0$, loaded at $x = 2.5$ by a quadratic shear distribution and modelled with 64 elements.

We can appreciate the following.

- Far from the boundary, it is possible to recognize the classical beam solution (constant shear stress $\tau(x)$, linear axial stress $\sigma_x(x)$, quadratic horizontal displacement $u(x)$ and cubic

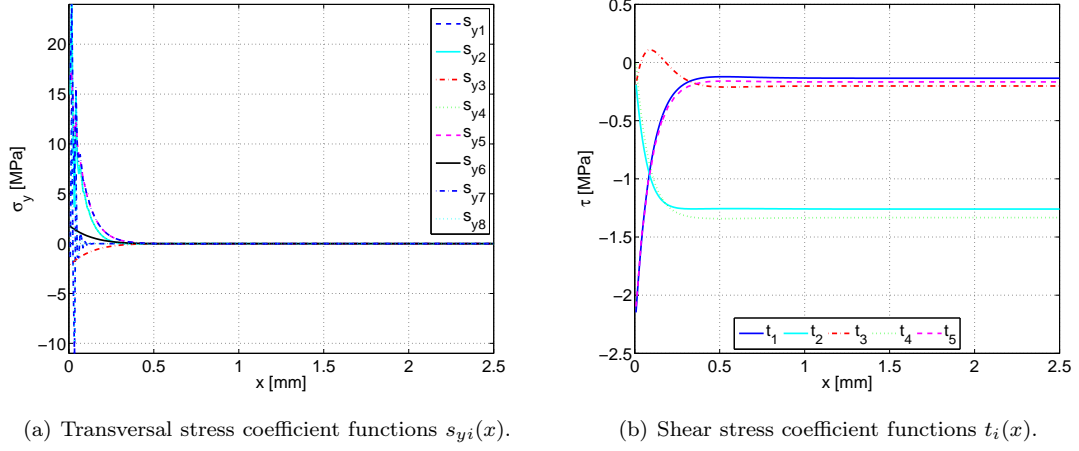


Figure 3.5: Transversal stress coefficient functions and shear coefficient functions of a three layer, homogeneous cantilever, clamped in $x = 0$, loaded at $x = 2.5$ by a quadratic shear distribution and modelled by means of 64 elements.

transverse displacement $v(x)$).

- As expected, the boundary effects decay as a damped harmonic functions.
- The local effects decay very rapidly, so that only the first oscillation is significant. This result is consistent with the other models capable to capture this kind of boundary effects.
- The section striction, described by the displacement quadratic terms v_2 , v_5 and v_8 , is negligible, as assumed in first-order theories.

As specified in Table 3.5, in the numerical model under discussion we do not *a-priori* impose displacement continuity across layers. In Figure 3.6 we plot the jump of the displacement filed across the inter-layer surfaces S_1 and S_2 . Figure 3.6(b) highlights that the transverse displacement

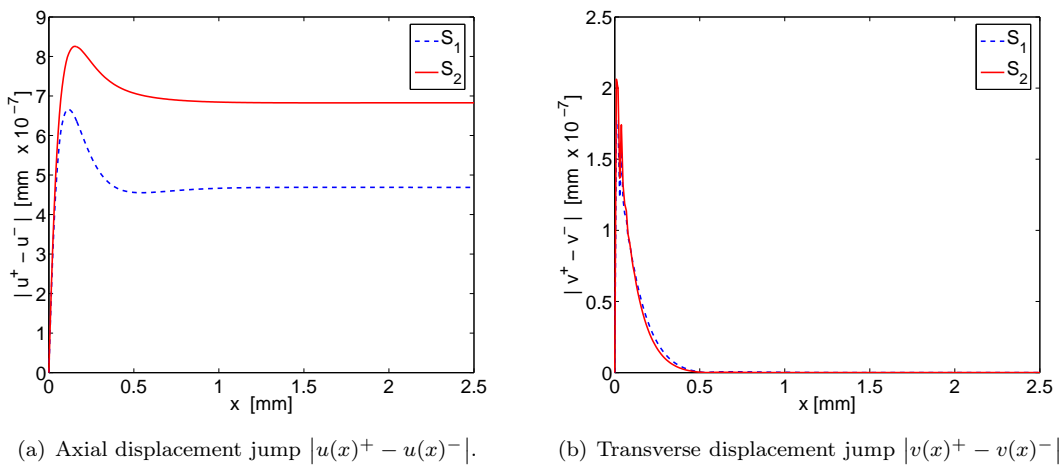


Figure 3.6: Relative axial and transverse displacements (i.e. compatibility errors) evaluated on interlayer surfaces $S_1 : y = -1/5$ and $S_2 : y = 1/6$.

jump rapidly decay far from the clamped boundary. On the other hand, from Figure 3.6(a) we

see that, far from the clamped boundary, the axial displacement jump $|u(x)^+ - u(x)^-|$ tends to a value different from zero (of the order of 10^{-7} mm). However, we notice that the displacement field is much greater, since it is of the order of 10^{-4} mm.

3.4.5.2 Multilayer non-homogeneous symmetric section

We consider a cantilever composed by three layers (total thickness $h = 1$ mm), clamped in A_0 , for which $\bar{l} = 5$ mm and $\mathbf{t}|_{A_l} = [0, 3/2(1 - 4y^2)]^T$ [MPa]; geometry and mechanical properties are specified in the following vectors:

$$\mathbf{h} = \begin{Bmatrix} 0.25 \\ 0.50 \\ 0.25 \end{Bmatrix} [\text{mm}] \quad \mathbf{E} = \begin{Bmatrix} 1 \cdot 10^5 \\ 1 \cdot 10^3 \\ 1 \cdot 10^5 \end{Bmatrix} [\text{MPa}] \quad \boldsymbol{\nu} = \begin{Bmatrix} 0.25 \\ 0.25 \\ 0.25 \end{Bmatrix} [-]$$

We evaluate the solution of the 1D model assuming a mesh size $\delta = 0.15625$ mm (32 elements) and the 2D solution using ABAQUS software and considering a mesh of 200×1000 square elements. For both the models we evaluate the stress distributions at different sections: $x = 2.5$, $x = 0.5$ and $x = 0.125$, as reported in Figures 3.7, 3.8 and 3.9 respectively.

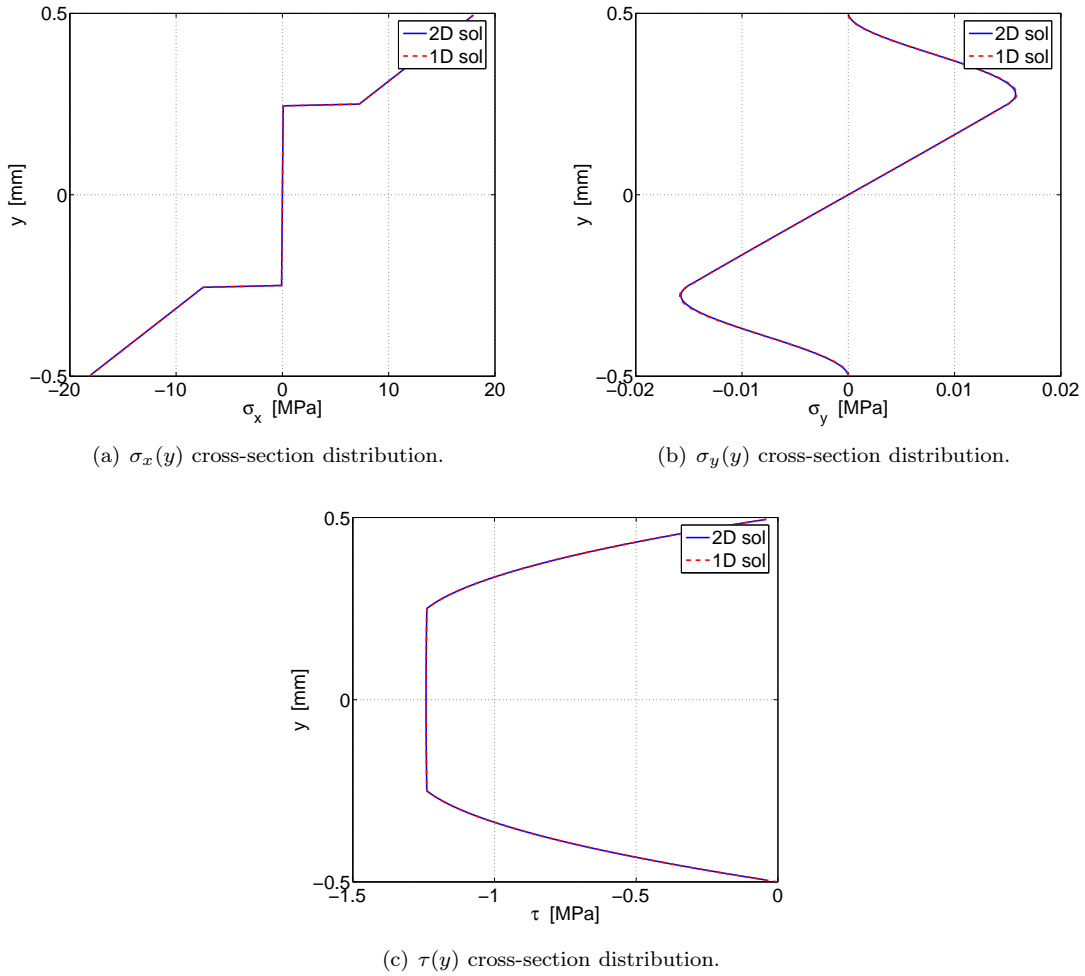


Figure 3.7: Cross-section stress-distributions evaluated at $x = 2.5$, far from the clamped boundary. 1D and 2D solutions for the symmetric section.

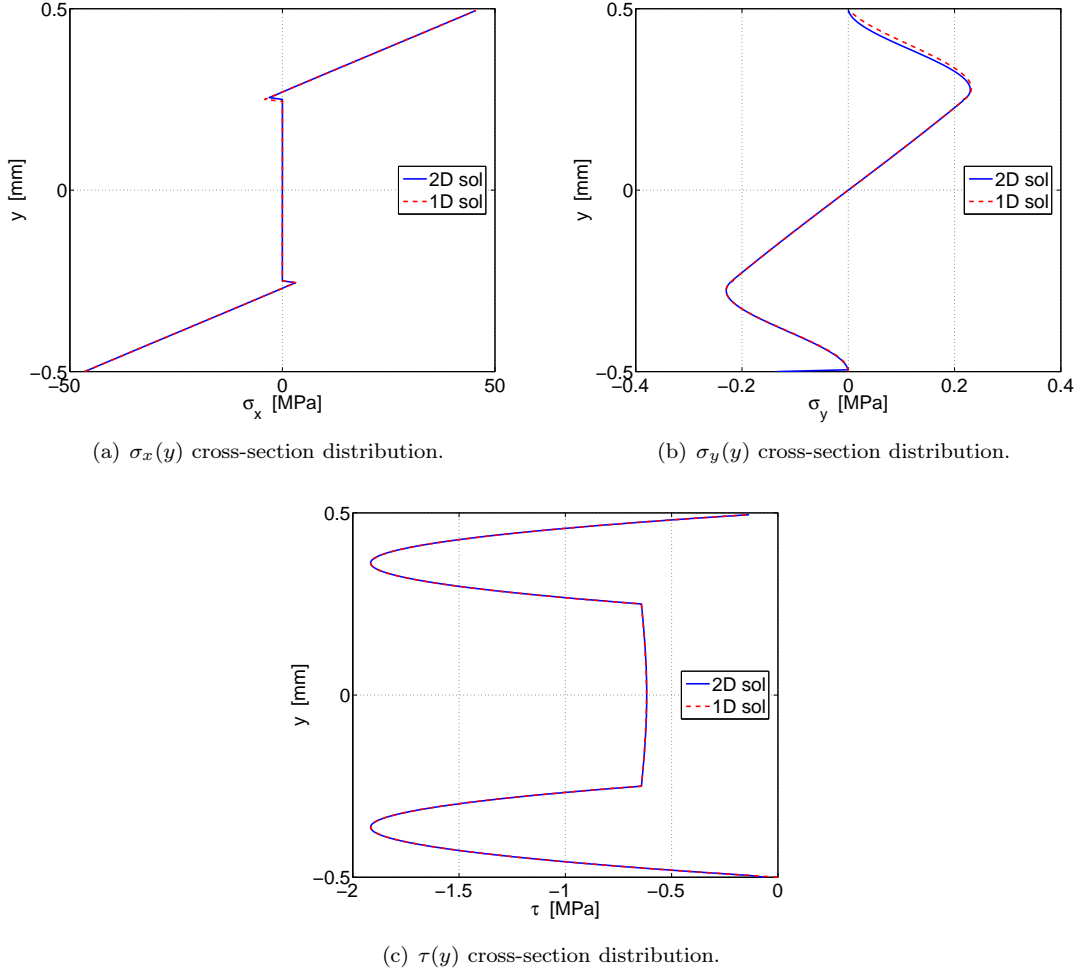


Figure 3.8: Cross-section stress-distributions evaluated at $x = 0.5$, close to the clamped boundary. 1D and 2D solutions for the symmetric section.

The capability of the numerical model to reproduce a very accurate stress distribution, far from the clamped boundary, is clearly seen from Figures 3.7. A similar feature is also maintained close the clamped boundary (see Figures 3.8 and 3.9), even though some error progressively arises as we approach $x = 0$. In particular, the axial stress σ_x and the shear stress τ are very accurately described, whereas the σ_y approximation exhibit a worse performance (maybe also because some kind of instability arises, cf. Figure 3.5(a)).

3.4.5.3 Multilayer non-homogeneous non-symmetric section

We consider a cantilever composed by four layers, clamped in A_0 , and for which $\bar{l} = 5\text{mm}$. The applied traction is: $\mathbf{t}|_{A_l} = [0, 3/2(1 - 4y^2)]^T$ [MPa]. The geometric and mechanical properties of the section are:

$$\mathbf{h} = \begin{Bmatrix} 0.25 \\ 0.25 \\ 0.25 \\ 0.25 \end{Bmatrix} [\text{mm}] \quad \mathbf{E} = \begin{Bmatrix} 1 \cdot 10^5 \\ 1 \cdot 10^3 \\ 1 \cdot 10^5 \\ 1 \cdot 10^3 \end{Bmatrix} [\text{MPa}] \quad \boldsymbol{\nu} = \begin{Bmatrix} 0.25 \\ 0.25 \\ 0.25 \\ 0.25 \end{Bmatrix} [-]$$

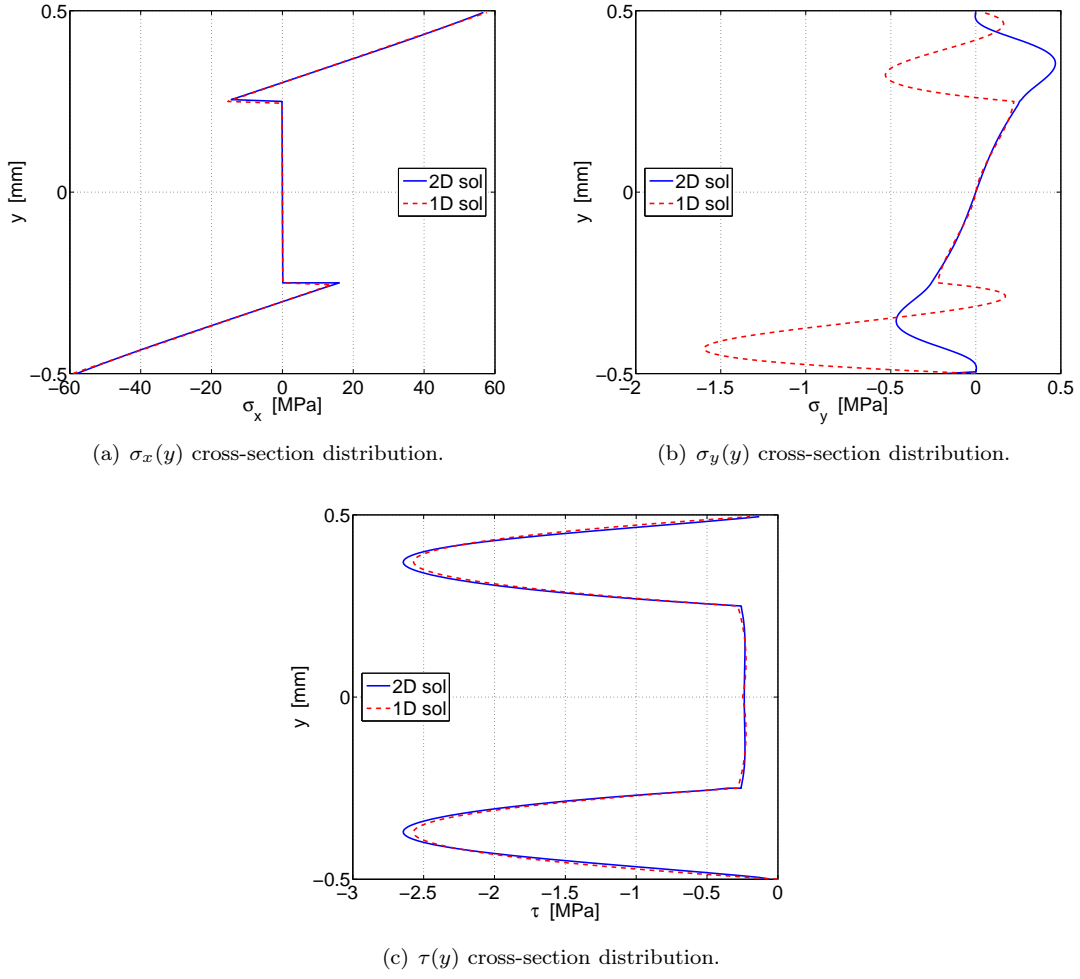


Figure 3.9: Cross-section stress-distributions evaluated at $x = 0.125$, very close to the clamped boundary. 1D and 2D solutions for the symmetric section.

We evaluate the 1D and 2D solutions using the same meshes as for the symmetric case of Section 3.4.5.2. The computed stress distributions at $x = 2.5$ is reported in Figures 3.10.

As in the symmetric case, there is no significant difference between the 1D and the 2D cross-section stress distributions. We only notice a small deviation (below 1%) in the plot of the σ_y .

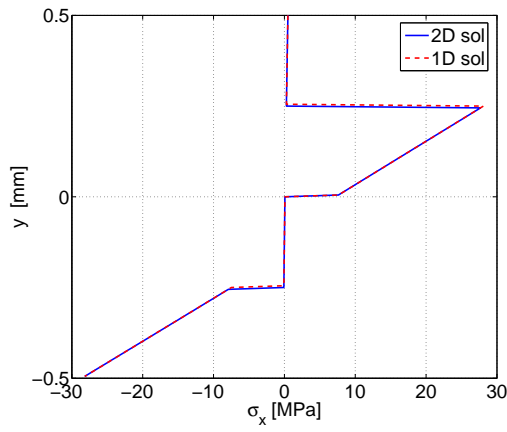
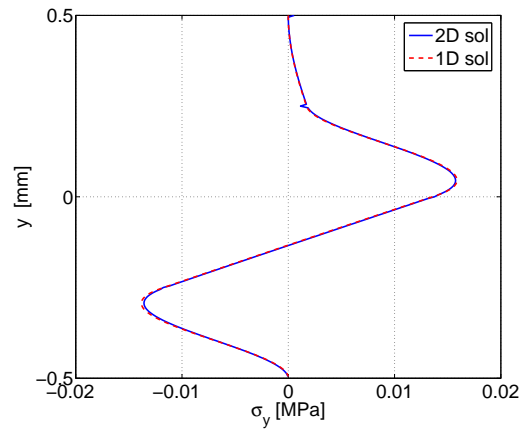
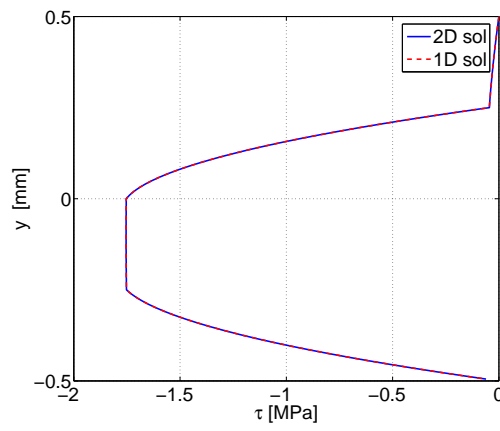
(a) $\sigma_x(y)$ cross-section distribution.(b) $\sigma_y(y)$ cross-section distribution.(c) $\tau(y)$ cross-section distribution.

Figure 3.10: Cross-section stress-distributions evaluated at $x = 2.5$, 1D and 2D solutions for the un-symmetric section.

3.5 Comparison of computational time

In this section we discuss and compare rigorously the numerical performance of the so far introduced beam FE. In particular we consider:

- TPE based beam FE introduced in Section 3.3.1 together with the kinematic specified in Table 3.2, denoted in the following as TPE_{cq} ,
- TPE based beam FE introduced in Section 3.3.1 together with a kinematic that uses cross-section shape functions defined as continuous piecewise polynomial with degrees specified in Table 3.4, denoted in the following as TPE_{lq} ,
- HR based beam FE introduced in Section 3.4.3.2, denoted in the following as HR .

In order to discuss the numerical performance of the proposed method, we consider an homogeneous beam identical to the one introduced in Section 3.4.5.1, modelled as if it is formed of 5 equal layers. Moreover, along the beam axis, we consider a regular mesh of equal elements.

In order to evaluate correctly the computation time, we implement the so far introduced models using the same program (MAPLE) and sequences of operations as similar as possible.

The global computational time t_{comp} take into account the time necessary to assemble the global matrix and solve the global linear system whereas pre-processing and post-processing are not considered.

We highlight that the axis shape functions are the same for all the considered models whereas only the cross-section shape functions change between the considered FE. Moreover we specify that, in all the considered FE, we condense out at element level all DOFs which support is a single element. As a consequence in all the considered FE we compute only the nodal displacements.

The displacement error e_{rel}^v is evaluated as in Equation (3.45) whereas the shear error e_{rel}^τ is defined as follows:

$$e_{rel}^\tau := \frac{|\tau(5,0) - \tau_{ref}(5,0)|}{|\tau_{ref}(5,0)|} \quad (3.46)$$

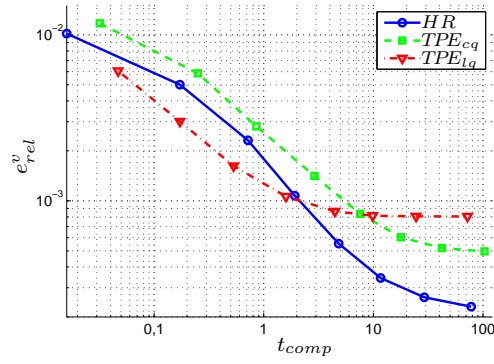
where $\tau_{ref}(5,0) = 3/2$, that corresponds to the value obtained from the analytical solution (see Timoshenko and Goodier, 1951).

Figures 3.11(a) and 3.11(b) plot respectively the displacement error e_{rel}^v and the shear error e_{rel}^τ as functions of the computational time t_{comp} . In both figures, data refer to regular meshes of 1, 2, 4, 8, 16, 32, 64, 128 elements that correspond to an increasing computational time.

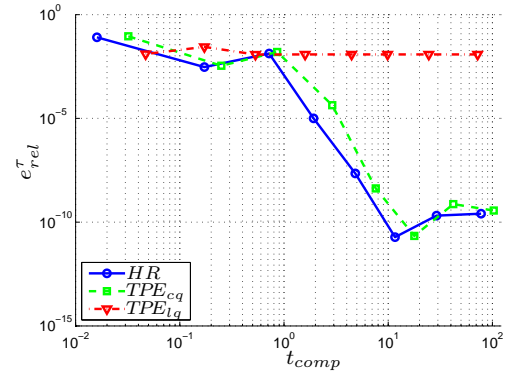
In Figure 3.11(a) we highlight that the curve relative to the three models display similar behaviours. Using few elements, TPE_{lq} is most performing FE whereas, using refined meshes, the HR is the most performing FE.

In Figure 3.11(b), TPE_{lq} has a bad behaviour since the increase of mesh refinement produce an increment of the computational time t_{comp} but negligible decrease of the shear error e_{rel}^τ . On the other hand, HR and TPE_{cq} evidence significant decreases of error estimation. In particular, HR shows the best performance with respect to shear error evaluation. Similar results are obtained also considering different numbers of layers, nevertheless we do not report them.

As a final remark, we can state that the HR FE seems to be the numerical model with the best benefit-cost ratio, at least considering as unique cost the computational time and as a benefit the decrease of error.



(a) displacement error e_{rel}^v versus computational time t_{comp}



(b) shear error e_{rel}^τ versus computational time t_{comp}

Figure 3.11: Displacement and shear errors versus the computational time, results evaluated for a 5 layer homogeneous beam.

Chapter 4

3D Beam–model

In this chapter we are going to consider a 3D elastic problem, i.e. with respect to the notation introduced in Chapter 2 we assume $n = 3$. As a consequence, the cross-section coordinates are defined as $\mathbf{y} = [y, z]^T$. Figure 4.1 represents the domain, the adopted Cartesian coordinate system, the initial and the final cross sections A_0 and A_l respectively, and the lateral surface L for the case we are considering.

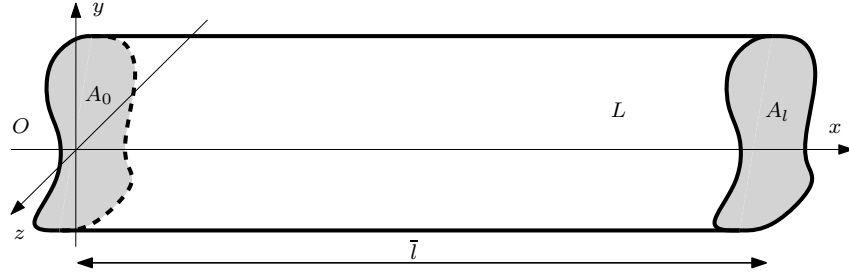


Figure 4.1: 3D beam geometry, Cartesian coordinate system, dimensions, and adopted notations.

Section 4.1 provides a brief literature review on existing 3D solution. Section 4.2 formulates the 3D, HR based beam model and discusses the analytical solution of some beam model examples. Section 4.3 formulates the corresponding FE and, finally, Section 4.4 provides some numerical examples.

4.1 Literature review: existing 3D solutions

4.1.1 Saint–Venant solution

In the nineteen century, **Saint–Venant** (SV) proposed a completely different approach to beam modelling, i.e. he provided the solution of the continuum mechanic problem for a beam body assuming that: (i) the body is homogeneous and isotropic; (ii) no distributed-loads are applied; (iii) loads and displacement constraints are applied far from the region where the solution is evaluated; (iv) stress components orthogonal to the beam axis are negligible. Unfortunately, SV solution is not explicit because it depends on some unknown **warping functions**, governed by auxiliary Partial Differential Equations (PDEs) defined on the cross section. Readers may refer to (Timoshenko and Goodier, 1951) for more details.

Warping functions are deeply investigated not only in order to determine the SV solution, but also because they are useful in the evaluation of stiffness correction factors. As an example,

Gruttmann et al. (1999) discuss the physical meaning of the warping functions and propose a numerical approach to solve the auxiliary PDEs, comparing some numerical results with available analytical solutions. More recently, Lacarbonara and Paolone (2007) propose and compare different strategies to compute the warping functions, highlighting advantages and critical steps of each strategy. In general, the numerical computation of warping functions could be quite expensive. However, it must be done only once, after the section geometry definition. As a consequence, the procedure is usually adopted in frame-structure analysis.

4.1.2 Saint–Venant solution enhancements

In practical applications, many of the hypotheses that allow to obtain the SV solution could be too restrictive. An attempt to overcome the SV hypotheses was proposed by Ladeveze and Simmonds (1998) that derive an analytical beam model and the relative solution maintaining only hypothesis (iv) (stress components orthogonal to the beam axis are negligible). In addition to the SV solution, the resulting beam model can take into account also **local effects** like stress concentrations that occur in proximity of displacement constrained boundary.

A more general attempt to overcome the SV hypotheses was proposed by Dong et al. (2001); Kosmatka et al. (2001) and Lin et al. (2001) that apply the **dimensional reduction method** to the continuum mechanic PDEs problem in order to obtain a semi-analytical SV-like solution. The authors assume displacement as independent variable and the Total Potential Energy functional as starting point in derivation whereas no restrictive hypotheses on materials, stress description, and loads are considered. Some ODEs govern the resulting semi-analytical solution that describes effectively also local effects. Moreover, no correction factors are required.

4.2 Model derivation

In this section, starting from the 3D problem weak formulation (2.13), we perform the dimensional reduction which is based on the introduction of field cross-section approximations and on a cross-section integration. For simplicity, in the model derivation, we switch to an engineering-oriented notation.

4.2.1 Cross-section approximation and notations

Adopting Position (2.20) and switching to an engineering notation we set:

$$\mathbf{s} := \begin{Bmatrix} s_u \\ s_v \\ s_w \end{Bmatrix} \approx \begin{bmatrix} \mathbf{r}_u^T & \mathbf{0} & \mathbf{0} \\ \mathbf{0} & \mathbf{r}_v^T & \mathbf{0} \\ \mathbf{0} & \mathbf{0} & \mathbf{r}_w^T \end{bmatrix} \begin{Bmatrix} \hat{\mathbf{u}} \\ \hat{\mathbf{v}} \\ \hat{\mathbf{w}} \end{Bmatrix} = \mathbf{R}_s \hat{\mathbf{s}} \quad (4.1)$$

$$\boldsymbol{\sigma} := \begin{Bmatrix} \sigma_{xx} \\ \sigma_{yy} \\ \sigma_{zz} \\ \tau_{xy} \\ \tau_{xz} \\ \tau_{yz} \end{Bmatrix} \approx \begin{bmatrix} \mathbf{r}_{\sigma_x}^T & \mathbf{0} & \mathbf{0} & \mathbf{0} & \mathbf{0} & \mathbf{0} \\ \mathbf{0} & \mathbf{r}_{\sigma_y}^T & \mathbf{0} & \mathbf{0} & \mathbf{0} & \mathbf{0} \\ \mathbf{0} & \mathbf{0} & \mathbf{r}_{\sigma_z}^T & \mathbf{0} & \mathbf{0} & \mathbf{0} \\ \mathbf{0} & \mathbf{0} & \mathbf{0} & \mathbf{r}_{\tau_{xy}}^T & \mathbf{0} & \mathbf{0} \\ \mathbf{0} & \mathbf{0} & \mathbf{0} & \mathbf{0} & \mathbf{r}_{\tau_{xz}}^T & \mathbf{0} \\ \mathbf{0} & \mathbf{0} & \mathbf{0} & \mathbf{0} & \mathbf{0} & \mathbf{r}_{\tau_{yz}}^T \end{bmatrix} \begin{Bmatrix} \hat{\sigma}_x \\ \hat{\sigma}_y \\ \hat{\sigma}_z \\ \hat{\tau}_{xy} \\ \hat{\tau}_{xz} \\ \hat{\tau}_{yz} \end{Bmatrix} = \mathbf{R}_\sigma \hat{\boldsymbol{\sigma}} \quad (4.2)$$

In the same way we define the virtual field approximations:

$$\delta \mathbf{s} := \mathbf{R}_s \delta \hat{\mathbf{s}}; \quad \delta \boldsymbol{\sigma} := \mathbf{R}_\sigma \delta \hat{\boldsymbol{\sigma}}$$

According to the engineering notations just introduced, we re-define the differential operator and the normal unit vector product as follows:

$$\begin{array}{cc} \text{Tensor notation} & \text{Engineering notation} \\ \nabla \cdot \boldsymbol{\sigma} & \equiv \left(\frac{\partial}{\partial x} \mathbf{E}_1 + \frac{\partial}{\partial y} \mathbf{E}_2 + \frac{\partial}{\partial z} \mathbf{E}_3 \right) \mathbf{R}_\sigma \hat{\boldsymbol{\sigma}} \end{array} \quad (4.3)$$

$$\boldsymbol{\sigma} \cdot \mathbf{n} \equiv (n_x \mathbf{E}_1 + n_y \mathbf{E}_2 + n_z \mathbf{E}_3) \mathbf{R}_\sigma \hat{\boldsymbol{\sigma}} \quad (4.4)$$

where products between partial derivatives and boolean matrices \mathbf{E}_i , $i = 1, 2, 3$ must be intended as scalar-matrix products, whereas differential operators are applied to stress approximations $\mathbf{R}_\sigma \hat{\boldsymbol{\sigma}}$. The boolean matrices \mathbf{E}_i , $i = 1, 2, 3$, are defined as follows:

$$\mathbf{E}_1 := \begin{bmatrix} 1 & 0 & 0 & 0 & 0 & 0 \\ 0 & 0 & 0 & 1 & 0 & 0 \\ 0 & 0 & 0 & 0 & 1 & 0 \end{bmatrix}; \quad \mathbf{E}_2 := \begin{bmatrix} 0 & 0 & 0 & 1 & 0 & 0 \\ 0 & 1 & 0 & 0 & 0 & 0 \\ 0 & 0 & 0 & 0 & 0 & 1 \end{bmatrix}; \quad \mathbf{E}_3 := \begin{bmatrix} 0 & 0 & 0 & 0 & 1 & 0 \\ 0 & 0 & 0 & 0 & 0 & 1 \\ 0 & 0 & 1 & 0 & 0 & 0 \end{bmatrix} \quad (4.5)$$

In Chapter 2, we denoted with \mathbf{D}^{-1} the fourth order, linear, elastic, isotropic tensor, while from now on, with a small abuse, we use the same notation to indicate the corresponding square matrix obtained following the engineering notation. Therefore, we have:

$$\mathbf{D}^{-1} := \frac{1}{E} \begin{bmatrix} 1 & -\nu & -\nu & 0 & 0 & 0 \\ -\nu & 1 & -\nu & 0 & 0 & 0 \\ -\nu & -\nu & 1 & 0 & 0 & 0 \\ 0 & 0 & 0 & 2(1+\nu) & 0 & 0 \\ 0 & 0 & 0 & 0 & 2(1+\nu) & 0 \\ 0 & 0 & 0 & 0 & 0 & 2(1+\nu) \end{bmatrix} \quad (4.6)$$

Due to assumption (2.20), computation of partial derivatives is straightforward:

$$\frac{\partial}{\partial x} \gamma = \mathbf{r}_\gamma^T \frac{d}{dx} \hat{\boldsymbol{\gamma}} = \mathbf{r}_\gamma^T \hat{\boldsymbol{\gamma}}'; \quad \frac{\partial}{\partial y} \gamma = \frac{\partial}{\partial y} \mathbf{r}_\gamma^T \hat{\boldsymbol{\gamma}} = \mathbf{r}_{\gamma,y}^T \hat{\boldsymbol{\gamma}}; \quad \frac{\partial}{\partial z} \gamma = \frac{\partial}{\partial z} \mathbf{r}_\gamma^T \hat{\boldsymbol{\gamma}} = \mathbf{r}_{\gamma,z}^T \hat{\boldsymbol{\gamma}} \quad (4.7)$$

where the prime means the derivative along x , $(\cdot)_{,y}$ and $(\cdot)_{,z}$ mean derivatives along y and z , respectively.

4.2.2 Model formulation

In the following we assume that $\partial\Omega_s = A_0$, $\partial\Omega_t = A_l \cup L$, and the lateral surface is unloaded, i.e.: $\mathbf{t}|_L = \mathbf{0}$. The unloaded lateral surface is an usual assumption in beam modelling. However, we notice that the model derivation can be performed taking into account arbitrary load conditions as well.

In order to strongly satisfy the boundary equilibrium, according to the definition of S_t^{dd} , see (2.15), we assume that the external traction $\mathbf{t}|_{A_l}$ can be exactly represented using the profiles \mathbf{R}_σ . This means that there exist suitable vectors $\hat{\mathbf{t}}_x$, $\hat{\mathbf{t}}_y$, and $\hat{\mathbf{t}}_z$ such that:

$$\mathbf{t}|_{A_l} = \begin{Bmatrix} \mathbf{r}_{\sigma_x}^T \hat{\mathbf{t}}_x \\ \mathbf{r}_{\tau_{xy}}^T \hat{\mathbf{t}}_y \\ \mathbf{r}_{\tau_{xz}}^T \hat{\mathbf{t}}_z \end{Bmatrix} \quad (4.8)$$

Since $\mathbf{n}|_{A_l} = (1, 0, 0)^T$, Definition (4.4) becomes $\boldsymbol{\sigma} \cdot \mathbf{n}|_{A_l} = \mathbf{E}_1 \mathbf{R}_\sigma \hat{\boldsymbol{\sigma}}(\bar{l})$ and the essential boundary

condition $\boldsymbol{\sigma} \cdot \mathbf{n}|_{A_l} = \mathbf{t}|_{A_l}$ can be expressed as follows:

$$\begin{Bmatrix} \hat{\boldsymbol{\sigma}}_x(\bar{l}) \\ \hat{\boldsymbol{\tau}}_{xy}(\bar{l}) \\ \hat{\boldsymbol{\tau}}_{xz}(\bar{l}) \end{Bmatrix} = \begin{Bmatrix} \hat{\mathbf{t}}_x \\ \hat{\mathbf{t}}_y \\ \hat{\mathbf{t}}_z \end{Bmatrix} \quad (4.9)$$

Introducing the engineering notation and the approximations defined in section 4.2.1, variational problem (2.13) becomes:

$$\begin{aligned} \delta J_{HR} = & - \int_{\Omega} \delta \hat{\mathbf{s}}^T \mathbf{R}_s^T \left[\left(\frac{d}{dx} \mathbf{E}_1 + \frac{\partial}{\partial y} \mathbf{E}_2 + \frac{\partial}{\partial z} \mathbf{E}_3 \right) \mathbf{R}_{\sigma} \hat{\boldsymbol{\sigma}} \right] d\Omega \\ & - \int_{\Omega} \left[\left(\frac{d}{dx} \mathbf{E}_1 + \frac{\partial}{\partial y} \mathbf{E}_2 + \frac{\partial}{\partial z} \mathbf{E}_3 \right) \mathbf{R}_{\sigma} \delta \hat{\boldsymbol{\sigma}} \right]^T \mathbf{R}_s \hat{\mathbf{s}} d\Omega \\ & - \int_{\Omega} \delta \hat{\boldsymbol{\sigma}}^T \mathbf{R}_{\sigma}^T \mathbf{D}^{-1} \mathbf{R}_{\sigma} \hat{\boldsymbol{\sigma}} d\Omega - \int_{\Omega} \delta \hat{\mathbf{s}}^T \mathbf{R}_s^T \mathbf{f} d\Omega \\ & + \int_{\partial\Omega_s} [(n_x \mathbf{E}_1 + n_y \mathbf{E}_2 + n_z \mathbf{E}_3) \mathbf{R}_{\sigma} \delta \hat{\boldsymbol{\sigma}}]^T \bar{\boldsymbol{\tau}} dA = 0 \end{aligned} \quad (4.10)$$

Expanding products, introducing the derivative notation (4.7), and recalling that $\partial\Omega_s = A_0$, Equation (4.10) becomes:

$$\begin{aligned} \delta J_{HR} = & - \int_{\Omega} (\delta \hat{\mathbf{s}}^T \mathbf{R}_s^T \mathbf{E}_1 \mathbf{R}_{\sigma} \hat{\boldsymbol{\sigma}}' + \delta \hat{\mathbf{s}}^T \mathbf{R}_s^T \mathbf{E}_2 \mathbf{R}_{\sigma,y} \hat{\boldsymbol{\sigma}} + \delta \hat{\mathbf{s}}^T \mathbf{R}_s^T \mathbf{E}_3 \mathbf{R}_{\sigma,z} \hat{\boldsymbol{\sigma}} \\ & + \delta \hat{\boldsymbol{\sigma}}'^T \mathbf{R}_{\sigma}^T \mathbf{E}_1^T \mathbf{R}_s \hat{\mathbf{s}} + \delta \hat{\boldsymbol{\sigma}}'^T \mathbf{R}_{\sigma}^T \mathbf{E}_2^T \mathbf{R}_s \hat{\mathbf{s}} + \delta \hat{\boldsymbol{\sigma}}'^T \mathbf{R}_{\sigma}^T \mathbf{E}_3^T \mathbf{R}_s \hat{\mathbf{s}} \\ & + \delta \hat{\boldsymbol{\sigma}}^T \mathbf{R}_{\sigma}^T \mathbf{D}^{-1} \mathbf{R}_{\sigma} \hat{\boldsymbol{\sigma}} + \delta \hat{\mathbf{s}}^T \mathbf{R}_s^T \mathbf{f}) d\Omega \\ & - \int_{A_0} \delta \hat{\boldsymbol{\sigma}}^T \mathbf{R}_{\sigma}^T \mathbf{E}_1^T \bar{\boldsymbol{\tau}} dA = 0 \end{aligned} \quad (4.11)$$

Splitting the integral on the domain Ω into an integral along the axis l and an integral on the cross section A , Equation (4.11) becomes:

$$\delta J_{HR} = - \int_l (\delta \hat{\mathbf{s}}^T \mathbf{G}_{s\sigma} \hat{\boldsymbol{\sigma}}' + \delta \hat{\mathbf{s}}^T \mathbf{H}_{s\sigma} \hat{\boldsymbol{\sigma}} + \delta \hat{\boldsymbol{\sigma}}'^T \mathbf{G}_{\sigma s} \hat{\mathbf{s}} + \delta \hat{\boldsymbol{\sigma}}^T \mathbf{H}_{\sigma s} \hat{\mathbf{s}} + \delta \hat{\boldsymbol{\sigma}}^T \mathbf{H}_{\sigma\sigma} \hat{\boldsymbol{\sigma}} + \delta \hat{\mathbf{s}}^T \mathbf{F}) dx - \delta \hat{\boldsymbol{\sigma}}^T \bar{\boldsymbol{\tau}} = 0 \quad (4.12)$$

where

$$\begin{aligned} \mathbf{H}_{s\sigma} &:= \mathbf{H}_{s\sigma}^T = \int_A (\mathbf{R}_s^T \mathbf{E}_2 \mathbf{R}_{\sigma,y} + \mathbf{R}_s^T \mathbf{E}_3 \mathbf{R}_{\sigma,z}) dA; \quad \mathbf{H}_{\sigma\sigma} := \int_A \mathbf{R}_{\sigma}^T \mathbf{D}^{-1} \mathbf{R}_{\sigma} dA \\ \mathbf{G}_{s\sigma} &= \mathbf{G}_{s\sigma}^T := \int_A \mathbf{R}_s^T \mathbf{E}_1 \mathbf{R}_{\sigma} dA; \quad \mathbf{F} := \int_A \mathbf{R}_s^T \mathbf{f} dA; \quad \bar{\boldsymbol{\tau}} = \int_{A_0} \mathbf{R}_{\sigma}^T \mathbf{E}_1 \bar{\boldsymbol{\tau}} dA \end{aligned}$$

Equation (4.12) represents the weak formulation of the beam model: the integrals are defined only along the beam axis, whereas the cross-section integrals become coefficient matrices.

To obtain the corresponding strong formulation, i.e. the associated ODE system, we need to integrate by parts the third term of Equation (4.12):

$$- \int_l \delta \hat{\boldsymbol{\sigma}}'^T \mathbf{G}_{\sigma s} \hat{\mathbf{s}} dx = - \delta \hat{\boldsymbol{\sigma}}^T \mathbf{G}_{\sigma s} \hat{\mathbf{s}} \Big|_{x=0}^{x=\bar{l}} + \int_l \delta \hat{\boldsymbol{\sigma}}^T \mathbf{G}_{\sigma s} \hat{\mathbf{s}}' dx \quad (4.13)$$

Substituting Equation (4.13) in Equation (4.12), recalling that $\delta \hat{\boldsymbol{\sigma}}(\bar{l}) = \mathbf{0}$, and collecting the unknowns in a vector, we obtain:

$$\int_l [\delta \hat{\mathbf{s}}^T; \delta \hat{\boldsymbol{\sigma}}^T] \left(\mathbf{G} \begin{Bmatrix} \hat{\mathbf{s}}' \\ \hat{\boldsymbol{\sigma}}' \end{Bmatrix} + \mathbf{H} \begin{Bmatrix} \hat{\mathbf{s}} \\ \hat{\boldsymbol{\sigma}} \end{Bmatrix} - \begin{Bmatrix} \mathbf{F} \\ \mathbf{0} \end{Bmatrix} \right) dx - \delta \hat{\boldsymbol{\sigma}}^T (\bar{\boldsymbol{\tau}} - \mathbf{G}_{\sigma s} \hat{\mathbf{s}}) = 0 \quad (4.14)$$

where

$$\mathbf{G} := \begin{bmatrix} \mathbf{0} & -\mathbf{G}_{s\sigma} \\ \mathbf{G}_{\sigma s} & \mathbf{0} \end{bmatrix}; \quad \mathbf{H} := \begin{bmatrix} \mathbf{0} & -\mathbf{H}_{s\sigma} \\ -\mathbf{H}_{\sigma s} & -\mathbf{H}_{\sigma\sigma} \end{bmatrix} \quad (4.15)$$

Since Equation (4.14) needs to be satisfied for all the possible virtual fields, we obtain the following ODE, equipped with the essential boundary condition (4.9).

$$\begin{cases} \mathbf{G} \begin{Bmatrix} \hat{\mathbf{s}}' \\ \hat{\boldsymbol{\sigma}}' \end{Bmatrix} + \mathbf{H} \begin{Bmatrix} \hat{\mathbf{s}} \\ \hat{\boldsymbol{\sigma}} \end{Bmatrix} = \begin{Bmatrix} \mathbf{F} \\ \mathbf{0} \end{Bmatrix} & \text{in } l \\ \mathbf{G}_{\sigma s} \hat{\mathbf{s}} = \overline{\mathbf{S}} & \text{at } x = 0 \\ \hat{\boldsymbol{\sigma}}_x = \hat{\mathbf{t}}_x & \text{at } x = \bar{l} \\ \hat{\boldsymbol{\tau}}_{xy} = \hat{\mathbf{t}}_y & \text{at } x = \bar{l} \\ \hat{\boldsymbol{\tau}}_{xz} = \hat{\mathbf{t}}_z & \text{at } x = \bar{l} \end{cases} \quad (4.16)$$

We notice that, since \mathbf{H} contains only y and z derivatives, it governs a generalized plane strain problem defined in the cross section. Furthermore, looking at the definition of \mathbf{G} (see (4.15)–(4.13)) and at the definition of the boolean matrix \mathbf{E}_1 (see (4.5)), we observe that all the coefficients multiplying $\hat{\boldsymbol{\sigma}}'_y$, $\hat{\boldsymbol{\sigma}}'_z$, and $\hat{\boldsymbol{\tau}}'_{yz}$ vanish. As a consequence, we conclude that the beam model (4.16) is an algebraic-differential problem where at least $\hat{\boldsymbol{\sigma}}_y$, $\hat{\boldsymbol{\sigma}}_z$, and $\hat{\boldsymbol{\tau}}_{yz}$ are determined through purely algebraic equations.

4.2.3 Cross-section shape functions definition

Due to the domain definition (2.1) we can represent the stress tensor as follows:

$$\boldsymbol{\sigma} := \begin{bmatrix} \sigma_l & \boldsymbol{\tau}_{lA} \\ \boldsymbol{\tau}_{Al} & \boldsymbol{\sigma}_A \end{bmatrix} \quad (4.17)$$

where

$$\sigma_l := \sigma_{xx}; \quad \boldsymbol{\tau}_{lA} = \boldsymbol{\tau}_{Al}^T := [\tau_{xy}; \tau_{xz}]; \quad \boldsymbol{\sigma}_A := \begin{bmatrix} \sigma_{yy} & \tau_{yz} \\ \tau_{zy} & \sigma_{zz} \end{bmatrix}$$

Accordingly, we represent the divergence operator as follows:

$$\nabla := \left\{ \begin{array}{c} \frac{\partial}{\partial x} \\ \nabla_A \end{array} \right\} \quad \text{where} \quad \nabla_A := \left\{ \begin{array}{c} \frac{\partial}{\partial y} \\ \frac{\partial}{\partial z} \end{array} \right\} \quad (4.18)$$

We first recall that the space definition (2.15) requires in particular $\boldsymbol{\sigma} \in H(\text{div}, \Omega)$. Therefore, we must choose $\boldsymbol{\sigma}$ such that $(\nabla \cdot \boldsymbol{\sigma}) \in L^2(\Omega)$, i.e.:

$$\nabla \cdot \boldsymbol{\sigma} = \left\{ \begin{array}{c} \frac{\partial}{\partial x} \sigma_l + \nabla_A \cdot \boldsymbol{\tau}_{lA} \\ \frac{\partial}{\partial x} \boldsymbol{\tau}_{Al} + \nabla_A \cdot \boldsymbol{\sigma}_A \end{array} \right\} \in L^2(\Omega) \quad (4.19)$$

Sufficient conditions that guarantee the satisfaction of (4.19) are the following:

$$\frac{\partial}{\partial x} \sigma_l \in L^2(\Omega); \quad \nabla_A \cdot \boldsymbol{\tau}_{lA} \in L^2(\Omega); \quad \frac{\partial}{\partial x} \boldsymbol{\tau}_{Al} \in L^2(\Omega); \quad \nabla_A \cdot \boldsymbol{\sigma}_A \in L^2(\Omega) \quad (4.20)$$

In addition to Conditions (4.20), as suggested by Alessandrini et al. (1999), to ensure that the model is *well-posed*, one possible choice is to require the following condition:

$$\nabla \cdot S^{dd} = W^{dd} \quad (4.21)$$

Given a generic cross-section geometry, it is not trivial to define cross-section shape functions that satisfy conditions (4.20) and (4.21). As a consequence, we start focusing on the simplest case, i.e. a beam with a rectangular cross-section:

$$A = \left\{ (y; z) \in \mathbb{R}^2 : y \in \left[-\frac{h}{2}, \frac{h}{2} \right] \text{ and } z \in \left[-\frac{b}{2}, \frac{b}{2} \right] \right\}$$

where h is the beam thickness and b is the beam depth. Due to the simplicity of the considered geometry, the cross-section shape functions can be defined as the tensor products of two **profile function vectors** $\mathbf{p}_\gamma(y)$ and $\mathbf{q}_\gamma(z)$:

$$\mathbf{p}_\gamma : h \rightarrow \mathbb{R}^g; \quad \mathbf{q}_\gamma : b \rightarrow \mathbb{R}^k; \quad \mathbf{r}_\gamma^T := \text{vec}(\mathbf{p}_\gamma(y) \mathbf{q}_\gamma^T(z)) \quad (4.22)$$

where $\text{vec}(\cdot)$ is the linear operator that re-arranges a tensor into a row vector. Obviously the g components of \mathbf{p}_γ and the k components of \mathbf{q}_γ are sets of linearly independent functions.

Due to the introduction of profile function definition (4.22), we can express Condition (4.21) as follows (cf. also (4.1) and (4.2)).

Given $\hat{\mathbf{s}}$, there exists $\hat{\boldsymbol{\sigma}}$ such that:

$$\text{vec}(\mathbf{p}_{\sigma_x} \mathbf{q}_{\sigma_x}^T) \hat{\boldsymbol{\sigma}}'_x + \text{vec}(\mathbf{p}'_{\tau_{xy}} \mathbf{q}_{\tau_{xy}}^T) \hat{\boldsymbol{\tau}}_{xy} + \text{vec}(\mathbf{p}_{\tau_{xz}} \mathbf{q}_{\tau_{xz}}^T) \hat{\boldsymbol{\tau}}_{xz} = \text{vec}(\mathbf{p}_u \mathbf{q}_u^T) \hat{\mathbf{u}} \quad (4.23)$$

$$\text{vec}(\mathbf{p}_{\tau_{xy}} \mathbf{q}_{\tau_{xy}}^T) \hat{\boldsymbol{\tau}}'_{xy} + \text{vec}(\mathbf{p}'_{\sigma_y} \mathbf{q}_{\sigma_y}^T) \hat{\boldsymbol{\sigma}}_y + \text{vec}(\mathbf{p}_{\tau_{yz}} \mathbf{q}_{\tau_{yz}}^T) \hat{\boldsymbol{\tau}}_{yz} = \text{vec}(\mathbf{p}_v \mathbf{q}_v^T) \hat{\mathbf{v}} \quad (4.24)$$

$$\text{vec}(\mathbf{p}_{\tau_{xz}} \mathbf{q}_{\tau_{xz}}^T) \hat{\boldsymbol{\tau}}'_{xz} + \text{vec}(\mathbf{p}'_{\tau_{yz}} \mathbf{q}_{\tau_{yz}}^T) \hat{\boldsymbol{\tau}}_{yz} + \text{vec}(\mathbf{p}_{\sigma_z} \mathbf{q}_{\sigma_z}^T) \hat{\boldsymbol{\sigma}}_z = \text{vec}(\mathbf{p}_w \mathbf{q}_w^T) \hat{\mathbf{w}}, \quad (4.25)$$

and viceversa.

We consider complete polynomials as profile functions and we denote with $\deg(\cdot)$ their maximum degree. As a consequence, to satisfy Equations (4.23), (4.24), and (4.25) we enforce the following “natural” conditions:

$$\begin{aligned} \deg(\mathbf{p}_{\sigma_x}) &= \deg(\mathbf{p}_{\tau_{xy}}) - 1 = \deg(\mathbf{p}_{\tau_{xz}}) = \deg(\mathbf{p}_u) \\ \deg(\mathbf{p}_{\tau_{xy}}) &= \deg(\mathbf{p}_{\sigma_y}) - 1 = \deg(\mathbf{p}_{\tau_{yz}}) = \deg(\mathbf{p}_v) \\ \deg(\mathbf{p}_{\tau_{xz}}) &= \deg(\mathbf{p}_{\tau_{yz}}) - 1 = \deg(\mathbf{p}_{\sigma_z}) = \deg(\mathbf{p}_w) \\ \deg(\mathbf{q}_{\sigma_x}) &= \deg(\mathbf{q}_{\tau_{xy}}) = \deg(\mathbf{q}_{\tau_{xz}}) - 1 = \deg(\mathbf{q}_u) \\ \deg(\mathbf{q}_{\tau_{xy}}) &= \deg(\mathbf{q}_{\sigma_y}) = \deg(\mathbf{q}_{\tau_{yz}}) - 1 = \deg(\mathbf{q}_v) \\ \deg(\mathbf{q}_{\tau_{xz}}) &= \deg(\mathbf{q}_{\tau_{yz}}) = \deg(\mathbf{q}_{\sigma_z}) - 1 = \deg(\mathbf{q}_w) \end{aligned} \quad (4.26)$$

Table 4.1 displays the degree of profile functions \mathbf{p}_γ and \mathbf{q}_γ , assuming $\deg(\mathbf{p}_{\tau_{xy}}) = \deg(\mathbf{q}_{\tau_{xz}}) = 2$ and imposing Equation (4.26).

As illustrated in Figure 4.2, we can define non-elementary cross-sections assembling elementary rectangular blocks that we call **fibers** and we suppose to be homogeneous. We construct the non elementary cross-section shape functions \mathbf{r}_γ considering the profile functions so far defined on each fiber, requiring the profile-function continuities specified in Table 4.1, and imposing the essential boundary condition $\boldsymbol{\sigma} \cdot \mathbf{n}|_{\partial A} = \mathbf{0}$. We specify that profile-function continuities are fixed in order to satisfy Condition (4.20).

4.2.4 Beam-model examples

In this sub-section we evaluate and discuss the solution of the beam model (4.16) for the homogeneous beam with square cross section depicted in Figure 4.3. We assume that the properties

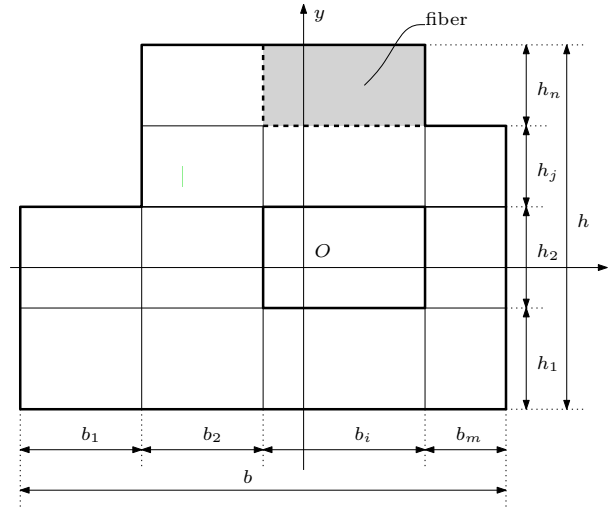
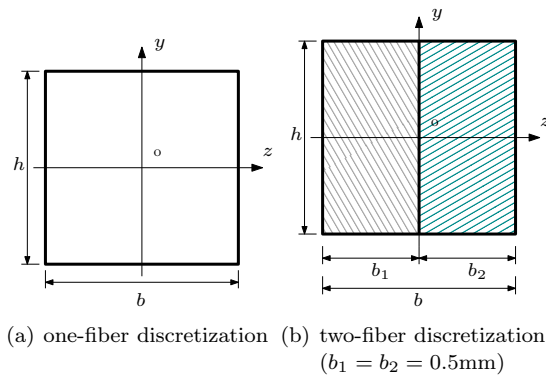


Figure 4.2: Non-elementary cross-section geometry definition, dimensions, and adopted notations.

Figure 4.3: Homogeneous, square cross-section: dimensions and adopted discretization ($h = b = 1\text{mm}$, $E = 10^5\text{MPa}$, and $\nu = 0.25$).

Variable	deg (\mathbf{p}_γ)	y cont.	deg (\mathbf{q}_γ)	z cont.
u	1	C^{-1}	1	C^{-1}
v	2	C^{-1}	1	C^{-1}
w	1	C^{-1}	2	C^{-1}
σ_x	1	C^{-1}	1	C^{-1}
σ_y	3	C^0	1	C^{-1}
σ_z	1	C^{-1}	3	C^0
τ_{xy}	2	C^0	1	C^{-1}
τ_{xz}	1	C^{-1}	2	C^0
τ_{yz}	2	C^0	2	C^0

Table 4.1: Degree and continuity of cross-section profile functions (C^{-1} means discontinuous function).

of the material are $E = 10^5$ MPa and $\nu = 0.25$ and, with respect to the notation introduced in Figure 4.2, the cross-section dimensions are $h = b = 1$ mm. We model the physical problem using 2 cross-section discretization: the **one-fiber cross-section discretization**, depicted in Sub-figure 4.3(a), and the **two-fiber cross-section discretization**, depicted in Sub-figure 4.3(b); the aim of these modelling choices is to appreciate the effect of different discretization refinement.

In the following, the matrices \mathbf{G} and \mathbf{H} are evaluated trough symbolic-calculus functions, whereas the further results are obtained using numerical-calculus functions, both implemented in MAPLE software.

4.2.4.1 One-fiber cross-section

After imposition of the lateral free-traction boundary condition, the one-fiber cross-section beam has 33 unknowns. In the following we will not report the definition of matrices \mathbf{G} and \mathbf{H} , due to their weight, nevertheless we could highlight the following statements.

Since $\text{rank}(\mathbf{G}) = 16$, in the considered example we can distinguish between 16 unknowns that are solutions of a differential problem, and the remaining 17 that are algebraically determined by linear combination of the differential problem solutions. As already observed at the end of Sub-section 4.2.2, the 9 $\hat{\sigma}_y$, $\hat{\sigma}_z$, and $\hat{\tau}_{yz}$ axial coefficient functions are among the ones algebraically determined. Moreover, looking at Equation (4.16) for the considered example, the boundary conditions are 16, since $\text{rank}(\mathbf{G}_{\sigma s}) = 8$ and the boundary equilibrium consists of 8 conditions. Therefore, the number of boundary conditions and the number of essential first order differential equations in (4.16) perfectly match.

As already explained in Auricchio et al. (2010), to construct the homogeneous solution of ODEs (4.16), we need the solution of the generalized eigenvalue problem:

$$\det(\lambda \mathbf{G} + \mathbf{H}) = 0 \quad (4.27)$$

where λ is the eigenvalue. For the case under investigation we obtain:

$$\lambda = \left\{ \begin{array}{c} \sim 0 \\ \pm 3.3652 \pm 1.1509i \end{array} \right\} \quad \begin{array}{c} [12] \\ [4] \end{array}$$

where the numbers in square brackets are the eigenvalue multiplicities (considering all the possible combination of sign of real and imaginary parts) and the notation ~ 0 means that the eigenvalues vanish up to the machine precision.

4.2.4.2 Two-fiber cross-section

After imposition of the lateral free-traction boundary condition, the two-fiber cross-section beam has 71 independent unknowns. Moreover, $\text{rank}(\mathbf{G}) = 36$. Hence, 36 unknowns are solution of a differential problem, whereas the remaining 35 are algebraically determined by linear combination of the differential problem solutions. Looking at Equation (4.16) for the considered example, the boundary conditions are 36, since $\text{rank}(\mathbf{G}_{\sigma_s}) = 18$ and the boundary equilibrium consists of 18 conditions. Therefore, the number of boundary conditions and the number of essential first order differential equations in (4.16) perfectly match for this case, too.

In the two-fiber beam, the solution of the generalized eigenvalue problem (4.27) is:

$$\lambda = \left\{ \begin{array}{l} \sim 0 \\ \pm 11.786 \\ \pm 10.116 \\ \pm 10.022 \\ \pm 8.2174 \\ \pm 8.1037 \\ \pm 4.5891 \pm 1.2945i \\ \pm 5.6931 \pm 0.4331i \\ \pm 4.9317 \\ \pm 3.3520 \pm 1.1591i \end{array} \right\} \begin{array}{l} [12] \\ [2] \\ [2] \\ [2] \\ [2] \\ [2] \\ [4] \\ [4] \\ [2] \\ [4] \end{array}$$

and it is going to be discussed in the next Sub-section.

4.2.4.3 Conclusions on beam models

We computed the solutions of the homogeneous problem associated to (4.16) for the beam models so far introduced, but we do not report them since their expressions are too long. However, the following remarks about the solution structure apply.

- Zero eigenvalues lead to polynomial terms, that correspond to the polynomial terms that appear also in the Saint-Venant solution. In particular, the 12 zero eigenvalues correspond to the 6 rigid body translations and to the 6 uniform deformations: extension, torque, two bendings, and two shears (associated with bendings).
- Non-zero, complex conjugate or real eigenvalues (generally represented as $\pm a \pm ib$) lead to harmonic dumped functions like $C_i e^{\pm ax} \sin(bx + C_j)$, that describe local effects near the boundaries, as it happens in other beam models, like Ladeveze and Simmonds (1998) and Allix and Dupleix-Couderc (2010).

Similar conclusions was also reported in Lin et al. (2001) where, moreover, the authors specify that the real part of the eigenvalue defines the inverse decay length of the corresponding boundary effect. As a consequence, the smallest eigenvalue real-part provides an estimation of the length of the axis region where boundary effects are not negligible.

From the comparison between the one- and two-fiber cross-section beam models, it is possible to draw some additional observations.

- The number of eigenvalues corresponds exactly to the rank of \mathbf{G} matrix i.e. to the number of differential equations governing the problem.
- The number of null eigenvalues does not change. As a consequence, we may conclude that the polynomial terms in the solution are independent from the number of considered fibers.

- Instead, the number of non-zero eigenvalues increases with the fiber number. As a consequence, we may conclude that a finer discretization improves at least the accuracy of the description of local effects.
- The decay lengths of the two models are not so different (the smallest real part of eigenvalues are 3.3652 and 3.3520 for one- and two- fiber cross-sections, respectively). As a consequence, we may conclude that also the simplest model is effective in the evaluation of this parameter.
- In both models, the inverse of decay length ensures that the magnitude of dumped functions is reduced of more than the 96% of its initial value, in a length of 1mm.

The independence of the polynomial solution with respect to the number of fibers suggests the idea that the modelling far from the extremal cross sections could be done by means of few global degrees of freedom, as in EB beam model. However, this idea will be the topic of future investigations.

4.3 FE derivation

The goal of this section is to obtain a displacement-based beam FE formulation. Accordingly, we introduce an approximation along the x direction, modify the beam-model weak formulation (4.12), and perform an integration along the axis. The procedure reduces the algebraic-differential equation system (4.16) to a pure algebraic equation system.

4.3.1 Weak problem formulation

In the following, we assume that the beam is clamped in A_0 , i.e. $\bar{\mathbf{s}} = \mathbf{0}$. Starting from beam-model weak formulation (4.12), we integrate by parts with respect to the x direction both the first and the third terms obtaining the following, alternative beam-model weak formulation:

Find $\hat{\mathbf{s}} \in \widetilde{W}$ and $\hat{\boldsymbol{\sigma}} \in \widetilde{S}$ such that $\forall \delta \hat{\mathbf{s}} \in \widetilde{W}$ and $\forall \delta \hat{\boldsymbol{\sigma}} \in \widetilde{S}$

$$\delta J_{HR} = \int_l (\delta \hat{\mathbf{s}}'^T \mathbf{G}_{s\sigma} \hat{\boldsymbol{\sigma}} - \delta \hat{\mathbf{s}}^T \mathbf{H}_{s\sigma} \hat{\boldsymbol{\sigma}} + \delta \hat{\boldsymbol{\sigma}}^T \mathbf{G}_{\sigma s} \hat{\mathbf{s}}' - \delta \hat{\boldsymbol{\sigma}}^T \mathbf{H}_{\sigma s} \hat{\mathbf{s}} - \delta \hat{\boldsymbol{\sigma}}^T \mathbf{H}_{\sigma\sigma} \hat{\boldsymbol{\sigma}} - \delta \hat{\mathbf{s}}^T \mathbf{F}) dx - \delta \hat{\mathbf{s}}^T \mathbf{T} = 0$$

(4.28)

where $\mathbf{T} := \int_{A_l} \mathbf{R}_s^T \mathbf{t} dA$, $\widetilde{W} := \{ \hat{\mathbf{s}} \in H^1(l) : \hat{\mathbf{s}}|_{x=0} = \mathbf{0} \}$, and $\widetilde{S} := L^2(l)$. We recall that:

$$L^2(l) := \left\{ \hat{\boldsymbol{\sigma}} : \int_l \hat{\boldsymbol{\sigma}}^T \hat{\boldsymbol{\sigma}} dx < \infty \right\}; \quad H^1(l) := \{ \hat{\mathbf{s}} : \hat{\mathbf{s}}, \hat{\mathbf{s}}' \in L^2(l) \}$$

4.3.2 FE formulation

The FE discretization of the model follows from the introduction of the axial shape function approximation (2.21) into the beam-model weak formulation (4.28):

$$\begin{aligned} \delta J_{HR} = \int_l \big(& \delta \tilde{\mathbf{s}}^T \mathbf{N}_s'^T \mathbf{G}_{s\sigma} \mathbf{N}_\sigma \tilde{\boldsymbol{\sigma}} - \delta \tilde{\mathbf{s}}^T \mathbf{N}_s^T \mathbf{H}_{s\sigma} \mathbf{N}_\sigma \tilde{\boldsymbol{\sigma}} + \delta \tilde{\boldsymbol{\sigma}}^T \mathbf{N}_\sigma^T \mathbf{G}_{\sigma s} \mathbf{N}_s' \tilde{\mathbf{s}} - \delta \tilde{\boldsymbol{\sigma}}^T \mathbf{N}_\sigma^T \mathbf{H}_{\sigma s} \mathbf{N}_s \tilde{\mathbf{s}} \\ & - \delta \tilde{\boldsymbol{\sigma}}^T \mathbf{N}_\sigma^T \mathbf{H}_{\sigma\sigma} \mathbf{N}_\sigma \tilde{\boldsymbol{\sigma}} - \delta \tilde{\mathbf{s}}^T \mathbf{N}_s^T \mathbf{F} \big) dx - \delta \tilde{\mathbf{s}}^T \mathbf{N}_s^T \mathbf{T} = 0 \end{aligned} \quad (4.29)$$

Collecting unknown coefficients in a vector and requiring (4.29) to be satisfied for all possible virtual fields, we obtain the following algebraic equation system:

$$\begin{bmatrix} \mathbf{0} & \mathbf{K}_{s\sigma} \\ \mathbf{K}_{\sigma s} & \mathbf{K}_{\sigma\sigma} \end{bmatrix} \begin{Bmatrix} \tilde{\mathbf{s}} \\ \tilde{\boldsymbol{\sigma}} \end{Bmatrix} = \begin{Bmatrix} \tilde{\mathbf{T}} \\ \mathbf{0} \end{Bmatrix} \quad (4.30)$$

where

$$\begin{aligned} \mathbf{K}_{s\sigma} &= \mathbf{K}_{\sigma s}^T := \int_l (\mathbf{N}_s'^T \mathbf{G}_{s\sigma} \mathbf{N}_\sigma - \mathbf{N}_s^T \mathbf{H}_{s\sigma} \mathbf{N}_\sigma) dx \\ \mathbf{K}_{\sigma\sigma} &:= - \int_l \mathbf{N}_\sigma^T \mathbf{H}_{\sigma\sigma} \mathbf{N}_\sigma dx; \quad \tilde{\mathbf{T}} := \int_l \mathbf{N}_s^T \mathbf{F} dx + \mathbf{N}_s^T|_{x=\tilde{l}} \mathbf{T} \end{aligned}$$

We highlight the following remarks.

- Since $\hat{\mathbf{s}} \in \widetilde{W}$, the continuity of displacements along the beam axis is satisfied *a priori*, whereas axial equilibrium is *weakly* imposed through Equation (4.28).
- The weak formulation (4.28) is symmetric.

4.3.3 Axial shape functions definition

In this sub-section we specify how to choose the FE approximation spaces. We first notice that, since $\mathbf{s} \in H^1(l)$, we need to impose axial continuity on displacements. Instead, since $\boldsymbol{\sigma} \in L^2(l)$ stress components can be axial-discontinuous, and in general it is convenient that they are so. Furthermore, to properly balance the discrete spaces, it seems reasonable to choose \widetilde{W} and \widetilde{S} satisfying: $\forall \hat{\boldsymbol{\sigma}} \in \widetilde{S}$ there exists $\hat{\mathbf{s}} \in \widetilde{W}$ such that

$$\frac{d}{dx} \hat{\mathbf{s}} = \mathbf{E}_1 \hat{\boldsymbol{\sigma}}; \quad \hat{\mathbf{s}} = \mathbf{E}_2 \hat{\boldsymbol{\sigma}}; \quad \hat{\mathbf{s}} = \mathbf{E}_3 \hat{\boldsymbol{\sigma}}, \quad (4.31)$$

and viceversa.

Accordingly, we require the following conditions on the axial shape functions:

$$\begin{aligned} \deg(\mathbf{N}_u) &= \deg(\mathbf{N}_{\sigma_x}) + 1 = \deg(\mathbf{N}_{\tau_{xy}}) = \deg(\mathbf{N}_{\tau_{xz}}) \\ \deg(\mathbf{N}_v) &= \deg(\mathbf{N}_{\tau_{xy}}) + 1 = \deg(\mathbf{N}_{\sigma_y}) = \deg(\mathbf{N}_{\tau_{yz}}) \\ \deg(\mathbf{N}_w) &= \deg(\mathbf{N}_{\tau_{xz}}) + 1 = \deg(\mathbf{N}_{\tau_{yz}}) = \deg(\mathbf{N}_{\sigma_z}) \end{aligned} \quad (4.32)$$

Assuming $\deg(\mathbf{N}_v) = 3$ and imposing Equations (4.32), we determine the degree of axis shape functions \mathbf{N}_γ , summarized in Table 4.2 together with properties of profile vectors.

Variable	$\deg(\mathbf{p}_\gamma)$	y cont.	$\deg(\mathbf{q}_\gamma)$	z cont.	$\deg(\mathbf{N}_\gamma)$	x cont.
u	1	C^{-1}	1	C^{-1}	2	C^0
v	2	C^{-1}	1	C^{-1}	3	C^0
w	1	C^{-1}	2	C^{-1}	3	C^0
σ_x	1	C^{-1}	1	C^{-1}	1	C^{-1}
σ_y	3	C^0	1	C^{-1}	3	C^{-1}
σ_z	1	C^{-1}	3	C^0	3	C^{-1}
τ_{xy}	2	C^0	1	C^{-1}	2	C^{-1}
τ_{xz}	1	C^{-1}	2	C^0	2	C^{-1}
τ_{yz}	2	C^0	2	C^0	3	C^{-1}

Table 4.2: Degree and continuity of cross-section profile functions and axis shape functions (C^{-1} means discontinuous function)

Looking at the properties of the axial shape functions summarized in Table 4.2, we notice that all stress components are discontinuous along the beam axis. Moreover, the matrix $\mathbf{H}_{\sigma\sigma}$ (see (4.13) and (4.6)) is invertible. Therefore, it is possible to statically condense the stress variables out at the element level. This leads to a displacement-based-like formulation of the problem, thus significantly reducing the dimension of the global stiffness matrix and improving the FE algorithm efficiency.

4.4 Numerical examples

The goal of this section is to illustrate the capability of the beam model and FE introduced so far. Accordingly, we consider the problems listed below.

1. Homogeneous square cross-section beam, depicted in Figure 4.4.
2. Homogeneous, rectangular, and slim cross-section beam, depicted in Figure 4.10.
3. Non-homogeneous square cross-section beam, depicted in Figure 4.13.
4. Homogeneous L-shape cross-section beam, depicted in Figure 4.15.

We introduce the relative error definition for a generic variable γ :

$$e_{\gamma rel} := \frac{|\gamma - \gamma^{ref}|}{|\gamma^{ref}|} \quad (4.33)$$

where γ^{ref} is the reference solution, to be specified for each problem under investigation.

FE solutions considered in this section are evaluated through numerical-calculus functions implemented in MATLAB software, unless specified.

4.4.1 Homogeneous square cross-section beam

We consider the homogeneous beam with a square cross-section depicted in Figure 4.4 and we discuss the following aspects.

1. Displacement error and convergence of displacement solution.
2. Stress error.
3. Asymptotic behaviour.

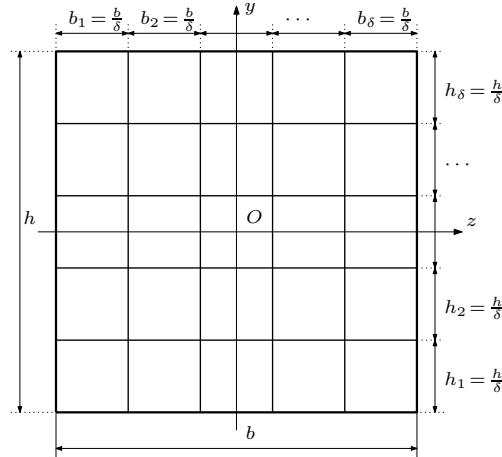


Figure 4.4: Homogeneous cross section: geometry and mesh definition (in the considered example $h = b = 1\text{mm}$, δ variable, $E = 10^5\text{MPa}$, and $\nu = 0.25$).

We recall that, in FE derivation, the beam is assumed to be clamped at the initial cross-section ($\partial\Omega_s = A_0$; $\bar{\mathbf{s}} = \mathbf{0}$); moreover, we set $\bar{l} = 10\text{mm}$, vanishing volume load ($\mathbf{f} = \mathbf{0}$), and a distributed shear load applied to the final cross section A_l ($\mathbf{t}|_{A_l} = [0, -1, 0]^T\text{MPa}$). In Figure 4.4, we define

the parameter δ that defines both the cross-section and the axial discretizations where the length of the k^{th} axis FE is defined as $l_k := \bar{l} / (10 \cdot \delta)$.

In the following, the acronym MB FE (Mixed Beam Finite Element) denotes the beam model FE discretization of Equation (4.30).

4.4.1.1 Displacement error

We consider the y -oriented displacement component s_v (see Definition (4.1)) and we evaluate its mean value $\bar{v}(\bar{l})$ on the final cross section A_l :

$$\bar{v}(\bar{l}) := \frac{\int_{A_l} \mathbf{r}_v^T \hat{\mathbf{v}}|_{x=\bar{l}} dydz}{\int_{A_l} dydz} \quad (4.34)$$

In order to discuss the displacement solution of the MB FE, we compare the solutions of the models listed in the following.

- The analytical solution of Euler-Bernoulli beam,
- The analytical solution of Timoshenko beam,
- The numerical solution of the MB FE evaluated considering two cases:
 - 1 fiber cross-section (i.e. $\delta = 1$),
 - 25 fiber cross-section (i.e. $\delta = 5$).
- 3D numerical solutions obtained using the software ABAQUS and with 3D trilinear bricks. The following uniform meshes are employed.
 - A uniform mesh of $5 \times 5 \times 50$ elements.
 - A uniform mesh of $10 \times 10 \times 100$ elements.
 - A fine and uniform mesh of $50 \times 50 \times 500$ elements. This overkilled solution is used as the reference solution s_v^{ref} .

In Table 4.3 we report the vertical-displacement mean-value $\bar{v}(\bar{l})$ for the considered beam models and their relative errors. We notice that all the models, even the two simplest ones (i.e.,

Beam model	$\bar{v}(10)$ mm	$e_{v\,rel}$
Euler-Bernoulli	$-4.000000 \cdot 10^{-2}$	$3.222 \cdot 10^{-3}$
Timoshenko	$-4.030000 \cdot 10^{-2}$	$4.254 \cdot 10^{-3}$
MB FE 1 fiber ($\delta = 1$)	$-4.022380 \cdot 10^{-2}$	$2.355 \cdot 10^{-3}$
MB FE 25 fiber ($\delta = 5$)	$-4.012917 \cdot 10^{-2}$	$0.003 \cdot 10^{-3}$
3D solution (mesh $5 \times 5 \times 50$)	$-4.175198 \cdot 10^{-2}$	$40.437 \cdot 10^{-3}$
3D solution (mesh $10 \times 10 \times 100$)	$-4.051178 \cdot 10^{-2}$	$9.531 \cdot 10^{-3}$
3D solution (v^{ref})	$-4.012929 \cdot 10^{-2}$	-

Table 4.3: Mean value of final cross-section displacement $\bar{v}(10)$ and the corresponding relative error for a cantilever ($\bar{l} = 10\text{mm}$, $b = h = 1\text{mm}$) evaluated using different beam models.

the Euler-Bernoulli and the Timoshenko models) give a relative error below 5‰. Furthermore, as expected, MB FE 25 fiber model provides the best solution, with a relative error close to 10^{-6} , negligible in most practical applications. In addition, despite the coarse discretization in the modelling procedure, the MB FE 1 fiber relative error is of the order of 2‰, better than both Euler-Bernoulli and Timoshenko beams. We also notice that we need $\sim 4 \cdot 10^6$ DOFs to compute

the displacements of the 3D overkilled solution, whereas we need $\sim 2 \cdot 10^4$ DOFs (plus $\sim 1.5 \cdot 10^3$ DOFs condensed at element level) to compute both displacements and stresses of the MB FE 25 fiber solution. In addition, the 3D solution obtained using the mesh $5 \times 5 \times 50$ (resp.: $10 \times 10 \times 100$), leads to $\sim 5.5 \cdot 10^3$ (resp.: $\sim 3.6 \cdot 10^4$) DOFs.

In Figure 4.5 we plot the relative error $e_{v,rel}$ as function of the element size $1/\delta$. It is worth

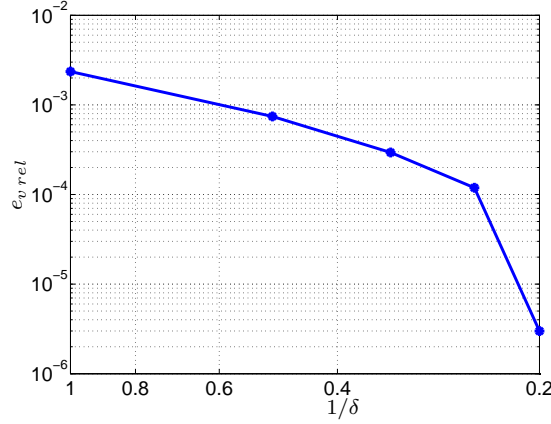


Figure 4.5: Relative error $e_{v,rel}$ plotted as function of the element size $1/\delta$.

observing the monotonic behaviour and the high speed convergence.

4.4.1.2 Stress error

We focus our attention to the shear components τ_{xy} and τ_{xz} since they have non-trivial distributions. In the following, the numerical results refer to the 25 fiber discretization.

Figures 4.6(a) and 4.6(b) report the shear axial coefficient functions $\hat{\tau}_{xy}$ and $\hat{\tau}_{xz}$ respectively. We remark that they show damped oscillations near the initial and final cross sections, while they are approximately constant otherwise. We notice that this numerical behaviour is consistent with the ODEs homogeneous solutions discussed in Section 4.2.4.

Moreover, the oscillations rapidly decay in an axial region whose length is of the order of magnitude of the cross-section edge, in accordance with the solution provided by the Saint-Venant principle.

Figures 4.7(a) and 4.7(b) report the cross-section distribution of shear components $\tau_{xy}(5, y, z)$ and $\tau_{xz}(5, y, z)$ respectively. We consider the cross section at $x = 5\text{mm}$ in order to exclude boundary effects. It is worth noticing that the cross-section shear component τ_{xy} has a parabolic distribution along y . Moreover, τ_{xy} is not constant along z , and the shear component τ_{xz} displays a non vanishing distribution in the cross section. These latter results provide a shear stress evaluation which is better than the one given by the simplified Jourawsky theory (e.g. Hjelmstad (2005)), usually adopted in connection with classical beam models.

Figures 4.7(c) and 4.7(d) report the cross-section error distributions $|\tau_{xy}(5, y, z) - \tau_{xy}^{ref}(5, y, z)|$ and $|\tau_{xz}(5, y, z) - \tau_{xz}^{ref}(5, y, z)|$, where $\tau_{xy}^{ref}(5, y, z)$ and $\tau_{xz}^{ref}(5, y, z)$ are reference solutions obtained using the results detailed in Timoshenko and Goodier (1951)[Chap. 12]. It is interesting to note that the numerical solution appears to be generally accurate. However, the error is higher close to the cross section edges.

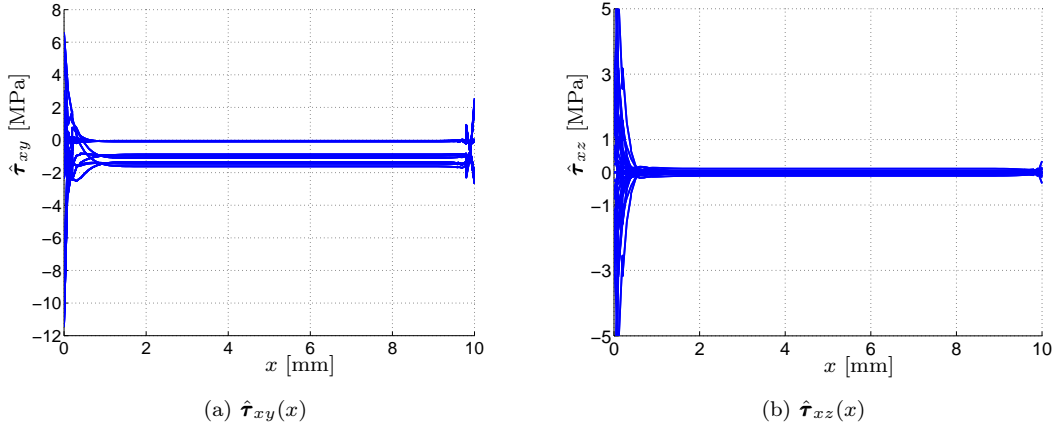


Figure 4.6: Shear axial coefficient functions $\hat{\tau}_{xy}(x)$ and $\hat{\tau}_{xz}(x)$ for the case of homogeneous and square cross section.

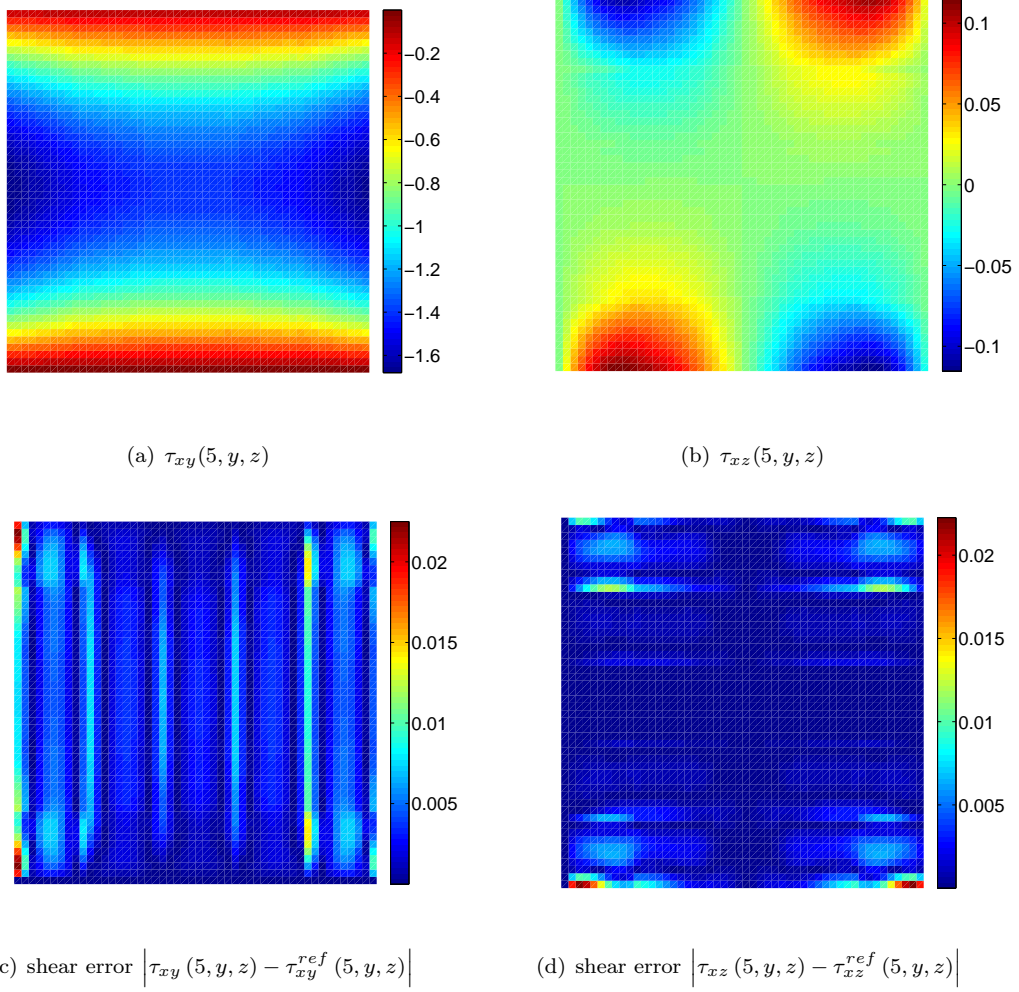


Figure 4.7: Shear cross-section distributions (4.7(a) and 4.7(b)) and cross-section error distributions (4.7(c) and 4.7(d)) for the case of homogeneous and square cross section.

4.4.1.3 Asymptotic analysis

In this sub-section, we investigate the beam model behaviour as the cross-section size tends to zero. It can be shown that the 3D beam solution converges to the EB solution, after a suitable scaling of the loads (see Ciarlet (1997), for instance). In this section we numerically verify that, decreasing the cross-section size, the MB FE solution converges to the EB solution, thus ensuring the asymptotic consistency of the proposed beam model.

We consider a beam with length and boundary conditions introduced in Section 4.4.1, and using a single square fiber to discretize the cross section. We use uniform meshes along the beam axis, and different decreasing values of the cross section size h . We implement the MB FE using numerical functions available in MAPLE software. In particular, we exploit the capability of the software to use an arbitrary number of digits during numerical calculation. Since we are interested in the asymptotic behaviour, the EB beam solution $\bar{v}^{ref}(\bar{l})$ is assumed as reference solution.

In Figure 4.8 we plot the relative error $e_{v,rel}$ evaluated at different ratios h/\bar{l} , for different axial meshes (4 and 50 elements, respectively), and for different machine precisions (16 and 30 digits, respectively). We notice that bad solutions are computed when using 16 digits and for very small

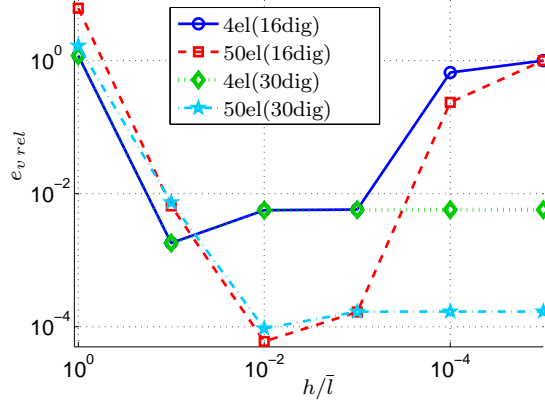


Figure 4.8: Relative asymptotic error.

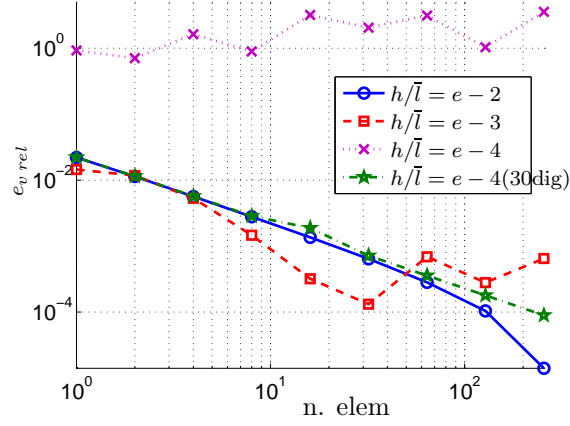
ratios h/\bar{l} , independently of the number of elements. However, satisfactory results are obtained for slendernesses of practical engineering interest. On the contrary, raising to 30 digits, the computed solutions display the correct behaviour. We remark that the plateau regions for 4el(30dig) and 50el(30dig) in Figure 4.8 correspond to the error due to the axial discretization, which dominates the total error in the asymptotic regime ($h/\bar{l} \ll 1$).

In Figure 4.9 we show the relative error of the single fiber MB FE, considering different ratios h/\bar{l} and varying the number of elements in the axial direction. The plot confirms the convergence of the solution, independently of the ratio h/\bar{l} when 30 digits are employed. As already noticed, a degeneracy in the convergence behaviour is experienced for very small h/\bar{l} and 16 digit precision.

4.4.1.4 Computational costs

In this subsection we give some information about the computational performance of the proposed method, comparing the numerical costs with the costs of a 3D displacement based analysis of the homogeneous square cross-section beam.

The time elapsed to compute the solutions is not a fair criterion due to the use of different softwares and machines. Instead, in Table 4.4 we provide some information that may be used to compare the different approaches. We notice that, in all the considered cases, the global stiffness

Figure 4.9: Relative error e_{vrel} plotted as function of the number of elements for different ratios h/\bar{l}

Model	e_{vrel}	# DOFs	# entries $\neq 0$	band-width	# flops
MB FE 1 fiber ($\delta = 1$)	$2.355 \cdot 10^{-3}$	$1.60 \cdot 10^2$	$7.17 \cdot 10^3$	$3.30 \cdot 10^1$	$8.71 \cdot 10^4$
MB FE 25 fiber ($\delta = 5$)	$0.003 \cdot 10^{-3}$	$2.00 \cdot 10^4$	$2.37 \cdot 10^7$	$1.60 \cdot 10^3$	$2.57 \cdot 10^{10}$
3D sol. ($5 \times 5 \times 50$)	$40.437 \cdot 10^{-3}$	$5.40 \cdot 10^3$	$4.37 \cdot 10^5$	$4.33 \cdot 10^2$	$5.05 \cdot 10^8$
3D sol. ($10 \times 10 \times 100$)	$9.531 \cdot 10^{-3}$	$3.63 \cdot 10^4$	$2.94 \cdot 10^6$	$1.45 \cdot 10^3$	$3.83 \cdot 10^{10}$
3D sol. ($50 \times 50 \times 500$)	-	$3.90 \cdot 10^6$	$3.16 \cdot 10^8$	$3.12 \cdot 10^4$	$1.90 \cdot 10^{15}$

Table 4.4: Final cross-section displacement relative error, number of DOFs used in the analysis (# DOFs), number of global stiffness-matrix entries different from zero (# entries $\neq 0$), band width of the global stiffness matrix (band-width), and estimation of the number of flops necessary to factorize the global stiffness matrix (# flops) for a cantilever ($\bar{l} = 10\text{mm}$, $b = h = 1\text{mm}$) evaluated using different beam models.

matrices governing the problem will be symmetric, sparse, and with a band structure.

The displacement relative error e_{vrel} is the same as reported in Table 4.3 and it provides information about the solution accuracy. The estimation of the number of DOFs (# DOFs) corresponds to the size of the global stiffness matrix. In particular, for the 1- and 5- fiber models, # DOFs does not take into account the number of variables condensed out at the element level, since negligible with respect to number of global DOFs (e.g. in the 5 fibre model $\sim 1.5 \cdot 10^3$ DOFs are condensed on each element). The number of non-vanishing entries in the global stiffness matrices (# entries $\neq 0$) is strictly related to the memory usage during computation. The fourth column of Table 4.4 reports an estimation of the band width. The fifth column reports an estimation of the number of flops necessary to LU-factorize the global stiffness matrix (# flops), under the following assumptions: (i) # DOFs \gg band-width and (ii) the computational cost of both the assembling procedure and the post-processing are negligible. As a consequence, # flops is evaluated through the following equation (see Quarteroni et al., 2007):

$$\# \text{ flops} = \frac{\# \text{ DOFs} \cdot (\text{band-width})^2}{2} \quad (4.35)$$

We highlight that the MB FE 25 fiber and the 3D solution (mesh $10 \times 10 \times 100$) require comparable # flops. Nevertheless, the former model provides a solution with a relative error that is 3 order of magnitude smaller than the latter. The obtained results, even if non exhaustive, lead us to conclude that the proposed method has interesting numerical performances with respect to the standard 3D analysis.

4.4.1.5 Conclusions on the beam model and the corresponding FE scheme

Looking at all the analyses performed in this section, we may remark what follows.

- As illustrated in Subsection 4.4.1.1, the MB and the corresponding FE scheme can capture the real displacement better than the most popular beam models (EB and Timoshenko models).
- As illustrated in Subsection 4.4.1.2, the proposed beam model has a significant accuracy in the stress description.
- As illustrated in Subsection 4.4.1.3, the asymptotic behaviour, for reasonable ratios h/\bar{l} , is correct. Nevertheless, we note that the MB FE scheme may exhibits troubles for extremely small ratios h/\bar{l} .

As a consequence, we conclude that the proposed approach is a competitive alternative to other popular beam models.

4.4.2 Rectangular slim cross-section

In this section, nevertheless, we consider only the bending of a beam with the slim cross-section represented in Figure 4.10 . The beam analytical solution is available in literature (see Timoshenko and Goodier, 1951).

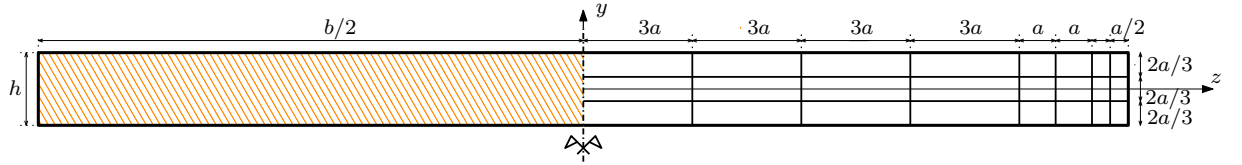


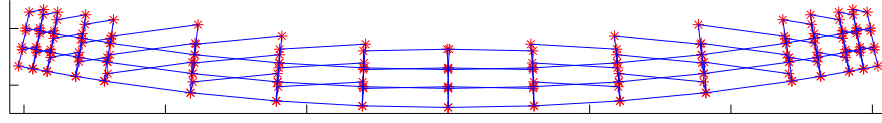
Figure 4.10: Slim cross section: geometry and mesh definition.

The beam geometrical dimensions are $h = 0.2\text{mm}$, $b = 3\text{mm}$, and $\bar{l} = 20\text{mm}$ whereas $a = 0.1\text{mm}$. The beam is clamped in the initial cross section A_0 (i.e., $\bar{\mathbf{s}} = \mathbf{0}$, as already specified in Section 4.2.2) and loaded in the final cross section A_l by a distributed shear load (i.e., $\mathbf{f} = \mathbf{0}$ and $\mathbf{t} = \{0, -1, 0\}^T \text{MPa}$). The material parameters are: $E = 10^5 \text{MPa}$ and $\nu = 0.25$. Finally, the axis discretization is done through a regular mesh of 10 elements whereas the cross-section discretization is done through 48 non regular rectangular fibres, as illustrated in Figure 4.10.

Figure 4.11 plots the deformed cross-section at $x = 10\text{mm}$ (to highlight deformations, displacements are amplified of a factor 10).

It is interesting to notice the following statements.

- Discontinuities between fibres in transversal displacement fields s_v and s_w are evident. They are the consequence of the assumption of Table 4.1 where the displacement cross-section shape functions are assumed to be discontinuous between fibres.
- The deformed section is concave, whereas the deformed beam axis is convex. This phenomenon is known in literature as *anticlastic bending* and it becomes more and more significant for higher values of the ratio b/h . It is worth noting that this phenomena is usually ignored in structural design and analysis. Nevertheless, in practical applications, it can be of interest for the induced deformations (see Reference Kushnir et al. (1993)) but also for the induced stress. We notice also that the most of the beam models adopted in engineering practice are not able to catch it.

Figure 4.11: Transversal cross-section displacements (amplification factor 10) evaluated at $x = 10\text{mm}$

Figures 4.12(a) and 4.12(c) plot the cross-section shear distributions $\tau_{xy}(10, y, z)$ and $\tau_{xz}(10, y, z)$ respectively.

Since the cross-section, as well as the boundary load \mathbf{t} and the assigned boundary displacement $\bar{\mathbf{s}}$ are symmetric respect to both the y - and z - axis, it is not surprising to obtain symmetric stress distributions. In particular, τ_{xy} has an even distribution respect to both the cross-section axis, i.e. $\tau_{xy}(10, y, z) = \tau_{xy}(10, -y, z) = \tau_{xy}(10, y, -z)$, whereas τ_{xz} has an odd distribution respect to both the cross-section axis, i.e. $\tau_{xz}(10, y, z) = -\tau_{xz}(10, -y, z) = -\tau_{xz}(10, y, -z)$. For this reason, Figures 4.12 plot distributions only for $y, z > 0$ in a dimensionless coordinate system.

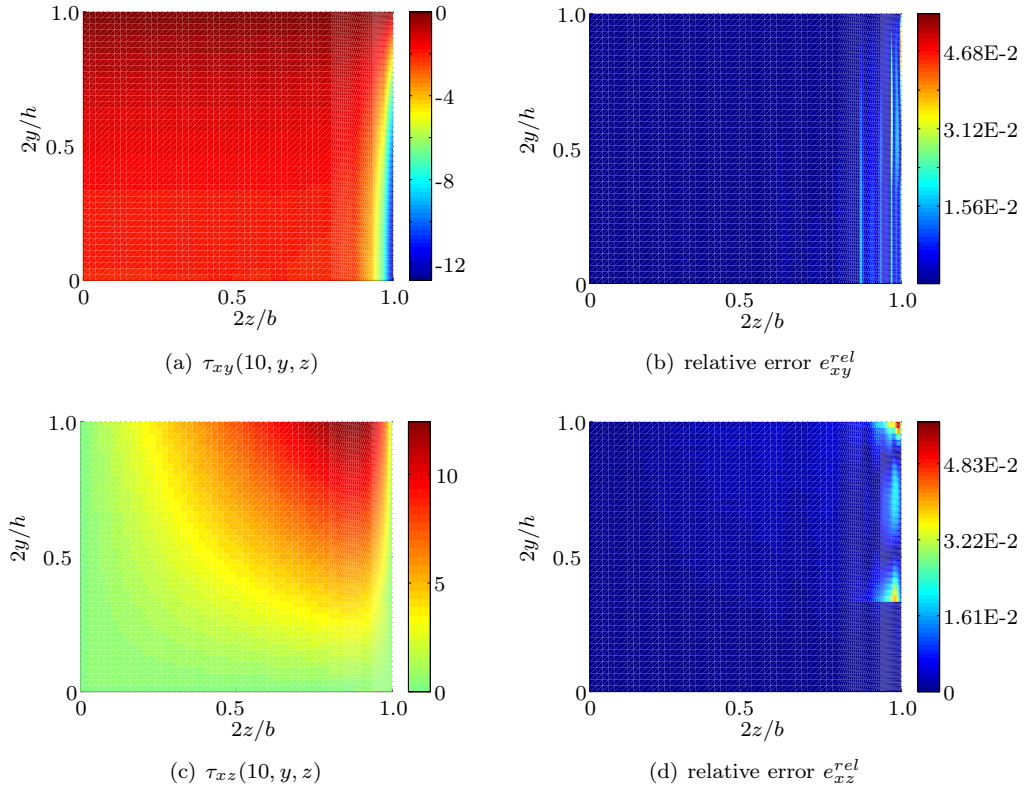


Figure 4.12: Shear components evaluated at $x = 10\text{mm}$ for the case of homogeneous, slim cross-section: cross-section distributions 4.12(a) and 4.12(c), cross-section relative error distributions 4.12(b) and 4.12(d) (results plotted for $y, z > 0$).

The reference distributions $\tau_{xy}^{ref}(10, y, z)$ and $\tau_{xz}^{ref}(10, y, z)$ are the analytical solutions of the

problem we are discussing. The analytical expression of the solution is illustrated in Reference Timoshenko and Goodier (1951)[Chap. 12]. Specifically, shear distributions $\tau_{xy}^{ref}(10, y, z)$ and $\tau_{xz}^{ref}(10, y, z)$ are expressed as Fourier series. In order to have a numerical evaluation of the solution, we truncate the series at a term negligible with respect to the machine precision.

Due to the cross-section's geometry with high ratio b/h , the shear component τ_{xz} becomes of the same order of magnitude of the other component τ_{xy} . Reference Timoshenko and Goodier (1951) notice that the ratio $\max_{(y,z) \in A} (|\tau_{xy}^{ref}|) / \max_{(y,z) \in A} (|\tau_{xz}^{ref}|) \approx 1$ for the considered b/h ratio. From numerical results we obtain that $\max_{(y,z) \in A} (|\tau_{xy}|) / \max_{(y,z) \in A} (|\tau_{xz}|) = 1.03$, in agreement with the analytical solution.

The relative errors e_{xy}^{rel} and e_{xz}^{rel} are defined in Equation (4.36) and Figures 4.12(b) and 4.12(d) plot their distribution within the cross-section.

$$e_{xy}^{rel} = \frac{|\tau_{xy}(10, y, z) - \tau_{xy}^{ref}(10, y, z)|}{\max_{(y,z) \in A} (|\tau_{xy}^{ref}(10, y, z)|)}, \quad e_{xz}^{rel} = \frac{|\tau_{xz}(10, y, z) - \tau_{xz}^{ref}(10, y, z)|}{\max_{(y,z) \in A} (|\tau_{xz}^{ref}(10, y, z)|)} \quad (4.36)$$

We notice that the error is always less than the 5%, and high relative error values occur close to the cross-section edges. On the contrary, the magnitude of the relative error is lower than the 1% on the rest of the cross-section. According our results, we can argue that the numerical solution is reasonably accurate, despite the relatively coarse cross-section fibre discretisation.

4.4.3 Non homogeneous cross-section beam (soft core beam)

In this subsection we consider a beam with the non-homogeneous square cross-section depicted in Figure 4.13, and modeled through 25 equal fibers.

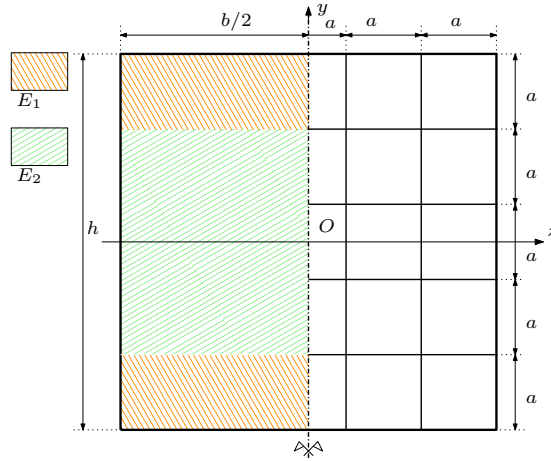
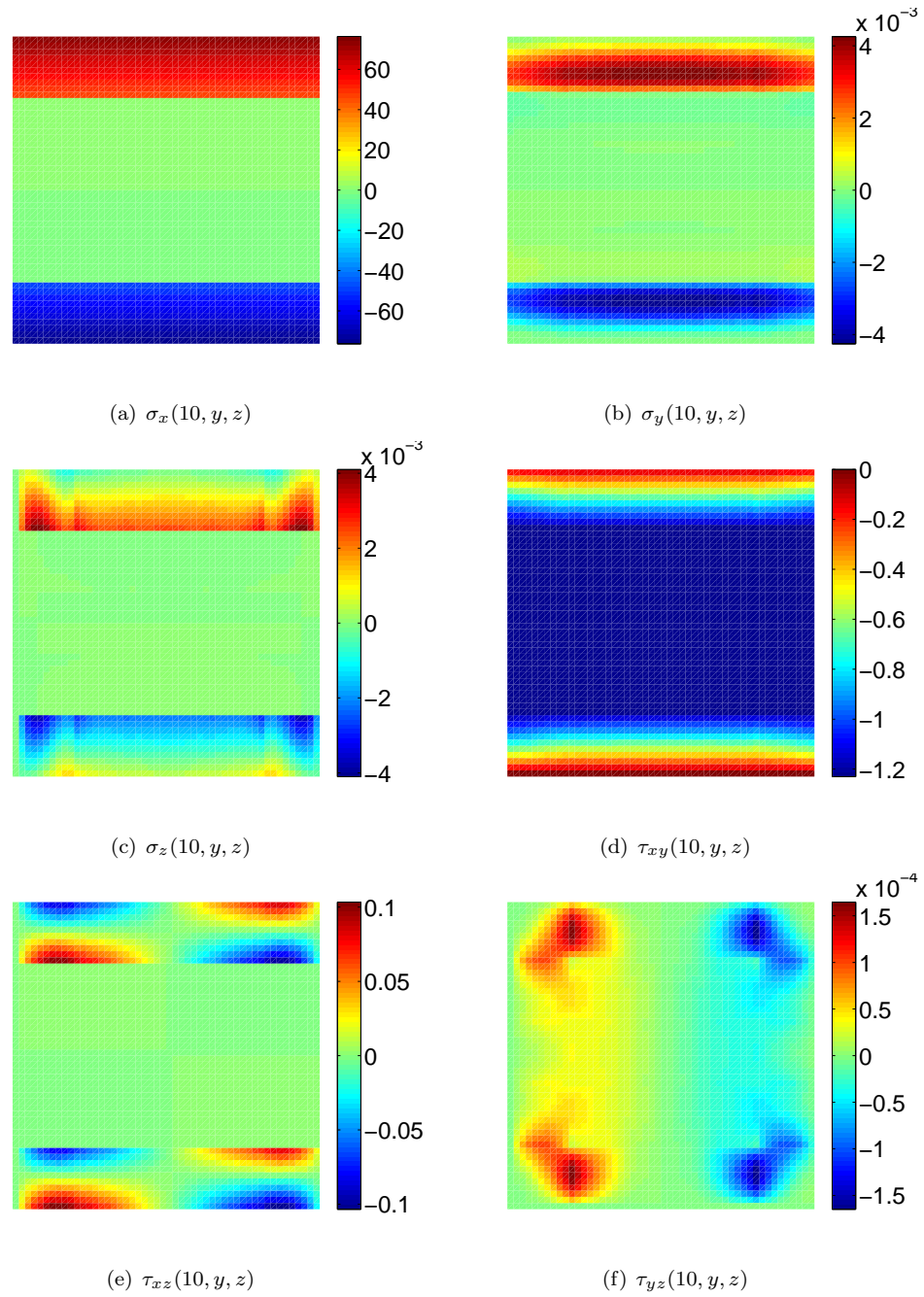


Figure 4.13: Non-homogeneous cross section: geometry and mesh definition (in the considered example $h = b = 1\text{mm}$, $a = 0.2\text{mm}$, $E_1 = 10^5\text{MPa}$, $E_2 = 10^3\text{MPa}$, and $\nu = 0.25$).

We assume the boundary conditions of the example in Section 4.4.1. Furthermore, we set $\bar{l} = 20\text{mm}$, $E_1 = 10^5\text{MPa}$, $E_2 = 10^3\text{MPa}$, and $\nu = 0.25$ everywhere in the cross section. Along the beam axis we use a non-uniform 8 element meshes, whose nodal coordinates are collected in the following vector: $[0; 1; 2; 3; 10; 17; 18; 19; 20]$. We plot the stress distribution in the cross section $x = 10\text{mm}$. The numerical results are reported in Figure 4.14.

Consistently with the Saint-Venant principle, the stress components σ_{yy} , σ_{zz} and τ_{yz} are negligible. Moreover, due to the large ratio between the two Young's moduli, stress distributions within the core appear always extremely regular and flat.

Figure 4.14: Stress distributions evaluated at $x = 10\text{mm}$ for the non homogeneous case.

In this example the non uniform distribution of shear component τ_{xy} along z -direction is less evident than in the case of homogeneous beam. The ratio between the maximum values of the shears τ_{xy} and τ_{xz} , is close to 10, which confirms, once again, that τ_{xz} should not be neglected. In order to validate the results, we compute a 3D numerical solution using the ABAQUS software and a homogeneous mesh of 40 brick elements. In Table 4.5 we report the minimum and the

	MB FE		ABAQUS	
	min	max	min	max
σ_x	$-7.54 \cdot 10^1$	$7.54 \cdot 10^1$	$-7.55 \cdot 10^1$	$7.55 \cdot 10^1$
σ_y	$-5.73 \cdot 10^{-2}$	$5.73 \cdot 10^{-2}$	$-2.57 \cdot 10^{-1}$	$2.57 \cdot 10^{-1}$
σ_z	$-1.22 \cdot 10^{-1}$	$1.22 \cdot 10^{-1}$	$-3.36 \cdot 10^{-1}$	$3.39 \cdot 10^{-1}$
τ_{xy}	$-1.23 \cdot 10^0$	$0.00 \cdot 10^0$	$-1.23 \cdot 10^0$	$-8.01 \cdot 10^{-2}$
τ_{xz}	$-1.25 \cdot 10^{-1}$	$1.25 \cdot 10^{-1}$	$-9.62 \cdot 10^{-2}$	$9.62 \cdot 10^{-1}$
τ_{yz}	$-7.27 \cdot 10^{-3}$	$7.27 \cdot 10^{-3}$	$-1.02 \cdot 10^{-1}$	$1.02 \cdot 10^{-1}$

Table 4.5: Minimum and maximum value of stress components distributions evaluated on the cross-section $x = 10\text{mm}$ for the non-homogeneous case, evaluated with different methods.

maximum values of the cross-section stress distribution evaluated on the cross-section $x = 10\text{mm}$. From the comparison of the two methods it is possible to appreciate the substantial agreement of the results. We notice that the high value of the σ_y , σ_z , and τ_{yz} in ABAQUS min and max evaluation depends on some localized instabilities that occur in numerical evaluation of stress.

4.4.4 L-shape cross-section beam

We consider the cross-section geometry and fiber distribution reported in Figure 4.15.

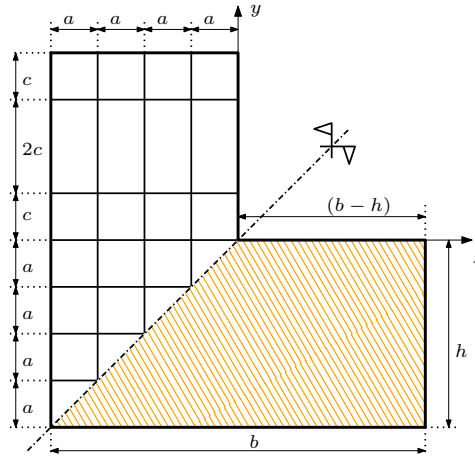
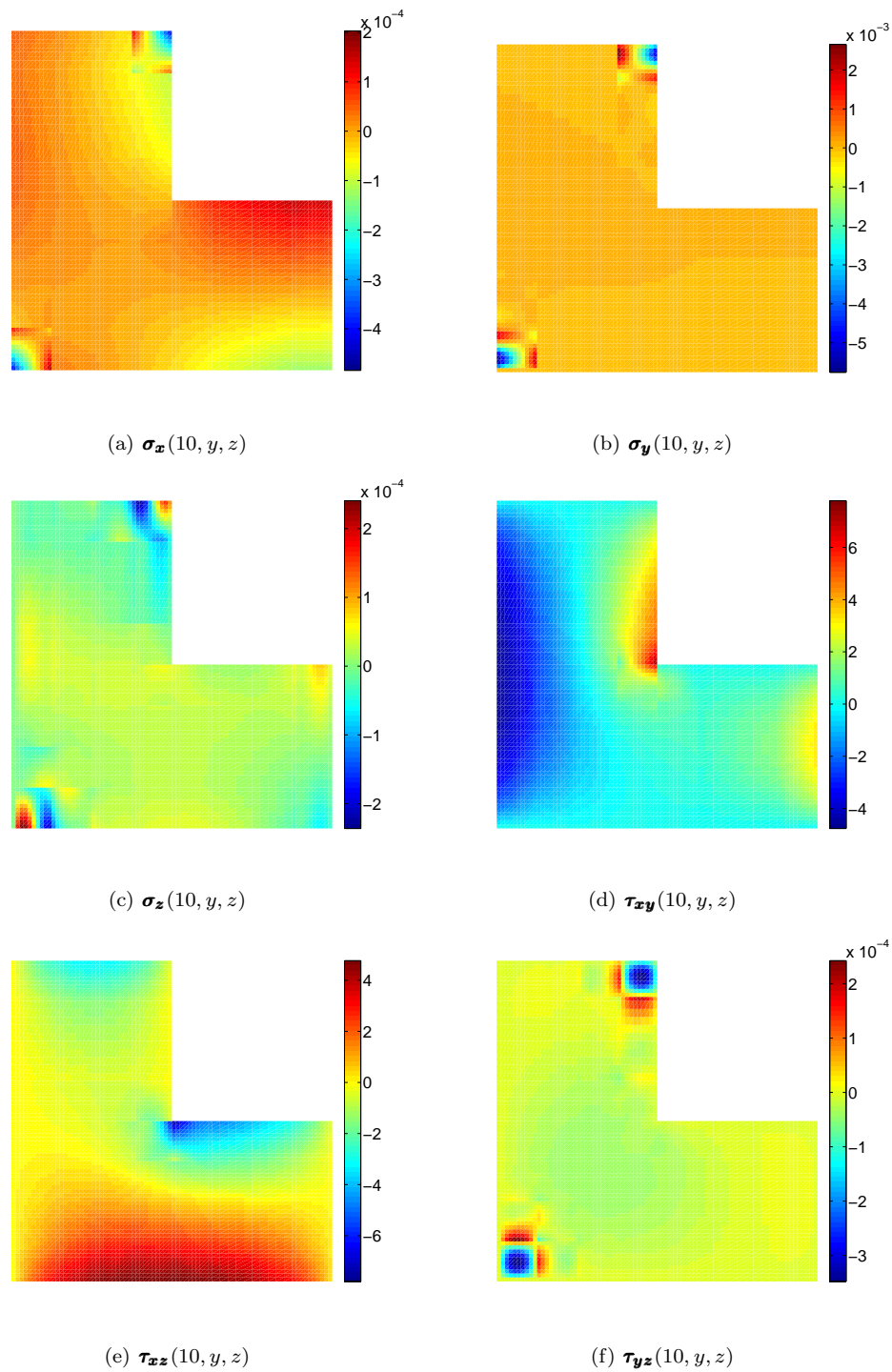


Figure 4.15: L-shape cross section: geometry and mesh definition (in the considered example $b = 1\text{mm}$, $h = 0.5\text{mm}$, $a = c = 0.125\text{mm}$, $E = 10^5\text{MPa}$, and $\nu = 0.25$).

We assume the beam length, the axial mesh, and the displacement constraint of the example in Section 4.4.3, while the material parameters are set as $E = 10^5\text{MPa}$ and $\nu = 0.25$. We load the beam with a torsion moment equal to 1Nmm in A_l , imposed through a couple of opposite unit forces $[0, 0, 1]\text{N}$ and $[0, 0, -1]\text{N}$ applied in vertices $(20, -0.5; -0.5)$ and $(20, 0; 0.5)$ respectively. The stress distributions at $x = 10\text{mm}$ are reported in Figure 4.16.

It is interesting to observe that, as expected, the magnitude of σ_x , σ_y , σ_z and τ_{yz} is negligible with respect to the magnitude of the shear components τ_{xy} and τ_{xz} . Moreover, considering the

Figure 4.16: Stress distributions evaluated at $x = 10\text{mm}$ for the L-shape cross section.

cross-section symmetry highlighted in Figure 4.15, the τ_{xy} distribution is anti-symmetric respect to the τ_{xy} distribution. Finally, a small stress concentration of σ_x , σ_y , σ_z and τ_{yz} can be appreciated close to the section vertices where concentrated forces are applied.

In order to validate the results, we compute a 3D numerical solution using the ABAQUS software and a homogeneous mesh of 40 brick elements. In Table 4.6 we report the minimum

	MB FE		ABAQUS	
	min	max	min	max
σ_x	$-3.61 \cdot 10^{-3}$	$1.74 \cdot 10^{-3}$	$-1.65 \cdot 10^{-9}$	$1.20 \cdot 10^{-9}$
σ_y	$-2.68 \cdot 10^{-2}$	$5.78 \cdot 10^{-2}$	$-1.51 \cdot 10^{-11}$	$1.41 \cdot 10^{-11}$
σ_z	$-7.50 \cdot 10^{-3}$	$7.19 \cdot 10^{-3}$	$-2.12 \cdot 10^{-11}$	$1.49 \cdot 10^{-11}$
τ_{xy}	$-9.54 \cdot 10^0$	$1.56 \cdot 10^1$	$-9.55 \cdot 10^0$	$1.66 \cdot 10^1$
τ_{xz}	$-1.56 \cdot 10^1$	$9.54 \cdot 10^0$	$-1.66 \cdot 10^1$	$9.55 \cdot 10^0$
τ_{yz}	$-2.47 \cdot 10^{-3}$	$7.29 \cdot 10^{-3}$	$-1.24 \cdot 10^{-11}$	$8.12 \cdot 10^{-12}$

Table 4.6: Minimum and maximum value of stress components distributions evaluated on the cross-section $x = 10\text{mm}$ for the L-shape case, evaluated with different methods.

and the maximum values of the cross-section stress distribution evaluated on the cross-section $x = 10\text{mm}$. From the comparison of the two method results it is possible to appreciate the substantial agreement of the results. We notice a small difference between the maximum values of τ_{xy} and τ_{xz} that occurs in the reflex angle of the cross-section where stress concentration occurs.

Chapter 5

Non-constant Cross-section Beam-model

In this chapter we are going to consider a 2D elastic problem, i.e. with respect to the notation introduced in Chapter 2, we assume $n = 2$. Nevertheless, differently from the Chapter 3, we are going to consider a non rectangular domain, i.e. a 2D beam with non-constant cross-section. Figure 3.1 represents the domain, the adopted Cartesian coordinate system, the initial and the final cross sections A_0 and A_l respectively, and the lateral surface $L := h_l \cup h_u$ for the case we are considering. The problem we are going to investigate presents some peculiarities with respect to the formulation intrduced in Chapter 2. As a consequence we will introduce a specific problem formulation.

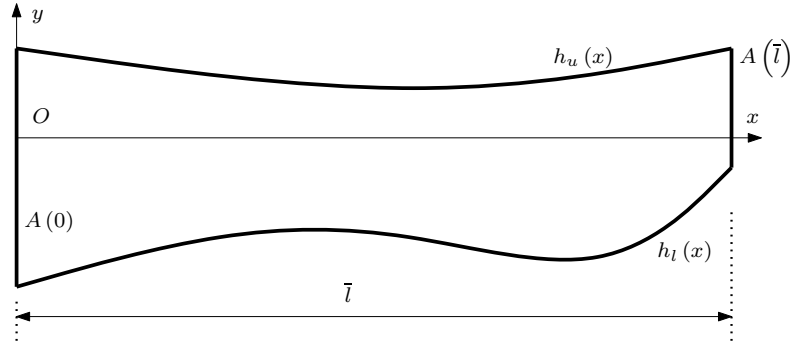


Figure 5.1: 2D beam geometry, coordinate system, dimensions and adopted notations.

Section 5.1 provides a brief literature review on existing non- constant beam models and an overview on the specific problem we are going to discuss in this chapter. Section 5.2 introduces a specialized problem formulation. Section 5.3 formulates the non-constant beam model. Section 5.4 formulates the corresponding FE and, finally, Section 5.5 provides some numerical examples.

5.1 Engineering motivations

Practitioners extensively use beams with **non-constant cross-section** since they allow to optimize the beam behaviour with respect to peculiar problems. As an example, non-constant cross-section beams allow to obtain the maximum resistance to the loads using the minimum amount of material. Laminated wood structures, cranes, and arc-shaped beams are applications

in which displacements and stresses induced by statical loads are the main problems to investigate. Windmill turbine and propeller blades are more complex applications of non-constant cross-section beams since centrifugal force induced by rotation and vibrations represent additional aspects to investigate.

Anyhow, the accuracy of non-constant cross-section beam models is a particularly crucial aspect for engineers, in order to perform an effective design. Unfortunately, non-constant cross-section beam models rarely satisfy the requests of practitioners who therefore must choose between the use of heavy approximations or the use of more expensive models, like 3D solids Finite Element (FE) models.

A simple class of non-constant cross-section beams are the so-called **tapered beams** in which the cross-section dimension varies linearly with respect to the axis coordinate. Since the twentieth century, researchers have been proposing both analytical and numerical tapered-beam models that are currently available in literature.

The simplest tapered-beam models simply modify the coefficients of the Euler-Bernoulli (EB) or Timoshenko beam models in order to take into account the variation with respect to the axial coordinate of the cross-section geometrical properties (area and inertia). Significant examples of these models are presented in (Banerjee and Williams, 1985) and (Banerjee and Williams, 1986) whereas, among the others, we cite (Vinod et al., 2007) as an example of numerical model application. Unfortunately, it is well-known since the 60ies (see (Boley, 1963)) that this approach is not adequate in a large class of applications, as recently illustrated in (Hodges et al., 2010). In fact, the error in displacement and stress evaluations increases with the taper slope, quickly overcoming the 10%. In particular, Hodges et al. (2010) isolate the error source in the violation of boundary equilibrium on the lateral surface during the beam model formulation.

Moreover, in beams without axis symmetry, the relative position of cross-section barycentre and load application-point varies along the beam axis and an axial load produces a bending moment. In the same context, also the relative position between shear centre and load application-point varies along the beam axis and a shear load produces a torque moment. On the other hand, the EB and the Timoshenko beams model *independently* the axial-compression, the shear-bending, and the torque problems. As a consequence, the simplest tapered-beam models are not adequate for non symmetric beams due to the absence of **coupling terms** between axial, transverse and rotation equilibrium equations. In order to overcome this problem, Li and Li (2002) consider in their model the coupling of axial-compression and shear-bending problems whereas Kitipornchai and Trahair (1975) investigate the coupling of shear bending and torque problems in the case of mono-symmetric cross-sections. Obviously, as highlighted in (Hodges et al., 2010), this modelling choices could open new problems related to the evaluation of the coupling terms that could be not trivial, in particular for complex cross-section geometries.

Restricting our attention to 2D bodies, Hodges et al. (2008) develop a displacement-based 2D tapered beam-model. The authors use the variational-asymptotic method for derivation and they consider the slope of taper as beam parameter, used to enforce the lateral surface equilibrium. Starting from this model, Hodges et al. (2010) provide formulae to recover stresses and strains and illustrate the model capability that appear to be extremely accurate. Unfortunately, the authors do not consider in their models the coupling terms and do not provide information about generalization of their model, for example to non-symmetric or generic non-constant cross-section beams.

5.2 Problem formulation

With respect to the definitions provided in Chapter 2, we modify the definition of the cross-section as follows:

$$A(x) := \{y \in [h_l(x), h_u(x)]\} \quad (5.1)$$

where h_l and $h_u : l \rightarrow \mathbb{R}$ are the cross-section lower- and upper- limits, respectively. In cross-section definition (5.1) we highlight the dependence of the cross-section on the axial coordinate x . We assume that the lower- and upper- limits are sufficiently smooth functions, defined so that $h_l(x) < h_u(x) \forall x \in l$ and $|\frac{d}{dx}h_l(x)|, |\frac{d}{dx}h_u(x)| < \infty$. As usual in beam modelling, $\bar{l} \gg \bar{A}(x) \forall x \in l$, where $\bar{A}(x)$ is the cross-section height, defined as $\bar{A}(x) := h_u(x) - h_l(x)$.

We define the problem domain as:

$$\Omega := l \times A(x) \quad (5.2)$$

Figure 5.1 represents the domain Ω , the adopted Cartesian coordinate system, the lower and upper limits $y = h_l(x)$ and $y = h_u(x)$, and the initial and final cross-sections $A(0)$ and $A(\bar{l})$, respectively. The lateral surface is defined as $L := h_l \cup h_u$.

In the following, we assume that the lower- and upper- limits belong to the loaded boundary, i.e. $h_u(x), h_l(x) \subset \partial\Omega_t$. Moreover, as usual in beam modelling, we assume that the lower- and upper- limits are unloaded, i.e. $\mathbf{t}|_{h_l \cup h_u} = \mathbf{0}$.

To enforce the boundary equilibrium we need to know the outward unit vectors on the lower- and upper- limits that result as follows:

$$\begin{aligned} \mathbf{n}|_{h_l}(x) &= \frac{1}{\sqrt{1 + (h'_l(x))^2}} \begin{Bmatrix} h'_l(x) \\ -1 \end{Bmatrix} \\ \mathbf{n}|_{h_u}(x) &= \frac{1}{\sqrt{1 + (h'_u(x))^2}} \begin{Bmatrix} -h'_u(x) \\ 1 \end{Bmatrix} \end{aligned} \quad (5.3)$$

where $(\cdot)'$ means the derivative with respect to the independent variable x . As a consequence, the boundary equilibrium on lateral surface $\boldsymbol{\sigma} \cdot \mathbf{n}|_{h_l \cup h_u} = \mathbf{0}$ could be expressed as follows:

$$\begin{bmatrix} \sigma_x & \tau \\ \tau & \sigma_y \end{bmatrix} \begin{Bmatrix} n_x \\ n_y \end{Bmatrix} = \begin{Bmatrix} 0 \\ 0 \end{Bmatrix} \Rightarrow \begin{cases} \sigma_x n_x + \tau n_y = 0 \\ \tau n_x + \sigma_y n_y = 0 \end{cases} \quad (5.4)$$

Manipulating Equation (5.4), we express τ and σ_y as function of σ_x . Using the outward unit vector \mathbf{n} definition (5.3), we obtain the following expressions for boundary equilibrium:

$$\tau = -\frac{n_x}{n_y}\sigma_x = h'\sigma_x; \quad \sigma_y = \frac{n_x^2}{n_y^2}\sigma_x = (h')^2\sigma_x \quad (5.5)$$

where h indicates both $h_l(x)$ and $h_u(x)$. We notice that, given the upper and lower surface definitions $y = h_l(x)$ and $y = h_u(x)$, σ_x could be seen as the independent variable that completely defines the stress state on the lateral surface. Moreover, as stated in (Hodges et al., 2008) and (Hodges et al., 2010), the unique parameter necessary to define the boundary equilibrium is the slope of the limit functions h'_l and h'_u .

5.3 Model derivation

In this section we develop the beam model through the dimensional reduction approach, described in Section 2.8.1. The same procedure is applied in Section 3.4 but, with respect to that section, in

this chapter we modify the definition of the approximated fields in order to satisfy the boundary equilibrium on lower- and upper- limits.

5.3.1 Cross-section approximation and notations

With respect to the notation introduced in Section 2.8.1, we introduce some additional hypothesis on cross-section shape functions useful to satisfy exactly the boundary equilibrium.

- The stress cross-section shape functions are Lagrange polynomials.
- The extremal cross-section points $y = h_l(x)$; $y = h_u(x)$ are interpolating nodes for the stresses cross-section shape functions.
- $\forall x \in l \quad \mathbf{r}_{\sigma_y}|_{h_l \cup h_u} = \mathbf{r}_\tau|_{h_l \cup h_u} = \mathbf{0}$

We highlight that, due to \mathbf{r}_γ definition and the assumptions listed so far, the stress cross-section shape functions implicitly depend also on x coordinate, since the interpolating node positions vary according to the lower- and upper- limits. As a consequence, some computational complications occur, but the model-derivation procedure illustrated in Auricchio et al. (2010) does not change.

Approximation definition (2.20) and the assumptions introduced so far lead to the following definition of partial derivatives.

$$\frac{\partial}{\partial x} \gamma = \frac{\partial}{\partial x} (\mathbf{r}_\gamma^T \hat{\gamma}) = \mathbf{r}_{\gamma,x}^T \hat{\gamma} + \mathbf{r}_\gamma^T \hat{\gamma}'; \quad \frac{\partial}{\partial y} \gamma = \frac{\partial}{\partial y} (\mathbf{r}_\gamma^T \hat{\gamma}) = \mathbf{r}_{\gamma,y}^T \hat{\gamma}$$

where $(\cdot)'$ indicates x derivative for $\hat{\gamma}$ whereas we use $(\cdot)_{,x}$ and $(\cdot)_{,y}$ to indicate respectively x - and y - partial derivatives for \mathbf{r}_γ .

Switching to an engineering notation, considering Equation (2.20) and introducing the boundary equilibrium as expressed in (5.5), we set:

$$\mathbf{s} = \begin{Bmatrix} s_u(x, y) \\ s_v(x, y) \end{Bmatrix} \approx \begin{bmatrix} \mathbf{r}_u^T & \mathbf{0} \\ \mathbf{0} & \mathbf{r}_v^T \end{bmatrix} \begin{Bmatrix} \hat{\mathbf{u}} \\ \hat{\mathbf{v}} \end{Bmatrix} = \mathbf{R}_s \hat{\mathbf{s}} \quad (5.6)$$

$$\boldsymbol{\sigma} = \begin{Bmatrix} \sigma_x(x, y) \\ \sigma_y(x, y) \\ \tau(x, y) \end{Bmatrix} \approx \begin{bmatrix} \mathbf{r}_{\sigma_x}^T & \mathbf{0} & \mathbf{0} \\ \mathbf{r}_{\sigma_x}^T \mathbf{T}^2 & \mathbf{r}_{\sigma_y}^T & \mathbf{0} \\ \mathbf{r}_{\sigma_x}^T \mathbf{T} & \mathbf{0} & \mathbf{r}_\tau^T \end{bmatrix} \begin{Bmatrix} \hat{\sigma}_x \\ \hat{\sigma}_y \\ \hat{\tau} \end{Bmatrix} = \mathbf{R}_\sigma \hat{\boldsymbol{\sigma}} \quad (5.7)$$

where \mathbf{T} is a diagonal matrix defined as follows:

$$T_{ii} := \begin{cases} 0 & \text{if } p_{\sigma_x i}|_{h_l} = p_{\sigma_x i}|_{h_u} = 0 \\ h'_0 & \text{if } p_{\sigma_x i}|_{h_l} \neq 0 \\ h'_n & \text{if } p_{\sigma_x i}|_{h_u} \neq 0 \end{cases} \quad (5.8)$$

Virtual fields are analogously defined as:

$$\delta \mathbf{s} = \mathbf{R}_s \delta \hat{\mathbf{s}}; \quad \delta \boldsymbol{\sigma} = \mathbf{R}_\sigma \delta \hat{\boldsymbol{\sigma}}$$

We highlight that the stress approximation so far introduced imposes the boundary equilibrium as essential condition, as required in S_0 and S_t functional spaces.

Coherently with the engineering notation just introduced, in Table 5.1 we re-define the differential operators and the outward unit vector scalar product.

The matrices \mathbf{E}_1 and \mathbf{E}_2 are defined as follows:

$$\mathbf{E}_1 = \begin{bmatrix} 1 & 0 & 0 \\ 0 & 0 & 1 \end{bmatrix}; \quad \mathbf{E}_2 = \begin{bmatrix} 0 & 0 & 1 \\ 0 & 1 & 0 \end{bmatrix}$$

Tensorial notation	Engineering notation
$\nabla \cdot \boldsymbol{\sigma}$	$\left(\frac{d}{dx} \mathbf{E}_1 + \frac{d}{dy} \mathbf{E}_2 \right) \mathbf{R}_\sigma \hat{\boldsymbol{\sigma}}$
$\boldsymbol{\sigma} \cdot \mathbf{n}$	$(n_x \mathbf{E}_1 + n_y \mathbf{E}_2) \mathbf{R}_\sigma \hat{\boldsymbol{\sigma}}$

Table 5.1: Tensor and engineering equivalent notations.

In Section 5.2, with \mathbf{D}^{-1} we denoted the fourth order elastic tensor while from now on, we use the same notation to indicate the corresponding square matrix obtained following engineering notation. Therefore, we have:

$$\mathbf{D}^{-1} = \frac{1}{E} \begin{bmatrix} 1 & -\nu & 0 \\ -\nu & 1 & 0 \\ 0 & 0 & 2(1+\nu) \end{bmatrix}$$

5.3.2 Model formulation

We use the notations (5.6) and (5.7) in Equation (2.13) and we assume $\bar{\mathbf{s}} = \mathbf{0}$. As a consequence, the HR functional stationariness (2.13) becomes:

$$\begin{aligned} \delta J_{HR} = & - \int_{\Omega} \delta \hat{\mathbf{s}}^T \mathbf{R}_s^T \left[\left(\frac{d}{dx} \mathbf{E}_1 + \frac{d}{dy} \mathbf{E}_2 \right) (\mathbf{R}_\sigma \hat{\boldsymbol{\sigma}}) \right] d\Omega \\ & - \int_{\Omega} \left[\left(\frac{d}{dx} \mathbf{E}_1 + \frac{d}{dy} \mathbf{E}_2 \right) (\mathbf{R}_\sigma \delta \hat{\boldsymbol{\sigma}}) \right]^T \mathbf{R}_s \hat{\mathbf{s}} d\Omega \\ & - \int_{\Omega} \delta \hat{\boldsymbol{\sigma}}^T \mathbf{R}_\sigma^T \mathbf{D}^{-1} \mathbf{R}_\sigma \hat{\boldsymbol{\sigma}} d\Omega - \int_{\Omega} \delta \hat{\mathbf{s}}^T \mathbf{R}_s^T \mathbf{f} d\Omega = 0 \end{aligned} \quad (5.9)$$

Expanding Equation (5.9), the weak formulation becomes:

$$\begin{aligned} \delta J_{HR} = & - \int_{\Omega} \left(\delta \hat{\mathbf{s}}^T \mathbf{R}_s^T \mathbf{E}_1 \mathbf{R}_\sigma \hat{\boldsymbol{\sigma}}' + \delta \hat{\mathbf{s}}^T \mathbf{R}_s^T \mathbf{E}_1 \mathbf{R}_{\sigma,x} \hat{\boldsymbol{\sigma}} + \delta \hat{\mathbf{s}}^T \mathbf{R}_s^T \mathbf{E}_2 \mathbf{R}_{\sigma,y} \hat{\boldsymbol{\sigma}} \right) d\Omega \\ & - \int_{\Omega} \left(\delta \hat{\boldsymbol{\sigma}}'^T \mathbf{R}_\sigma^T \mathbf{E}_1^T \mathbf{R}_s \hat{\mathbf{s}} + \delta \hat{\boldsymbol{\sigma}}^T \mathbf{R}_\sigma^T \mathbf{E}_1^T \mathbf{R}_{s,x} \hat{\mathbf{s}} + \delta \hat{\boldsymbol{\sigma}}^T \mathbf{R}_\sigma^T \mathbf{E}_2^T \mathbf{R}_{s,y} \hat{\mathbf{s}} \right) d\Omega \\ & - \int_{\Omega} \delta \hat{\boldsymbol{\sigma}}^T \mathbf{R}_\sigma^T \mathbf{D}^{-1} \mathbf{R}_\sigma \hat{\boldsymbol{\sigma}} d\Omega - \int_{\Omega} \delta \hat{\mathbf{s}}^T \mathbf{R}_s^T \mathbf{f} d\Omega = 0 \end{aligned} \quad (5.10)$$

Recalling that only the cross-section shape functions depend on y and splitting the integral over Ω into an integral over l and an integral over A , Equation (5.10) becomes:

$$\begin{aligned} \delta J_{HR} = & \int_l \left(-\delta \hat{\mathbf{s}}^T \mathbf{G}_{\sigma\sigma} \hat{\boldsymbol{\sigma}}' - \delta \hat{\mathbf{s}}^T \mathbf{H}_{s\sigma} \hat{\boldsymbol{\sigma}} - \delta \hat{\boldsymbol{\sigma}}'^T \mathbf{G}_{\sigma s} \hat{\mathbf{s}} - \delta \hat{\boldsymbol{\sigma}}^T \mathbf{H}_{\sigma s} \hat{\mathbf{s}} \right. \\ & \left. - \delta \hat{\boldsymbol{\sigma}}^T \mathbf{H}_{\sigma\sigma} \hat{\boldsymbol{\sigma}} - \delta \hat{\mathbf{s}}^T \mathbf{F} \right) dx = 0 \end{aligned} \quad (5.11)$$

where

$$\begin{aligned} \mathbf{H}_{\sigma s} = \mathbf{H}_{s\sigma}^T &= \int_A (\mathbf{R}_{\sigma,x}^T \mathbf{E}_1 \mathbf{R}_s + \mathbf{R}_{\sigma,y}^T \mathbf{E}_2 \mathbf{R}_s) dy; & \mathbf{F} &= \int_A \mathbf{R}_s^T \mathbf{f} dy; \\ \mathbf{H}_{\sigma\sigma} &= \int_A \mathbf{R}_\sigma^T \mathbf{D}^{-1} \mathbf{R}_\sigma dy; & \mathbf{G}_{\sigma s} = \mathbf{G}_{s\sigma}^T &= \int_A \mathbf{R}_\sigma^T \mathbf{E}_1^T \mathbf{R}_s dy \end{aligned}$$

Equation (5.11) represents the weak formulation of the 1D beam model. We highlight that the matrices $\mathbf{G}_{\sigma s}$, $\mathbf{H}_{\sigma s}$, and $\mathbf{H}_{\sigma\sigma}$ implicitly depend on x due to the cross-section shape function definition.

To obtain the corresponding boundary value problem, we integrate by parts the third term of Equation (5.11):

$$-\int_l \delta \hat{\boldsymbol{\sigma}}'^T \mathbf{G}_{\sigma s} \hat{\mathbf{s}} dx = -\delta \hat{\boldsymbol{\sigma}}^T \mathbf{G}_{\sigma s} \hat{\mathbf{s}} \Big|_{x=0}^{x=\bar{l}} + \int_l \delta \hat{\boldsymbol{\sigma}}^T \mathbf{G}'_{\sigma s} \hat{\mathbf{s}} dx + \int_l \delta \hat{\boldsymbol{\sigma}}^T \mathbf{G}_{\sigma s} \hat{\mathbf{s}}' dx \quad (5.12)$$

Substituting Equation (5.12) in Equation (5.11), recalling that $\delta \hat{\boldsymbol{\sigma}} = \mathbf{0}$ on $\partial\Omega_t$, and collecting the unknowns in a vector we obtain:

$$\int_l \{\delta \hat{\mathbf{s}}; \delta \hat{\boldsymbol{\sigma}}\}^T \left(\mathbf{G} \begin{Bmatrix} \hat{\mathbf{s}}' \\ \hat{\boldsymbol{\sigma}}' \end{Bmatrix} + \mathbf{H} \begin{Bmatrix} \hat{\mathbf{s}} \\ \hat{\boldsymbol{\sigma}} \end{Bmatrix} - \begin{Bmatrix} \mathbf{F} \\ \mathbf{0} \end{Bmatrix} \right) dx + \delta \hat{\boldsymbol{\sigma}}^T \mathbf{G}_{\sigma s} \hat{\mathbf{s}} \Big|_{\partial\Omega_s} = 0 \quad (5.13)$$

where

$$\mathbf{G} = \begin{bmatrix} \mathbf{0} & -\mathbf{G}_{s\sigma} \\ +\mathbf{G}_{\sigma s} & \mathbf{0} \end{bmatrix}; \quad \mathbf{H} = \begin{bmatrix} \mathbf{0} & -\mathbf{H}_{s\sigma} \\ \mathbf{G}'_{\sigma s} - \mathbf{H}_{\sigma s} & -\mathbf{H}_{\sigma\sigma} \end{bmatrix} \quad (5.14)$$

Requiring to satisfy Equation (5.13) for all the possible variations, we finally obtain the following ordinary differential equations:

$$\begin{cases} \mathbf{G} \begin{Bmatrix} \hat{\mathbf{s}}' \\ \hat{\boldsymbol{\sigma}}' \end{Bmatrix} + \mathbf{H} \begin{Bmatrix} \hat{\mathbf{s}} \\ \hat{\boldsymbol{\sigma}} \end{Bmatrix} = \begin{Bmatrix} \mathbf{F} \\ \mathbf{0} \end{Bmatrix} \\ + \text{suitable boundary conditions} \end{cases} \quad \text{in } l \quad (5.15)$$

5.3.3 Beam-model examples

In this section we give two examples of beam models with non-constant cross-section. More precisely, we derive:

1. a beam model for a tapered beam, assuming simplified kinematic and stresses; by means of this example we will illustrate how the introduction of non-constant cross-section modifies the coefficients governing the equations;
2. a beam model for a non-constant cross-section, assuming a refined kinematic and stresses.

5.3.3.1 Simplified kinematic and stress

In this section we give an example of a beam model developed using the strategies of Section 2.8.1. More precisely, starting from the HR div-div approach (Equation (5.15)), we derive a linear tapered beam model in which we use a first order displacement field, as already done in Section 3.4.3.1.

We consider a linearly tapered beam in which each cross-section is symmetric with respect to the beam axis. As a consequence the cross-section height $\bar{A}(x)$, the upper- and the lower- limits are defined as follows:

$$\bar{A}(x) = 2 \cdot h_0 - 2 \cdot h' \cdot x; \quad h_l = -h_u = -h_0 + h' \cdot x$$

where h_0 represents the cross-section height at $x = 0$ and h' represents the slope of the lateral surface.

We assume a first-order kinematic (as in Timoshenko model) and the usual cross-section stress distributions (obtained from the Jourawsky theory). In other words we make the following hy-

potheses:

$$\begin{array}{lll}
u = u_0(x) + yu_1(x) & \text{i.e.} & \mathbf{r}_u = \begin{Bmatrix} 1 \\ y \end{Bmatrix} & \hat{\mathbf{u}} = \begin{Bmatrix} u_0 \\ u_1 \end{Bmatrix} \\
v = v(x) & \text{i.e.} & \mathbf{r}_v = \{1\} & \hat{\mathbf{v}} = \{v\} \\
\sigma_{xx} = \sigma_{x0}(x) + y\sigma_{x1}(x) & \text{i.e.} & \mathbf{r}_{\sigma_x} = \begin{Bmatrix} 1 \\ y \end{Bmatrix} & \hat{\boldsymbol{\sigma}}_x = \begin{Bmatrix} \sigma_{x0} \\ \sigma_{x1} \end{Bmatrix} \\
\sigma_{yy} = 0 & \text{i.e.} & \mathbf{r}_{\sigma_y} = \{0\} & \hat{\boldsymbol{\sigma}}_y = \{0\} \\
\tau = \frac{(y - h_l)(h_u - y)}{(h_u - h_l)^2} \tau(x) & \text{i.e.} & \mathbf{r}_\tau = \left\{ \frac{(y - h_l)(h_u - y)}{(h_u - h_l)^2} \right\} & \hat{\boldsymbol{\tau}} = \{\tau\}
\end{array}$$

The matrices \mathbf{G} and \mathbf{H} defined in (5.14) and entering into the beam model (5.15), are explicitly given by:

$$\mathbf{G} = \begin{bmatrix} 0 & 0 & 0 & -\bar{A}(x) & 0 & 0 \\ 0 & 0 & 0 & 0 & -\frac{(\bar{A}(x))^3}{12} & 0 \\ 0 & 0 & 0 & -\frac{h'\bar{A}(x)}{2} & 0 & -\frac{2}{3}\bar{A}(x) \\ \bar{A}(x) & 0 & \frac{h'\bar{A}(x)}{2} & 0 & 0 & 0 \\ 0 & \frac{(\bar{A}(x))^3}{12} & 0 & 0 & 0 & 0 \\ 0 & 0 & \frac{2}{3}\bar{A}(x) & 0 & 0 & 0 \end{bmatrix} \quad (5.16)$$

$$\mathbf{H} = \begin{bmatrix} 0 & 0 & 0 & 0 & -\frac{h'\bar{A}(x)}{2} & 0 \\ 0 & 0 & 0 & 0 & 0 & \frac{2}{3}\bar{A}(x) \\ 0 & 0 & 0 & 0 & -\frac{h'^2\bar{A}(x)}{4} & 0 \\ 0 & 0 & 0 & -\frac{\bar{A}(x)}{E} \left(1 + \frac{h'}{4}\right)^2 & 0 & -\frac{2h'\bar{A}(x)(1+\nu)}{3 \cdot E} \\ -\frac{h'\bar{A}(x)}{2} & 0 & -\frac{h'^2\bar{A}(x)}{4} & 0 & -\frac{\bar{A}(x)^3}{12 \cdot E} \left(1 + \frac{h'}{4}\right)^2 & 0 \\ 0 & \frac{2}{3}\bar{A}(x) & 0 & 0 & 0 & -\frac{8}{15}\bar{A}(x) \frac{2(1+\nu)}{E} \end{bmatrix} \quad (5.17)$$

If we compare the matrices \mathbf{G} and \mathbf{H} defined above with the matrices obtained for 2D beam models with constant cross section (3.39) we notice the following statements.

- In the matrices that govern the define the model for the tapered cross-section beam, some entries explicitly depend on the slope of the lateral surface h' .
- If the taper slope h' vanishes, the matrices defined in (5.16) recover the constant cross-section beam matrices defined in (3.39).

5.3.3.2 Enhanced kinematic

As in Chapter 3, we assume that $\deg(\mathbf{r}_\gamma)$ denotes the highest polynomial degree with respect to y of the generic cross-section shape function. In the following, we assume the highest polynomial

degrees specified in Table (5.2). The same polynomial degrees was adopted in Chapter 3 that illustrate how the choice leads to a satisfactory beam model.

	\mathbf{r}_u	\mathbf{r}_v	\mathbf{r}_{σ_x}	\mathbf{r}_{σ_y}	\mathbf{r}_τ
$\deg(\mathbf{r}_\gamma)$	1	2	1	3	2

Table 5.2: Highest polynomial degree with respect to y of the cross-section shape functions used in beam modelling.

Using all the hypotheses listed in this section and through the symbolic calculus software MAPLE, we evaluate the matrices \mathbf{G} and \mathbf{H} for a general non-constant cross-section beam. We notice that $\text{rank}(\mathbf{G}) = 6$ whereas the model uses 10 independent variables. As a consequence, we conclude that beam model, as defined in (5.15) and with the refined kinematic specified in Table 5.2, is a differential-algebraic boundary value problem. Thus, 6 variables are solutions of a differential problem, while the remaining 4 unknowns are algebraically determined by the former ones. Since \mathbf{G} and \mathbf{H} are matrices of non-constant coefficients, it is not possible to evaluate the homogeneous solution of the differential equation. Nevertheless, we can suppose that considerations done in (Auricchio et al., 2010) about constant cross-section beam model are still valid.

Moreover, comparing the constant and non-constant cross-section beam models, we observe that the latter does not use more independent variables. On the contrary, the non-constant cross-section beam model increments the matrices fill-in (e.g. compare \mathbf{H}_{σ_s} definition given in Equation (5.11) and $\mathbf{H}_{\sigma's}$ definition given in Equation 26 of (Auricchio et al., 2010)). As a consequence, we conclude that the proposed model introduces new variable relations that, hopefully, will take into account naturally the axial and bending equations coupling.

5.4 FE derivation

To obtain the beam FE formulation we integrate by parts the weak formulation of the beam model (5.11), we introduce the axis approximation (2.21) and we perform an integration along the axis.

Starting from beam model variational formulation (5.11), we assume $\partial\Omega_s = A_0$, $A_l \subset \partial\Omega_t$ and $\bar{\mathbf{s}} = \mathbf{0}$. We start integrating by parts with respect to the x direction both the third and the first terms of Equation (5.11), see (5.12) and the following equations:

$$-\int_l \delta \hat{\mathbf{s}}'^T \mathbf{G}_{s\sigma} \hat{\boldsymbol{\sigma}} dx = -\delta \hat{\mathbf{s}}^T \mathbf{G}_{s\sigma} \hat{\boldsymbol{\sigma}} \Big|_{x=0}^{x=l} + \int_l \delta \hat{\mathbf{s}}^T \mathbf{G}'_{s\sigma} \hat{\boldsymbol{\sigma}} dx + \int_l \delta \hat{\mathbf{s}}^T \mathbf{G}_{s\sigma} \hat{\boldsymbol{\sigma}}' dx \quad (5.18)$$

Substituting Equations (5.12) and (5.18) into Equation (5.11) we obtain an alternative beam model formulation:

Find $\hat{\mathbf{s}} \in \widetilde{W}$ and $\hat{\boldsymbol{\sigma}} \in \widetilde{S}$ such that $\forall \delta \hat{\mathbf{s}} \in \widetilde{W}$ and $\forall \delta \hat{\boldsymbol{\sigma}} \in \widetilde{S}$

$$\delta J_{HR} = \int_l \left(\delta \hat{\mathbf{s}}'^T \mathbf{G}_{s\sigma} \hat{\boldsymbol{\sigma}} + \delta \hat{\mathbf{s}}^T \mathbf{G}'_{s\sigma} \hat{\boldsymbol{\sigma}} - \delta \hat{\mathbf{s}}^T \mathbf{H}_{s\sigma} \hat{\boldsymbol{\sigma}} + \delta \hat{\boldsymbol{\sigma}}^T \mathbf{G}_{\sigma s} \hat{\mathbf{s}}' + \delta \hat{\boldsymbol{\sigma}}^T \mathbf{G}'_{\sigma s} \hat{\mathbf{s}} - \delta \hat{\boldsymbol{\sigma}}^T \mathbf{H}_{\sigma s} \hat{\mathbf{s}} \right. \\ \left. - \delta \hat{\boldsymbol{\sigma}}^T \mathbf{H}_{\sigma\sigma} \hat{\boldsymbol{\sigma}} - \delta \hat{\mathbf{s}}^T \mathbf{F} \right) dx - \delta \hat{\mathbf{s}}^T \mathbf{T} = 0 \quad (5.19)$$

where $\widetilde{W} := \{\hat{\mathbf{s}} \in H^1(l) : \hat{\mathbf{s}}|_{x=0} = \mathbf{0}\}$; $\widetilde{S} := L^2(l)$ and $\mathbf{T} = \int_{A_l} \mathbf{R}_s^T \mathbf{t} dA$

The FE discretization of the beam model follows from the introduction of the axis shape

function approximation (2.21) into the variational formulation (5.19):

$$\begin{aligned} \delta J_{HR} = \int_l & \left(\delta \tilde{\mathbf{s}}^T \mathbf{N}_s'^T \mathbf{G}_{s\sigma} \mathbf{N}_\sigma \tilde{\boldsymbol{\sigma}} + \delta \tilde{\mathbf{s}}^T \mathbf{N}_s^T \mathbf{G}'_{s\sigma} \mathbf{N}_\sigma \tilde{\boldsymbol{\sigma}} - \delta \tilde{\mathbf{s}}^T \mathbf{N}_s^T \mathbf{H}_{s\sigma} \mathbf{N}_\sigma \tilde{\boldsymbol{\sigma}} \right. \\ & + \delta \tilde{\boldsymbol{\sigma}}^T \mathbf{N}_\sigma^T \mathbf{G}_{\sigma s} \mathbf{N}_s' \tilde{\mathbf{s}} + \delta \tilde{\boldsymbol{\sigma}}^T \mathbf{N}_\sigma^T \mathbf{G}'_{\sigma s} \mathbf{N}_s \tilde{\mathbf{s}} - \delta \tilde{\boldsymbol{\sigma}}^T \mathbf{N}_\sigma^T \mathbf{H}_{\sigma s} \mathbf{N}_s \tilde{\mathbf{s}} \\ & \left. - \delta \tilde{\boldsymbol{\sigma}}^T \mathbf{N}_\sigma^T \mathbf{H}_{\sigma\sigma} \mathbf{N}_\sigma \tilde{\boldsymbol{\sigma}} - \delta \tilde{\mathbf{s}}^T \mathbf{N}_s^T \mathbf{F} \right) dx - \delta \tilde{\mathbf{s}}^T \mathbf{N}_s^T \mathbf{T} = 0 \end{aligned} \quad (5.20)$$

Collecting unknown coefficients in a vector and requiring (5.20) to be satisfied for all possible virtual fields we obtain:

$$\begin{bmatrix} \mathbf{0} & \mathbf{K}_{s\sigma} \\ \mathbf{K}_{\sigma s} & \mathbf{K}_{\sigma\sigma} \end{bmatrix} \begin{Bmatrix} \tilde{\mathbf{s}} \\ \tilde{\boldsymbol{\sigma}} \end{Bmatrix} = \begin{Bmatrix} \tilde{\mathbf{T}} \\ \mathbf{0} \end{Bmatrix} \quad (5.21)$$

where

$$\begin{aligned} \mathbf{K}_{s\sigma} &= \mathbf{K}_{\sigma s}^T = \int_l (\mathbf{N}_s'^T \mathbf{G}_{s\sigma} \mathbf{N}_\sigma + \mathbf{N}_s^T \mathbf{G}'_{s\sigma} \mathbf{N}_\sigma - \mathbf{N}_s^T \mathbf{H}_{s\sigma} \mathbf{N}_\sigma) dx; \\ \mathbf{K}_{\sigma\sigma} &= - \int_l \mathbf{N}_\sigma^T \mathbf{H}_{\sigma\sigma} \mathbf{N}_\sigma dx; \quad \tilde{\mathbf{T}} = - \int_l \mathbf{N}_s^T \mathbf{F} dx - \mathbf{N}_s^T|_{x=\bar{l}} \mathbf{T} \end{aligned}$$

About the properties of the axis shape functions, we refer to Section 6.1 of (Auricchio et al., 2010).

5.5 Numerical examples

In this section we discuss the numerical results of some significant test cases, in order to understand the model's and FE's capabilities.

We start considering a symmetric tapered beam for which compare the numerical results with the analytical solutions available in literature. In the following we give some remarks on the stiffness-matrix condition-number and we conclude considering an arch-shaped beam that shows the capability of the beam model to take into account also complex geometries with high accuracy.

All the presented examples are implemented in MAPLE software which allows to calculate the stiffness matrices using symbolic calculus. Obviously, the same results could be obtained also using numerical-calculus tools, with the shrewdness to use suitable integration rules.

5.5.1 Symmetric tapered beam

In the following we consider the tapered beam illustrated in Figure 5.2. We assume $E = 10^5 \text{MPa}$ and $\nu = 0.25$. Moreover, as illustrated in Figure 5.2, the beam is clamped in the initial cross section $\bar{A}(0)$ and a concentrated load $\mathbf{q} = [0, -1] \text{N}$ acts in the lower limit of the final cross-section $\bar{A}(\bar{l})$. About FE beam model, we discretize the axis through an homogeneous mesh of 20 elements.

Figure 5.3 plots the displacement axial coefficients $\hat{\mathbf{u}}$ and $\hat{\mathbf{v}}$ obtained through the FE scheme introduced in Section 5.4.

In the considered example, we use the following displacement cross-section shape functions:

$$\mathbf{r}_u = \{1; \quad y\}^T; \quad \mathbf{r}_v = \{1; \quad y; \quad y^2\}^T; \quad (5.22)$$

As a consequence, the axial coefficients have physical meanings.

- \hat{v}_1 is the mean value of transversal displacement.
- \hat{v}_2 is associated to the change of cross-section length.
- \hat{v}_3 is a deformation of the cross-section within its plane.

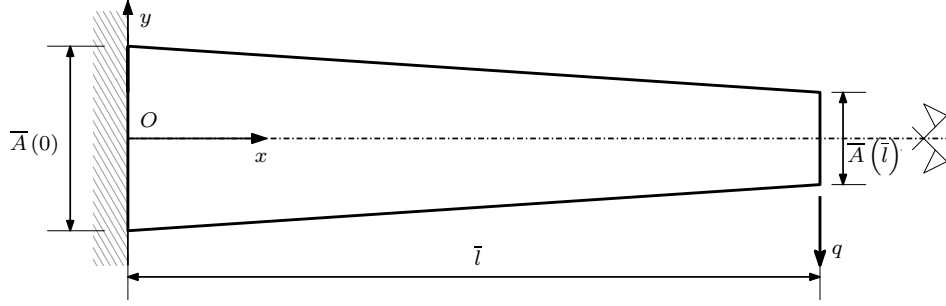
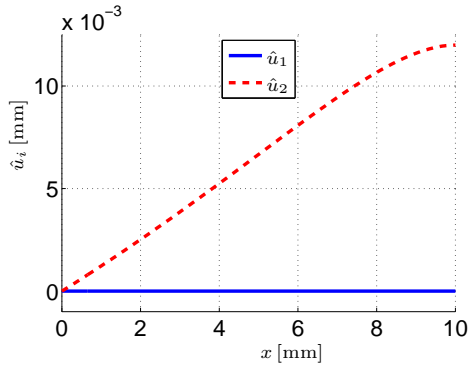
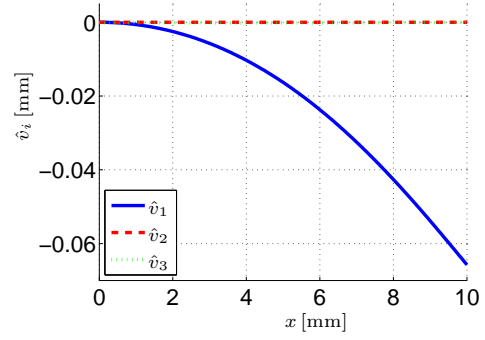


Figure 5.2: Symmetric tapered beam: $\bar{l} = 10\text{mm}$, $\bar{A}(0) = 1\text{mm}$, $\bar{A}(\bar{l}) = 0.5\text{mm}$, $q = 1\text{N}$, $E = 100000\text{MPa}$, and $\nu = 0.25$.



(a) Horizontal displacement, axial coefficient functions \hat{u}_i $i = 1, 2$.



(b) Vertical displacement, axial coefficient functions \hat{v}_i $i = 1, 2, 3$.

Figure 5.3: Displacement axial coefficient functions, evaluated for a symmetric tapered beam under shear-bending load.

- \hat{u}_1 is the mean value of axial displacement.
- \hat{u}_2 is the cross-section rotation.

We notice that the distributions of the displacement mean values \hat{v}_1 and \hat{u}_1 are qualitatively not far from the results of the Euler-Bernoulli beam with constant cross section.

Figures 5.4(a), 5.4(b), and 5.4(e) plot the stress axial coefficient functions. Referring to Figure 5.4(a), the axial coefficient function $\hat{\sigma}_{x1}$ indicates the value of the axial stress at the bottom of the cross section whereas $\hat{\sigma}_{x2}$ indicates the same value at the top of the cross section. Figure 5.4(c) plots the axis distribution of bending moment $M(x)$ which definition is recalled in the following:

$$M(x) = \int_{A(x)} \sigma_x \cdot y \, dy \quad (5.23)$$

The bending moment distribution $M(x)$ agrees with the classical beam theories, in fact it varies linearly along the axis, being equal to zero in the final cross-section and equal to $q \cdot \bar{l} = 10\text{Nmm}$ in the initial cross-section. On the other hand, the axial coefficient functions are non-linear in order to compensate the change of the cross-section thickness.

Figure 5.4(d) plots the axis distribution of resulting shear $V(x)$ which definition is recalled in the following:

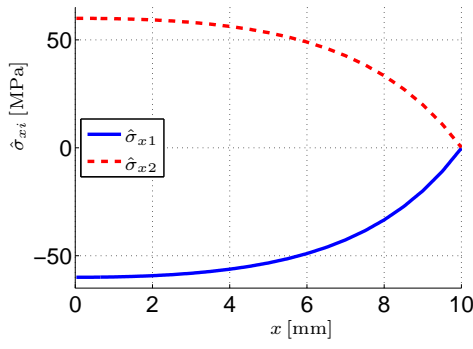
$$V(x) = \int_{A(x)} \tau \, dy \quad (5.24)$$

The resulting shear $V(x)$ is constant and equal to -1N , with some numerical noises, that give errors in the order of magnitude of $5 \cdot 10^{-6}$. Also the resulting shear distribution agrees with the classical beam theories. Once again, the resulting shear is constant whereas the beam variable $\hat{\tau}_1(x)$ is non linear in order to compensate the cross-section changes.

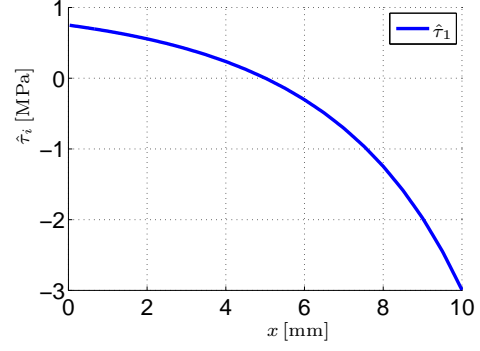
In Figure 5.4(e), far from the initial and final cross-sections, the axial coefficient functions $\hat{\sigma}_{yi}$ have an order of magnitude negligible with respect to the other stress components. Nevertheless, we can appreciate how $\hat{\sigma}_{yi}$ tends to increase going from the initial to the final cross-section. Moreover, close to the initial and final cross-sections, the axial coefficient functions $\hat{\sigma}_{yi}$ significantly oscillate. In (Auricchio et al., 2010), the solution oscillations are associated to the boundary effects. Nevertheless, in the specific case we are discussing, it is not clear if the oscillations have a physical meaning or are associated to some numerical instability.

Figure 5.5 plots the cross-section distributions of σ_x and σ_y stresses. Specifically, the label *num* indicates the numerical solution obtained through the FE introduced in Section 5.4, whereas the label *an* indicates the analytical solution obtained considering the solutions of the loaded wedge, available in literature (see (Timoshenko and Goodier, 1951)[Section 35]). About analytical solution, we consider a wedge obtained extending the lines constituting the lower and upper limits of the beam illustrated in Figure 5.2 and a force system acting on the wedge end that produces the same bending moment and resulting shear of the load applied on the final cross-section of the tapered beam. In order to exclude any boundary effects, we consider the cross section $A(5)$. We highlight the good agreement between numerical results and analytical solution.

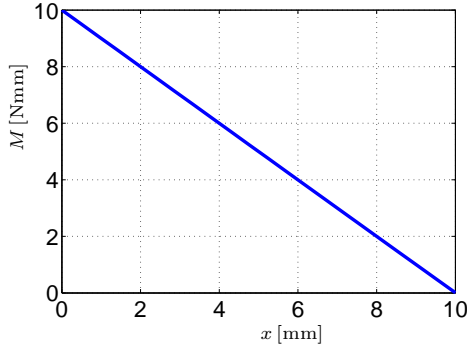
The shear cross-section distribution τ requires some additional remarks. Figures 5.6(a), 5.6(b), and 5.6(c) plot the shear distributions evaluated on the cross sections $A(2.5)$, $A(5)$, and $A(7.5)$, respectively. It is possible to appreciate a change of concavity in shear distribution that agrees with the analytical solution and the sign of shear axial coefficient function (see Figure 5.4(b)). In Figures 5.6(a) and 5.6(c), qualitatively, we see a good agreement between the numerical and analytical solutions. Moreover, the analytical solution depicted in Figure 5.6(b) shows oscillations whereas the numerical solution has a negligible curvature. This may be the consequence of the poor shape functions adopted in beam modelling that appear to be not



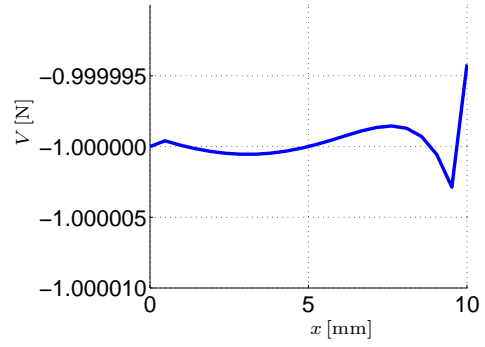
(a) Axial stress, axial coefficient functions $\hat{\sigma}_{xi}$ $i = 1, 2$.



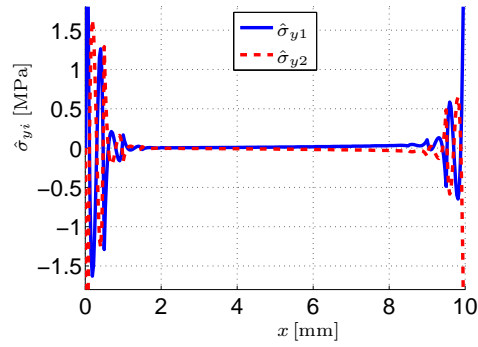
(b) Shear stress, axial coefficient function $\hat{\tau}_1$.



(c) Resulting bending moment, axial distribution $M(x)$.



(d) Resulting shear, axial distribution $V(x)$.



(e) Transversal stress, axial coefficient functions $\hat{\sigma}_{yi}$ $i = 1, 2$.

Figure 5.4: Stress axial coefficient functions (Subfigure 5.4(a), 5.4(b), and 5.4(e)) and resulting internal actions (Subfigure 5.4(c), and 5.4(d)), evaluated for a symmetric tapered beam under shear-bending load.

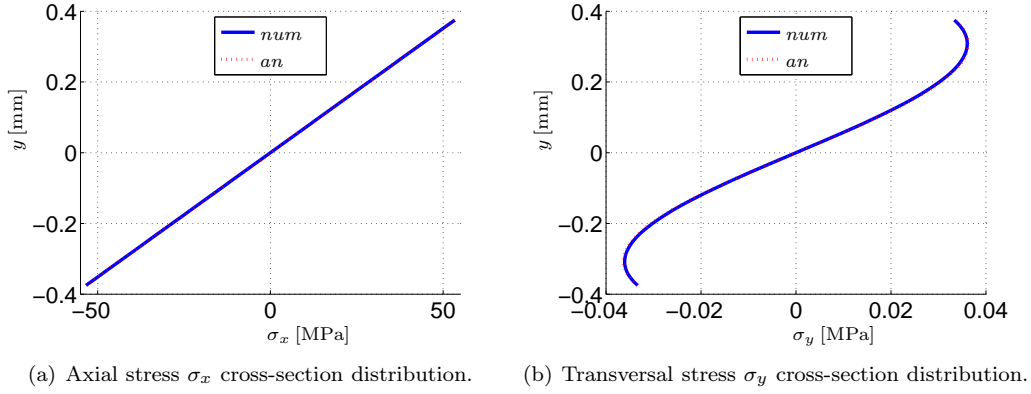


Figure 5.5: Axial (Figure 5.5(a)) and transversal (Figure 5.5(a)) stress cross-section distributions, evaluated in the cross section $A(5)$.

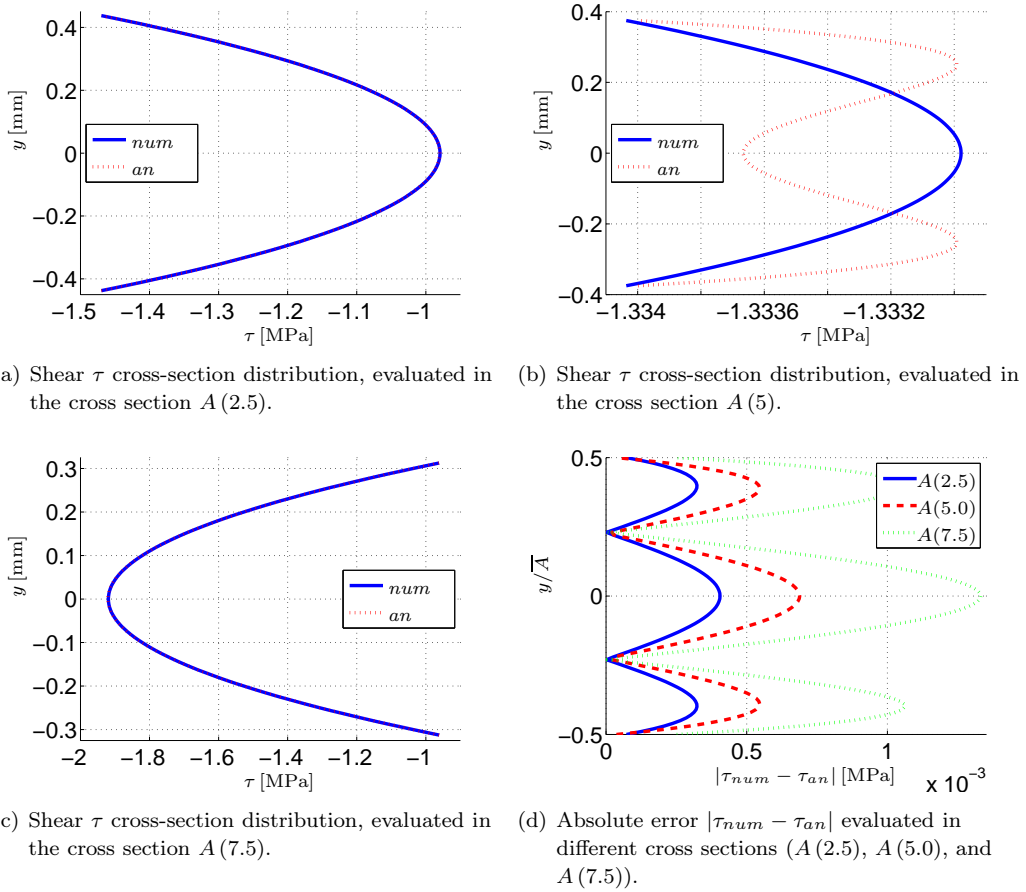


Figure 5.6: Cross-section shear distributions (Figures 5.6(a), 5.6(b), and 5.6(c)) and related absolute errors (Figure 5.6(d)).

able to catch the high frequency oscillations of the analytical solution. This statement is confirmed also by Figure 5.6(d) that plots the absolute error in the three considered cross sections. In all the considered cases, the maximum absolute error is 3 order of magnitude less than the shear mean-value.

5.5.2 Stiffness-matrix condition-number

In this section we discuss the behaviour of the stiffness-matrix condition-number, which definition is recalled in the following:

$$\text{cond}(\mathbf{A}) := \|\mathbf{A}\| \cdot \|\mathbf{A}^{-1}\| \quad (5.25)$$

The norm of the generic matrix \mathbf{A} of size $n \times n$ is defined as follows:

$$\|\mathbf{A}\| := \max_{i=1 \dots n} \left\{ \sum_{j=1}^n a_{ij} \right\} \quad (5.26)$$

First of all, we notice that, applying the FE method introduced in Section 5.4 to a tapered beam with the final cross-section height that tends to zero, we obtain a stiffness-matrix condition-number that goes to infinity. Considering the limit case of a wedge shaped beam, we obtain a singular stiffness-matrix. As a consequence, we consider significant an investigation of the condition number of stiffness-matrix in order to understand how the geometry parameters influence the condition number and the effectiveness of the proposed beam model.

Figure 5.9(a) plots the variation of the condition-number evaluated for a constant cross-section beam, varying the number of axis-FE and the beam height. We notice that, in general, the condition-number becomes bigger and bigger increasing the beam slenderness \bar{l}/h and increasing the number of elements used to discretize the axis. Nevertheless, we notice also that the slope of plots is constant and independent from the beam slenderness.

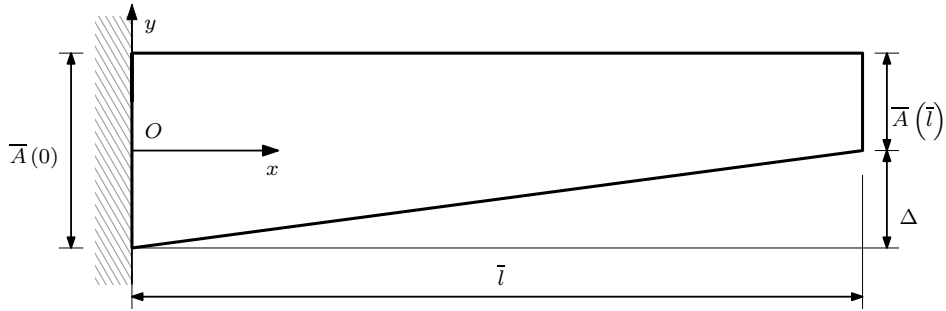


Figure 5.7: Non-symmetric tapered beam: $\bar{l} = 10\text{mm}$, $\bar{A}(0) = \bar{A}(\bar{l}) + \Delta$, $E = 100000\text{MPa}$, and $\nu = 0.25$.

Δ	$A(0)$	$A(\bar{l})$	h'_l
0.0	5.50	5.50	0.00
0.1	5.55	5.45	0.01
1.0	6.00	4.00	0.10
5.0	8.00	3.00	0.50
10.0	10.50	0.50	1.00

Table 5.3: Non-symmetric tapered beams, parameter definitions for the considered examples

Figure 5.9(b) plots the variation of the condition number evaluated for the non-symmetric tapered beam depicted in Figure 5.7. The number of axis-FE and the difference between the initial

and final cross-section heights Δ are the independent parameters considered in Figure 5.9(b). In order to exclude the influence of the beam slenderness on the condition number, we choose initial and final cross-section measures such that the average of thickness is equal to 5.5mm in all the considered cases, as specified in Table 5.3. We notice that an increase of Δ produces not only a worsening of the condition number but also an increase of slope of plots. On the other hand, as we can see in Table 5.3, the slope of lateral surface is proportional to the parameter Δ and, in Figure 5.9(b) we can not distinguish the effects of the two parameters on the condition number.

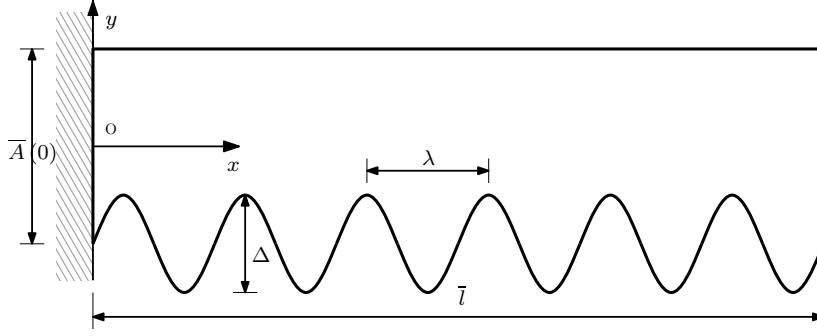


Figure 5.8: Non-constant cross-section beam: $\bar{l} = 10\text{mm}$, $\bar{A}(0) = 1\text{mm}$, $\Delta = 0.46875\text{mm}$, $E = 100000\text{MPa}$, and $\nu = 0.25$.

wave number	λ	h'_m
0	-	0
1	10.00	$\frac{1}{8}$
2	5.00	$\frac{1}{4}$
4	2.50	$\frac{1}{2}$
8	1.25	1

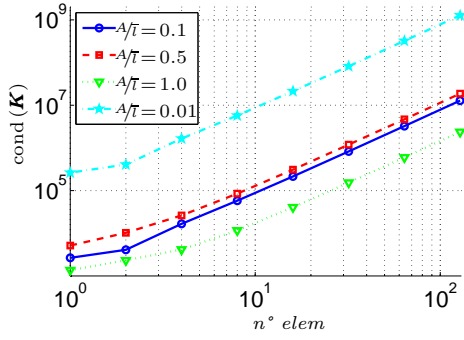
Table 5.4: Non-constant cross-section beams, parameter definitions for the considered examples

To investigate the effect of increase of slope separately from the effect of the difference of cross-section height, we consider the non constant cross-section beam illustrated in Figure 5.8. The lower limit of the beam illustrated in Figure 5.8 is a periodic piecewise cubic polynomial. We define the maximum slope h'_m as follows:

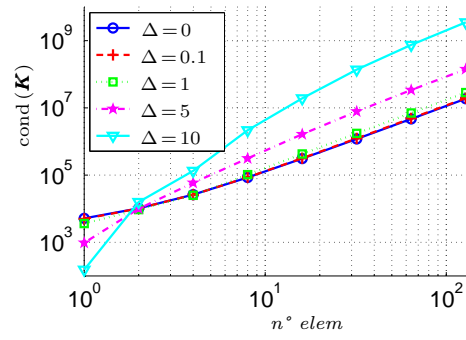
$$h'_m := \max_{x \in l} (|h'_l|) \quad (5.27)$$

As illustrated in Table 5.4, we consider different wave length such that we increase the maximum slope h'_m but we do not modify the difference of cross-section heights Δ . Figure 5.9(c) plots the variations of condition number with respect to the number of axis elements and the maximum slope h'_m . We observe that the maximum slope h'_m does not influence significantly the condition number, at least for the considered values of practical interest.

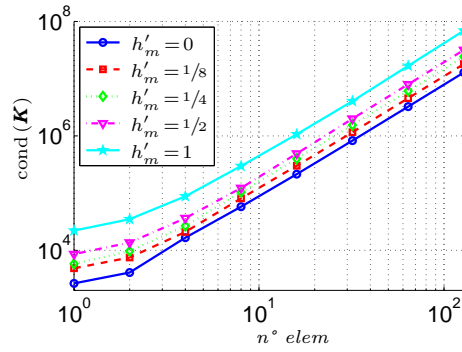
As a general remark, we notice that the condition number remains into a reasonable range for the most of practical applications, but it could lead significant errors for high-refined meshes, beams with high taper slope, and very slender beams.



(a) Condition number, evaluated for a constant cross-section beam with different ratio A/l .



(b) Condition number, evaluated for a non-symmetric tapered beam with different taper slope.



(c) Condition number, evaluated for a non-constant cross-section beam with different boundary slope.

Figure 5.9: Stiffness matrix condition number.

5.5.3 Arch shaped beam

In this Subsection we consider the arch shaped beam illustrated in Figure 5.10. The lower and the upper limits are defined respectively as:

$$h_l := -\frac{1}{50}x^2 + \frac{1}{5}x - \frac{1}{2}; \quad h_u := \frac{1}{10} \quad (5.28)$$

Moreover, the beam is clamped in the initial cross-section and loaded on the final cross-section with a constant axial load distribution $\mathbf{t}|_{A_l} = [1, 0, 0]^T$ N/mm.

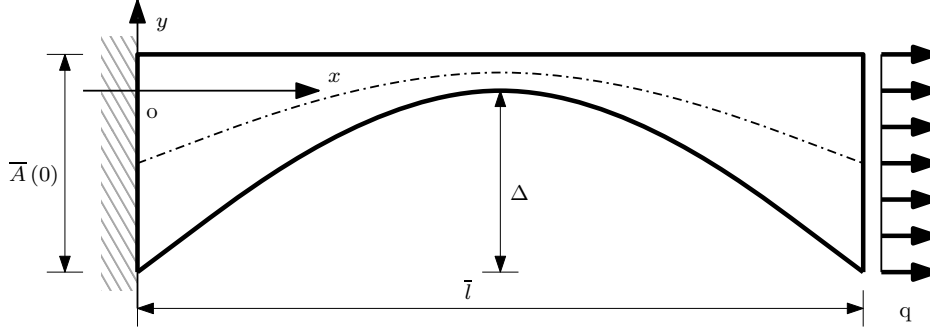


Figure 5.10: Arch shaped beam: $\bar{l} = 10\text{mm}$, $\Delta = 0.5\text{mm}$, $\bar{A}(\bar{l}) = \bar{A}(0) = 0.6\text{mm}$, $q = 1\text{N/mm}$, $E = 100000\text{MPa}$, and $\nu = 0.25$.

About FE beam model, we discretize the axis through a regular mesh of 20 elements.

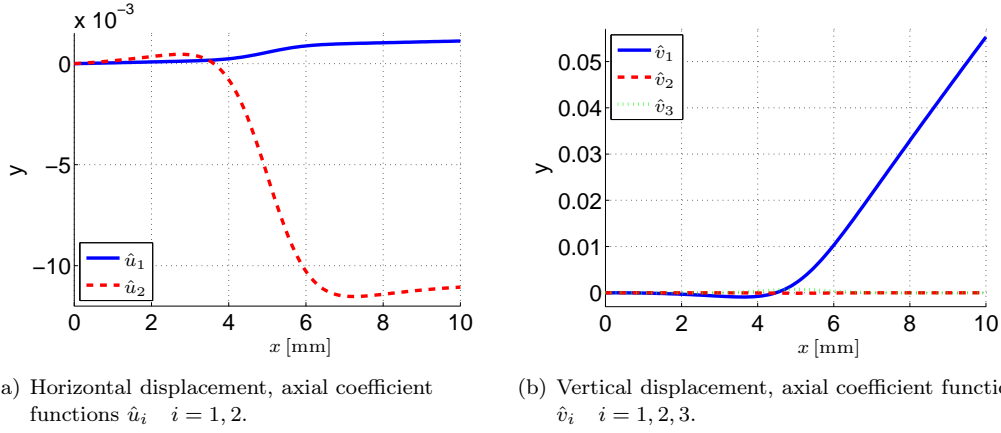


Figure 5.11: Displacement axial coefficient functions, evaluated for an arch shaped beam under axial load.

Figure 5.11 plots the displacement axial coefficients. We highlight that the solution shows significant transversal displacement (see \hat{v}_1 in Figure 5.11(b)) and cross-section rotation (see \hat{u}_2 in Figure 5.11(a)) produced by the axial load.

Figure 5.12 plots the stress axial coefficients, Figure 5.13(a) plots the resulting axial stress, and Figure 5.13(b) plots the eccentricity, defined as:

$$e(x) := \frac{M(x)}{|\mathbf{t}|} \quad (5.29)$$

Specifically e_{num} denotes the eccentricity evaluated considering the FE solution whereas e_{an} denotes the eccentricity evaluated analytically (it coincides with the positions of cross-section

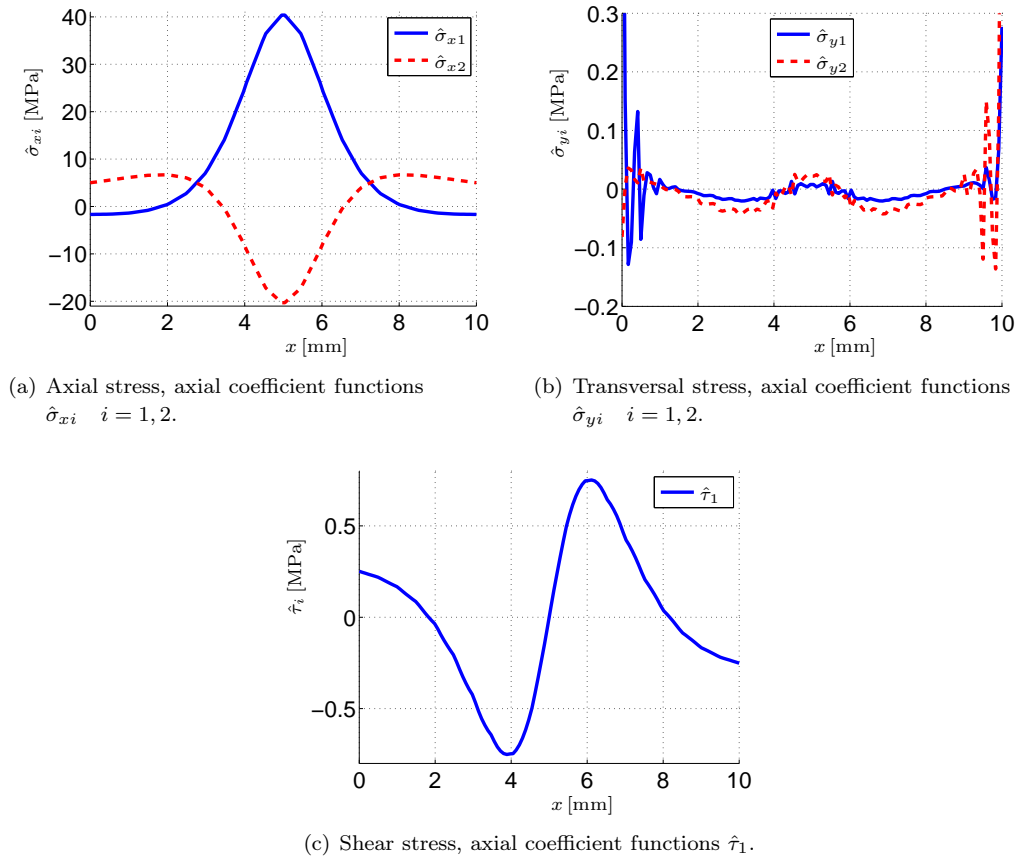


Figure 5.12: Stress axial coefficient functions, evaluated for an arch shaped beam under axial load.

barycentre). We notice that the stress axial-distributions are highly non linear whereas the resulting axial load is constant and equal to the resulting applied load. Precisely, Figure 5.13(a) highlights a small error, in the order of the 0.5% in the resulting axial stress. Moreover, the numerical eccentricity e_{num} coincides with the analytical eccentricity e_{an} . As a consequence, we conclude that the proposed beam model has the capability to model the coupling of axial load and bending moment. We highlight also that the coupling factors are obtained naturally from the dimensional reduction procedure illustrated in Section 5.3, leading the model to be extremely efficient and effective.

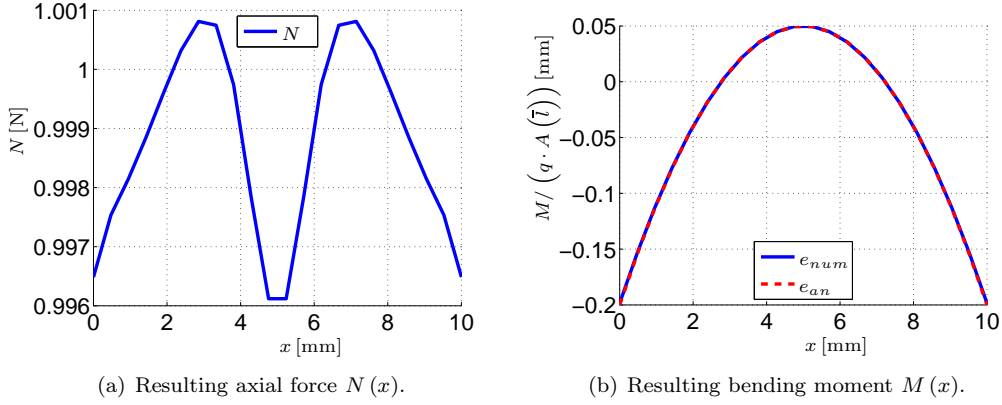


Figure 5.13: Resulting actions distributions, evaluated for an arch shaped beam under axial load.

Chapter 6

Final Remarks

In this thesis we apply the dimensional reduction modelling approach to obtain some, linear, elastic beam-models. In a second moment we discretize the beam-models through a classical *finite element procedure*.

The comparison of different weak formulations points out the advantages of mixed-functionals. In particular, the Hellinger-Reissner functional formulation that finds the stress solution in the $H(\text{div}, \Omega)$ results to be the most interesting starting point since it privileges the accuracy of stress description.

Analytical and numerical examples highlight that the resulting mixed beam models do not need correction factors. Moreover, for the non-homogeneous cross-section beam, they take correctly into account also equation couplings. Finally, the beam model can predict the local effects of both boundary displacement constraints and non homogeneous or concentrated boundary load distributions.

The proposed FE discretisation has the peculiarity to find the axial-coefficient displacements and stresses in $H^1(l)$ and $L^2(l)$ whereas the initial HR functional requires that the displacements and stresses belong to $L^2(\Omega)$ and $H(\text{div}, \Omega)$ respectively.

Several numerical tests highlight the following positive statements.

- The finite element-solution converges to the analytical solution providing accurate description of both displacement and stresses.
- The computational efforts produce significant benefits in solution accuracy leading the proposed method to be convenient with respect to the standard ones usually adopted in practice.
- The beam model shows the expected asymptotic behaviour.
- The beam model the corresponding finite element are able to model complex bodies.

On the other hand, the numerical tests highlight also the following critical points.

- Numerical instabilities and spurious oscillations could occur close to regions of stress concentration.
- The stiffness-matrix condition number could hamper the FE effectiveness, in particular for extremely slender beam elements and for non-constant cross-section beams with big changes of the cross-section size.

Nevertheless, the limitations listed so far do not influence significantly the model effectiveness, at least for the cases of practical interest.

Finally, the following topics could be further investigated in the future.

- Development of models that consider more general cross-section meshes, as triangular or quadrilateral fibres.
- Models of beams made of anisotropic materials.
- Multilayer non-constant cross-section beams.
- 3D non-constant cross-section beams.
- Multilayer plate models.

Bibliography

EN 1990: Basis of structural design.

(2010). *A new modelling approach for planar beams*.

(2012). *Mixed 3D beam models: differential equation derivation and finite element solutions*.

Adams, S. and B. Cockburn (2005). A mixed finite element method for elasticity in three dimensions. *Journal of scientific computing* 25, 515–521.

Alessandrini, S. M., D. N. Arnold, R. S. Falk, and A. L. Madureira (1999). Derivation and justification of plate models by variational methods. *CRM Proceedings and Lecture Notes* 21, 1–20.

Allen, D. H. (2013). *Introduction to the mechanics of deformable solids: Bars and beams*. Springer.

Allix, O. and C. Dupleix-Couderc (2010). A plate theory as a mean to compute precise 3D solutions including edge effects and related issues. *New trends in thin structures: formulation, optimization and coupled problems*, 1–28.

Amara, M. and J. Thomas (1979). Equilibrium finite elements for the linear elastic problem. *Num* 33, 367–383.

Arnold, D. N., G. Awanou, and R. Winther (2008). Finite element for symmetric tensors in three dimensions. *Mathematics of Computation* 263, 1229–1251.

Arnold, D. N. and R. S. Falk (1988). A new mixed formulation for elasticity. *Numerische Mathematik* 53, 13–30.

Auricchio, F., G. Balduzzi, and C. Lovadina (2010). A new modeling approach for planar beams: Finite-element solutions based on mixed variational derivations. *Journal of Mechanic of Materials and Structures* 5, 771–794.

Auricchio, F., G. Balduzzi, and C. Lovadina (2013). The dimensional reduction modelling approach for 3D beams: Differential equations and finite-element solutions based on hellinger-reissner principle. *International Journal of Solids and Structures* 50, 4184–4196.

Auricchio, F., C. Lovadina, and A. L. Madureira (2004). An asymptotically optimal model for isotropic heterogeneous linearly elastic plates. *ESAIM Mathematical Modelling and Numerical Analysis* 38, 877–897.

Auricchio, F. and E. Sacco (1999). A mixed-enhanced finite-element for the analysis of laminated composite plates. *International Journal for Numerical Methods in Engineering* 44, 1481–1504.

- Banerjee, J. R. and F. W. Williams (1985). Exact bernoulli-euler dynamic stiffness matrix for a range of tapered beams. *International Journal for Numerical Methods in Engineering* 21(12), 2289–2302.
- Banerjee, J. R. and F. W. Williams (1986). Exact bernoulli-euler static stiffness matrix for a range of tapered beam-columns. *International Journal for Numerical Methods in Engineering* 23, 1615–1628.
- Batra, R., S. Vidoli, and F. Vestroni (2002). Plane wave solutions and modal analysis in higher order shear and normal deformable plate theories. *Journal of Sound and Vibration* 257, 63–88.
- Batra, R. C. and S. Vidoli (2002). Hogher-order piezoelectric plate theory derived from a three-dimensional variational principle. *AIAA (American Institute of Aeronautics and Astronautics) journal* 40, 91–104.
- Boley, B. A. (1963). On the accuracy of the bernoulli-euler theory for beams of variable section. *Journal of Applied Mechanics* 30, 374–378.
- Brezzi, F. and M. Fortin (1991). *Mixed and hybrid finite element methods*. New York, NY, USA: Springer-Verlag New York, Inc.
- Carrera, E. (2000). Assessment of mixed and classical theories on global and local response of multilayered orthotropic plates. *Composite Structures* 50, 183–198.
- Carrera, E. (2001). Developments, ideas and evaluations based upon reissner’s mixed variational theorem in the modelling of multilayered plates and shells. *Applied Mechanics Review* 54, 301–329.
- Carrera, E. and L. Demasi (2002). Classical and advanced multilayered plate elements based upon pvd and rmvt. part 1: derivation of finite element matrices. *International Journal for Numerical Methods in Engineering* 55, 191–231.
- Ciarlet, P. (1997). *Theory of Plates*. Number volume 2 in Studies in mathematics and its applications. Elsevier Science.
- Dauge, M., A. Rossle, and Z. Yosibash (2002). Higher-order response of three-dimensional elastic plate structures and their numerical illustration by p-FEM. *International Journal for Numerical Methods in Engineering* 53, 1353–1376.
- Demasi, L. (2009a). Mixed plate theories based on the generalized unified formulation. part i: governing equations. *Composite Structures* 87, 1–11.
- Demasi, L. (2009b). Mixed plate theories based on the generalized unified formulation. part ii: layerwise theories. *Composite Structures* 87, 12–22.
- Demasi, L. (2009c). Mixed plate theories based on the generalized unified formulation. part iii: advanced mixed high order shear deformation theories. *Composite Structures* 87, 183–194.
- Demasi, L. (2009d). Mixed plate theories based on the generalized unified formulation. part iv: zig-zag theories. *Composite Structures* 87, 195–205.
- Demasi, L. (2009e). Mixed plate theories based on the generalized unified formulation. part v: results. *Composite Structures* 88, 1–16.

- Dong, S. B., J. B. Kosmatka, and H. C. Lin (2001). On Saint-Venant's problem for an inhomogeneous, anisotropic cylinder - part I: methodology for Saint-Venant solutions. *ASME, Journal of Applied Mechanics* 68, 376–381.
- Feng, W. and S. Hoa (1998). Partial hybrid finite elements for composite laminates. *Finite Elements in Analysis and Design* 30, 365–382.
- Gruttmann, F., R. Sauer, and W. Wagner (1999). Shear stresses in prismatic beams with arbitrary cross-sections. *International journal for numerical methods in engineering* 45, 865–889.
- Hjelmstad, K. and E. Taciroglu (2002). Mixed methods and flexibility approaches for nonlinear frame analysis. *Journal of constructional steel research* 58, 967–993.
- Hjelmstad, K. and E. Taciroglu (2003). Mixed variational methods for finite element analysis of geometrically non-linear, inelastic bernoulli-euler beams. *Communications in numerical methods in engineering* 19, 809–832.
- Hjelmstad, K. and E. Taciroglu (2005). Variational basis of nonlinear flexibility methods for structural analysis of frames. *Journal of engineering mechanics* 131, 1157–1169.
- Hjelmstad, K. D. (2005). *Fundamentals of structural mechanics*. Springer.
- Hodges, D. H., J. C. Ho, and W. Yu (2008). The effect of taper on section constants for in-plane deformation of an isotropic strip. *Journal of Mechanic of Materials and Structures* 3, 425–440.
- Hodges, D. H., A. Rajagopal, J. C. Ho, and W. Yu (2010). Stress and strain recovery for the in-plane deformation of an isotropic tapered strip-beam. *Journal of Mechanic of Materials and Structures* 5, 963–975.
- Huang, Y., S. Di, C. Wu, and H. Sun (2002). Bending analysis of composite laminated plates using a partially hybrid stress element with interlaminar continuity. *Computers and Structures* 80, 403–410.
- Icardi, U. and A. Atzori (2004). Simple, efficient mixed solid element for accurate analysis of local effects in laminated and sandwich composites. *Advances in Engineering Software* 35, 843–859.
- Johnson, C. and B. Mercier (1978). Some equilibrium finite element methods for the linear elasticity problem. *Numerische Mathematik* 30, 103–116.
- Kantorovich, L. and V. Krylov (1958). *Approximate methods of higher analysis* (Third ed.). P. Noordhoff LTD.
- Kitipornchai, S. and N. S. Trahair (1975). Elastic behavior of tapered monosymmetric I-beams. *Journal of the structural division* 101, 11479–11515.
- Kosmatka, J. B., H. C. Lin, and S. B. Dong (2001). On Saint-Venant's problem for an inhomogeneous, anisotropic cylinder - part II: cross-sectional properties. *ASME, Journal of Applied Mechanics* 68, 382–391.
- Kushnir, V., J. Quintana, and P. Georgopoulos (1993). On the sagittal focusing of synchrotron radiation with a double crystal monochromator. *Nuclear Instruments and Methods in Physics Research, section A* 328, 588–591.
- Lacarbonara, W. and A. Paolone (2007). On solution strategies to Saint-Venant problem. *Journal of Computational and Applied Mathematics* 206, 473–497.

- Ladeveze, P. and J. Simmonds (1998). New concepts for linear beam theory with arbitrary geometry and loading. *European Journal of Mechanics, A/solids* 17, 377–402.
- Li, G.-Q. and J.-J. Li (2002). A tapered timoshenko-euler beam element for analysis of steel portal frames. *Journal of Constructional Steel Research* 58, 1531–1544.
- Lin, H. C., S. B. Dong, and J. B. Kosmatka (2001). On Saint-Venant’s problem for an inhomogeneous, anisotropic cylinder - part III: end effects. *ASME, Journal of Applied Mechanics* 68, 392–398.
- Lo, K., R. Christensen, and E. Wu (1977a). A high order theory for plate deformations, part i homogeneous plates. *Journal of Applied Mechanics* 44, 663–668.
- Lo, K., R. Christensen, and E. Wu (1977b). A high order theory for plate deformations, part ii: lamianted plates. *Journal of Applied Mechanics* 44, 669–676.
- Pechstein, A. and J. Schoberl (2012). Anisotropic mixed finite elements for elasticity. *Int* 90, 196–217.
- Quarteroni, A., E. Sacco, and F. Saleri (2007). *Numerical Mathematics*, Volume 37. Springer.
- Reddy, J. (1984). A simple higher-order theory of lamianted composite plates. *ASME, Journal of Applied Mechanics of Composite Materials* 51, 745–752.
- Reissner, E. (1986). On a variational theorem and on shear deformable plate theory. *International Journal for Numerical Methods in Engineering* 23, 193–198.
- Rohwer, K., S. Friedrichs, and C. Wehmeyer (2005). Analyzing laminated structures from fibre - reinforced composite material - an assessment. *Technische Mechanik* 25, 59–79.
- Rohwer, K. and R. Rolfes (1998). Calculating 3d stresses in layered composite plates and shells. *Mechanics of Composite Materials* 34, 355–362.
- Saritas, A. and F. C. Filippou (2009). Inelastic axial-flexure-shear coupling in a mixed formulation beam finite element. *International Journal of Non-Linear Mechanics* 44, 913–922.
- Sheinman, I. (2001). On the analytical closed-form solution of high-order kinematic models in laminated beam theory. *International Journal for Numerical Methods in Engineering* 50, 919–936.
- Spacone, E., F. C. Filippou, and F. F. Taucer (1996). Fibre beam-column model for non-linear analysis of r/c frames: part I formulation. *Earthquake engineering and structural dynamics* 25, 711–725.
- Spilker, R. (1982). Hybrid-stress eight-node elements for thin and thick multilayer laminated plates. *International Journal for Numerical Methods in Engineering* 18, 801–828.
- Stein, E. (2012). Milestones of direct variational calculus and its analysis from the 17th century until today and beyond – mathematics meets mechanics– with restiction to linear elasticity. *Computer assisted methods in engineering and science* 19, 7–91.
- Timoshenko, S. (1955). Strength of materials. In *Elementary theory and problems*. Krieger publishing company.
- Timoshenko, S. and J. N. Goodier (1951). *Theory of Elasticity* (Second ed.). McGraw-Hill.

- Vinayak, R., G. Prathap, and B. Naganarayana (1996a). Beam elements based on a higher order theory – I formulation and analysis of performance. *Computers and Structures* 58, 775–789.
- Vinayak, R., G. Prathap, and B. Naganarayana (1996b). Beam elements based on a higher order theory – II boundary layer sensitivity and stress oscillations. *Computers and Structures* 58, 791–796.
- Vinod, K. G., S. Gopalakrishnan, and R. Ganguli (2007). Free vibration and wave propagation analysis of uniform and tapered rotating beams using spectrally formulated finite elements. *International Journal of Solids and Structures* 44, 5875–5893.
- Vogelius, M. and I. Babuska (1981a). On a dimensional reduction method I. the optimal selection of basis functions. *Mathematics of Computation* 37, 31–46.
- Vogelius, M. and I. Babuska (1981b). On a dimensional reduction method II. some approximation-theoretic results. *Mathematics of Computation* 37, 47–68.
- Wanji, C. and W. Zhen (2008). A selective review on recent development of displacement-based laminated plate theories. *Recent Patents on Mechanical Engineering* 1, 29–44.
- Zienkiewicz, O. and R. Taylor (2000a). The finite element method. In *The basis* (V ed.). Butterworth Heinemann.
- Zienkiewicz, O. and R. Taylor (2000b). The finite element method. In *Solid mechanics*. Butterworth Heinemann.

